

Antenna Design with Characteristic Mode Analysis for Internet of Things Applications

by

Qianyun Zhang

A thesis submitted to the University of London for the degree of
Doctor of Philosophy

School of Electronic Engineering and Computer Science
Queen Mary University of London
United Kingdom

June 2018

TO MY FAMILY

Abstract

The TV white space (TVWS) is one of the promising technologies to provide wide coverage, energy efficient and cost effective Internet of Things (IoT) services. However, its low operating frequency and wide bandwidth poses significant challenges to antenna designs.

In this thesis, three antennas are developed using the characteristic mode analysis (CMA) for IoT devices operating over the TVWS.

First, a very-low profile circular small antenna is transformed from a vertical monopole antenna. The CMA is used to determine the mode to be excited and to design a specific feeding structure. After being printed on Rogers 5880 substrate, the final antenna structure operates at 474 MHz with a $VSWR < 2$ bandwidth of 2.2 MHz. Its lateral radius is just 5.2% of the wavelength of its resonant frequency.

Second, a compact U-shaped printed UWB monopole antenna is proposed to operate over the entire UHF TV spectrum. This antenna measures $0.36\lambda_0 \times 0.06\lambda_0 \times 0.01\lambda_0$ where λ_0 is the wavelength of its lowest operating frequency. Its $VSWR < 2$ bandwidth is 87.5%, and the UWB behaviour is discussed by the CMA.

Third, a novel antenna design method is established on annular ring-shaped structures with modal characteristics revealed by the CMA. Following the proposed method, another UWB antenna is achieved by creating and exciting multiple modes with resonant frequencies distributed across the UHF TV spectrum.

All antenna designs are verified thorough simulations and measurements. Furthermore, antennas are also integrated into IoT devices and their system performance is measured under different communication scenarios. The system measurements also verify the good propagation property and the abundant spectrum resource of the TVWS.

Acknowledgments

Foremost, I would like to express my sincere gratitude to my supervisor, Dr. Yue Gao, for his guidance, patience, and continuous support throughout my years of Ph.D. With his profound knowledge and rich research experience, he offered me many valuable ideas, suggestions, and comments on my Ph.D. research and personal long-term development. He has always taught me to keen on pursuing the essence of phenomena and encouraged me to be an independent and hard-working researcher. To be his student is the greatest treasure I have ever had.

I would also like to thank Prof. Chive G. Parini and Dr. Akram Alomainy for their valuable advice and insightful comments. Our discussions at each milestone throughout my Ph.D. study did help to shape my research profile and to cultivate my ability of scientific writing. I would also like to thank Dr. Runbo Ma, Prof. Dirk Manteuffel, and Dr. Yujiang Wu who gave me lots of constructive suggestions on antenna designs and theoretical analyses.

I sincerely thank Dr. Max Munoz Torrico, Ms. Geetha Bommireddy, Dr. Qian Xu, Dr. Massimo Candotti, and Mr. Tony Stone for their kind help and support in the fabrication and measurement of antennas, without which designs proposed in this thesis could not have been experimentally verified.

I am deeply grateful to all my friends in Queen Mary: Dr. Zhijin Qin, Dr. Yuan Ma, Dr. Biyi Wu, Dr. Yuanwei Liu, Dr. Biao Peng, Dr. Qiao Cheng, Dr. Min Zhou, Dr. Yang Zeng, Dr. Ke Yang, Dr. Xiang Li, Dr. Guangwei Jiang, Mingtuan Lin, Xingjian Zhang, Wei Su, Haoran Qi, Shaker Alkaraki, Beici Liang, Haoyang Zhang, Rui Zhang, Liang Yang, Darryl Smith, Dr. Peter Alizadeh, Dr. Oleksandr Sushko, etc. for the research discussions, for the sleepless nights we were working together, and for every

unforgettable moments we shared in London.

Finally, with my love and gratitude, I would like to thank my parents who always encourage and support me with not only tremendous love and patience, but also enthusiastic and energetic attitudes towards their own work. To them I would like to dedicate this thesis.

Table of Contents

Abstract	i
Acknowledgments	ii
Table of Contents	iv
List of Figures	viii
List of Tables	xiv
List of Abbreviations	xv
1 Introduction	1
1.1 Background	1
1.2 Motivations and Contributions	2
1.2.1 Motivations	2
1.2.2 Contributions	3
1.3 List of Publications	4
1.4 Organisation of the Thesis	7
2 Background	9
2.1 Internet of Things Systems	9
2.1.1 Overview of the Internet of Things	9
2.1.2 Connectivity Technologies for the Internet of Things	11

2.1.3	Overview of TV White Space	13
2.2	Antenna Miniaturization	14
2.2.1	Fundamental Limitations for Small Antennas	15
2.2.2	Approaches to Antenna Miniaturization	18
2.3	Ultra-Wideband Technology	21
2.3.1	Overview of the Ultra-Wideband Technology	22
2.3.2	Ultra-Wideband Antennas	24
2.4	Characteristic Mode Theory	27
2.4.1	Physical Interpretations of Characteristic Modes	27
2.4.2	Bandwidth Estimation	29
2.4.3	Excitation of Characteristic Modes	30
2.4.4	State-of-the-art Review of Characteristic Mode Analysis on Antenna Designs	31
2.5	Summary	34
3	Design of a Narrowband Miniaturized Circular Antenna	35
3.1	Introduction	35
3.1.1	Related Work	35
3.1.2	Contributions	36
3.2	Radiating Body Design and Characteristic Mode Analysis	37
3.2.1	Circular Radiating Body with Disk Ground Plane	37
3.2.2	Radiating Bodies with Different Ground Planes	40
3.3	Proposed Radiator on Substrate	43
3.4	Proposed Radiator with a Feeding Loop	45
3.5	Simulation and Measurement Results and Analyses	47
3.6	Summary	51
4	Design of an UWB U-shaped Printed Monopole Antenna	52
4.1	Introduction	52
4.1.1	Related Work	52

4.1.2	Contributions	54
4.2	Antenna Design	55
4.2.1	Radiating Body Design and Characteristic Mode Analysis	55
4.2.2	Characteristic Mode Analysis on the Proposed Antenna	58
4.3	Parametric Study and Measurement	62
4.3.1	Parametric Study	62
4.3.2	Antenna Measurement	64
4.3.3	Bandwidth-Efficiency Product against Antenna Electrical Size	71
4.4	Summary	71
5	Design of an UWB Dual Annular Ring Antenna	73
5.1	Introduction	73
5.1.1	Related Work	74
5.1.2	Contributions	75
5.2	Characteristic Mode Analysis on an Annular Ring and Feeding Structure Design	76
5.2.1	Characteristic Mode Analysis on an Annular Ring	76
5.2.2	Cutting Slots on the Annular Ring	79
5.2.3	Characteristic Mode Analysis with Feeding Structure	82
5.3	Structure Modification and Feeding Refinement	85
5.3.1	Structure Modification	85
5.3.2	Feeding Refinement	88
5.4	Antenna Optimization and Measurement	88
5.4.1	Antenna Optimization	88
5.4.2	Antenna Measurement	92
5.4.3	Discussions on the Unbalanced Coaxial Cable	96
5.5	Summary	99
6	System Measurement	103
6.1	Introduction	103

6.1.1	Related Work	104
6.1.2	Contribution	104
6.2	Sensor Node Enabled by a Miniaturized Narrowband Antenna	105
6.2.1	System Description	105
6.2.2	Measurement Results and Discussions	107
6.3	UHF TV Spectrum Monitoring	110
6.3.1	System Description	110
6.3.2	Measurement Results and Discussions	111
6.4	TVWS Network Provisioning with Directional and Omni-directional Terminal Antennas	112
6.4.1	System Description	112
6.4.2	Measurement Location Selection	115
6.4.3	Measurement Results and Discussions	117
6.5	Summary	121
7	Conclusions and Future Work	122
7.1	Conclusions	122
7.2	Future Work	124
7.2.1	Time Domain Behavior of UWB Antennas	125
7.2.2	Variations of the UWB Annular Ring-Shaped Antenna	125
7.2.3	Radiation Pattern Synthesis and Stability	125
7.2.4	Platform-Embedded Antenna Design	126
	References	127

List of Figures

2.1	IoT Framework.	10
2.2	Frequency allocation of channels 21-69 in the spectrum between 470 MHz and 862 MHz in the United Kingdom.	13
2.3	UHF TV spectrum usage in London (Crystal Palace) [1].	14
2.4	The method for determining the radius, a , of the smallest enclosing sphere. (a) For an antenna without ground plane, it is the smallest sphere to enclose the entire antenna. (b) For antennas on a small ground plane with less than $\lambda/4$ radius, or closer than $\lambda/4$ from an edge, the sphere encloses the entire ground plane. (c) For antennas on an electrically large ground plane, the sphere encloses the antenna and its image currents [2].	16
2.5	The measured bandwidth-efficiency products for 110 antenna designs published in the <i>IEEE Transactions on Antennas and Propagation</i> by the end of the year 2010 [2].	17
2.6	Illustration of the image theory.	19
2.7	The effect of slots and notches on currents on a patch [3].	20
2.8	The iterative-generation procedure for a Vicsek fractal.	21
2.9	Illustrations of (a) helical antenna and (b) Vivaldi antenna [4].	25
2.10	Illustrations of (a) spiral antenna and (b) log-periodic antenna [4].	26
2.11	Illustrations of two UWB antennas with multiple resonances [5, 6].	26
2.12	Illustration of modal decomposition on a metallic plate.	28

3.1	The proposed planar circular radiating body with a disk ground plane. . .	38
3.2	Current flows of (a) mode 1 and (b) mode 2.	39
3.3	Eigen values and modal significances for the first three modes on the structure shown in Fig. 3.1.	39
3.4	Structures with variant grounds and their current flows of mode 1: (a) <i>ring 1</i> , (b) <i>ring 2</i> , and (c) <i>ring 3</i>	40
3.5	Near H-fields in the xz -plane of mode 1 for radiating bodies with different ground planes: (a) disk, (b) <i>ring 1</i> , (c) <i>ring 2</i> , and (d) <i>ring 3</i>	41
3.6	Eigen values of radiating bodies with different ground planes.	42
3.7	Far-field radiation patterns of radiating bodies with different ground planes.	43
3.8	Eigen values χ_1 of radiators with substrates at different thicknesses repre- sented by h in terms of λ_0	44
3.9	(a) Structure layout of the proposed circular antenna with a feeding loop. (b) The current flow of mode 1 for the antenna.	46
3.10	Modal excitation coefficients (2.19) and normalized resonant frequencies of mode 1 with respect to length of the feeding loop l_f	46
3.11	Prototype of the proposed antenna: (a) radiator side view and (b) fee- ding loop side view. ($r_1=33\text{mm}$, $r_2=26\text{mm}$, $r_3=15.5\text{mm}$, $r_4=11.5\text{mm}$, and $h=3.1\text{mm}$ corresponding to parameters in Fig. 3.1).	48
3.12	VSWR and radiation efficiency of the proposed antenna.	48
3.13	Radiation patterns of the proposed antenna.	49
3.14	Eigen value χ_1 of the proposed circular radiator with a test cable at dif- ferent lengths.	50
3.15	Comparison of bandwidth-efficiency product between the proposed antenna and other antennas.	50
4.1	Normalized current distributions of the first three modes for (a) rectan- gular plate and (b) U-shaped plate in simulation.	55

4.2	Simulated characteristic angles of the first three modes for rectangular (solid curves) and U-shaped (dashed curves) plates. Modes 1, 2, and 3 are noted by 'o', '△', and '+', respectively. L is the length of the plate and c is the speed of light.	56
4.3	Geometry of the proposed antenna (a) top view and (b) side view.	57
4.4	Simulated modal current distributions of (a) mode 1 at 370 MHz, (b) mode 2 at 700 MHz, (c) mode 3 at 1080 MHz, (d) mode 4 at 1010 MHz, and (e) mode 5 at 1300 MHz on the proposed antenna (current indicators on the U-shaped radiator are noted by solid lines, while those on the ground are noted by dashed curves).	59
4.5	Simulated characteristic angles of modes 1-5 on the proposed antenna.	60
4.6	Simulated modal VSWRs of modes 1-5 and the total VSWR on the proposed antenna.	61
4.7	Simulated characteristic angles of modes 1-5 after reducing L_{rect} used in Fig. 4.5 by 8 mm.	61
4.8	Simulated VSWRs for different widths of the slit between the radiating body and the ground.	63
4.9	Simulated VSWRs for different dimensions of the notch on the ground.	64
4.10	Prototype of the proposed antenna (a) top view and (b) back view.	65
4.11	Simulated and measured VSWRs of the proposed antenna.	66
4.12	Simulated (solid curves) and measured (dashed curves) E-plane and H-plane radiation patterns at (a) 474MHz, (b) 630MHz, and (c) 786MHz.	67
4.13	Simulated and measured realized gains over the UHF TV spectrum.	68
4.14	Set up of the antenna radiation efficiency measurement using two-antenna method in a reverberation chamber.	69
4.15	Measured radiation efficiency of the proposed antenna over the UHF TV spectrum.	70
4.16	The measured bandwidth-efficiency product for antenna designs summarized in [2] (noted by 'o') and the proposed antenna (noted by '+').	72

5.1	Geometry of an annular ring ($R_1=100$ mm, $R_2=70$ mm, $r_1=68$ mm, and $r_2=45$ mm).	76
5.2	Modal current distributions and radiation patterns of (a) mode 1 at 708 MHz, (b) mode 2 at 794 MHz, and (c) mode 3 at 950 MHz on the annular ring shown in Fig. 5.1.	77
5.3	Characteristic angles of modes 1-3 for annular rings with and without slots.	78
5.4	Current distributions of mode 1 and mode 2 on the original ring and illustrations of different slot cuttings.	80
5.5	Modal current distributions and radiation patterns of (a) mode 1 at 610 MHz, (b) mode 2 at 654 MHz, and (c) mode 3 at 950 MHz on the annular ring with slots.	81
5.6	Structure layout of the slotted annular ring with a rectangular strip (a) top view and (b) side view.	82
5.7	Modal current distributions and radiation patterns of (a) mode 1^a at 553 MHz, (b) mode 1^b at 809 MHz, (c) mode 2 at 654 MHz, and (d) mode 3 at 950 MHz on the structure containing a ring and a rectangular strip. . .	83
5.8	(a) Characteristic angles and (b) modal weight coefficients of modes 1^a , 1^b , 2, and 3 given in Fig. 5.7.	84
5.9	Modal current distributions and radiation patterns of (a) mode 1^c at 552 MHz, (b) mode 4 at 776 MHz, and (c) mode 1^d at 1198 MHz on the structure containing dual rings and a rectangular strip.	86
5.10	(a) Characteristic angles and (b) modal weight coefficients of modes 1^c , 4, and 1^d given in Fig. 5.9.	87
5.11	Structure layout of dual rings with two rectangular strips (a) top view and (b) side view.	88
5.12	(a) Characteristic angles and (b) modal weight coefficients of modes 1^c , 4, and 1^d corresponding to structure shown in Fig. 5.11.	89

5.13	Modal current distributions on the structure containing two rings and four strips (a) mode 1^c at 546 MHz, (b) mode 2^c at 581 MHz, (c) mode 4 at 760 MHz, (d) mode 5 at 981 MHz, (e) mode 1^d at 1102 MHz, and (f) mode 2^d at 1500 MHz.	90
5.14	(a) Characteristic angles and (b) modal weight coefficients of modes 1^c , 2^c , 4, 5, 1^d , and 2^d given in Fig. 5.13.	91
5.15	Structure layout of the final antenna (a) top view and (b) bottom view. . .	92
5.16	Prototype of the proposed antenna (a) top view and (b) bottom view. . .	93
5.17	Simulated and measured (a) reflection coefficients and (b) realized gains of the proposed antenna.	94
5.18	Simulated and measured radiation patterns at (a) 500 MHz, (b) 600 MHz, (c) 700 MHz, and (d) 800 MHz in the xz and yz plane.	95
5.19	(a) Resistances and (b) absolute resistances for antennas fed by a discrete port and a 5 mm coaxial cable.	97
5.20	Reflection coefficients for antennas fed by a discrete port and a 5 mm coaxial cable.	98
5.21	Reflection coefficients for antennas with different cable lengths.	99
5.22	Radiation patterns of the proposed antenna with coaxial cables at different lengths at 500 MHz in (a) yz plane, (b) xy plane, and (c) xz plane. . . .	100
5.23	Radiation patterns of the proposed antenna with coaxial cables at different lengths at 800 MHz in (a) yz plane, (b) xy plane, and (c) xz plane. . . .	101
6.1	Sensor node with (a) a commercial spiral antenna and a serial port extension and (b) the in-house developed antenna.	106
6.2	Measurement setup in an anechoic chamber.	107
6.3	Detected signal intensity over 470-480 MHz.	108
6.4	Normalized peak signal strengths detected by the spectrum monitor when the transmitter turns to different directions.	109

6.5	RFeye node with (a) the in-house developed antenna and (b) a commercial antenna.	110
6.6	The UHF TV spectrum detected by a spectrum monitor equipped with the in-house developed antenna and a commercial antenna.	111
6.7	Channel occupation of the UHF TV spectrum.	112
6.8	Yagi-Uda antenna connected to the base station.	113
6.9	(a) Commercial log-periodic antenna and (b) in-house developed printed monopole antenna connected to the client.	114
6.10	Radiation patterns of the commercial log-periodic antenna [7] and the in-house developed printed monopole antenna in (a) elevation plane and (b) azimuth plane at 630MHz.	115
6.11	Floor plans of EE building (composed of Section I, Section II and Section III), People’s Palace, CS building and ITL building. The ground floor is in white, the first floor is in orange, the second floor is in yellow, and the third floor is in green.	116
6.12	Link SINRs with client antenna turning to different directions. SINRs of uplink signals are noted by ‘o’ and those of downlink are noted by ‘+’. Blue symbols stand for SINRs acquired using the log-periodic antenna at the client and red symbols are for using the printed monopole antenna. . .	119
7.1	Antennas proposed in this thesis and their main features.	123

List of Tables

2-A	Comparison of different connectivity technologies for the IoT.	12
3-A	Normalized resonant frequencies.	44
4-A	Dimensions of the proposed antenna.	62
4-B	Bandwidths and sizes of antennas covering the UHF TV spectrum (λ_L is the wavelength of the lowest operating frequency).	66
5-A	The polynomial coefficients of (5.1) calculating the resonant frequency (in MHz) of mode 1.	79
5-B	The polynomial coefficients of (5.1) calculating the resonant frequency (in MHz) of mode 2.	79
5-C	Resonant frequencies of mode 1 and mode 2 on rings with different slot cuttings.	81
5-D	Dimensions of the proposed antenna.	93
6-A	Received RSSIs with the transmitter turning to different directions.	109
6-B	Comparison between antennas connected to the TVWS client: the in-house developed printed monopole antenna and the commercial log-periodic antenna.	113
6-C	Variances of SINRs acquired when client antennas facing at different directions.	118
6-D	Realized downlink and uplink speeds.	121

List of Abbreviations

ATM	Automated Teller Machine
BMW	Bavarian Motor Vehicle
CCE	Capacitive Coupling Element
CMA	Characteristic Mode Analysis
CS	Computer Science
CR	Cognitive Radio
DTV	Digital Television
DVB—T	Digital Video Broadcasting—Terrestrial
EIRP	Equivalent Isotropically Radiated Power
EE	Electronic Engineering
FCC	Federal Communications Commission
GPS	Global Positioning System
HetNets	Heterogeneous Networks
IBM	International Business Machines Corporation
ICE	Inductive Coupling Element
LoS	Light-of-Sight
IoT	Internet of Things
ITL	Informatics Teaching Laboratory
LTE	Long-Term Evolution

NLoS	Non-Light-of-Sight
LPWAN	Low-Power Wide-Area Network
Ofcom	Office of Communications
PIFA	Planar Inverted-F Antenna
PMSE	Programme Making and Special Event
QMUL	Queen Mary University of London
QoS	Quality of Service
RFID	Radio-Frequency Identification
RSSI	Received Signal Strength Indicators
SIG	Special Interest Group
SINR	Signal-to-Interference-Plus-Noise Ratio
SNR	Signal-to-Noise Ratio
TCM	Theory of Characteristic Mode
TD	Time Division
TVWS	TV White Space
TVWSD	TV White Space Device
UHF	Ultra-High Frequency
UWB	Ultra-Wideband
VHF	Very High Frequency
VSWR	Voltage Standing Wave Ratio
WPAN	Wireless Personal Area Network
WSN	Wireless Sensor Network
WWAN	Wireless Wide Area Network

Chapter 1

Introduction

1.1 Background

“The Internet of Things (IoT) has the potential to change the world, just as the Internet did. Maybe even more so,” said Kevin Ashton, the person firstly coined the term of IoT, and after decades of development, the IoT era is coming [8]. The IoT connects power grids, railways, pipelines, buildings, household appliances, and various objects, all called things, and with technical support from the global positioning system (GPS), wireless sensor networks (WSN), radio-frequency identification (RFID), wireless communications, etc. a huge network reaching everything all over the world is established. According to the BI Intelligence [9], the number of connected IoT devices is expected to exponentially grow, and it will increase to 34 billion by 2020. Keys to unleash benefits of the IoT are the connectivity between things and people as well as communications among things without human intervention.

Based on the quality of service (QoS) requirements of different applications, kinds of wireless connectivity technologies are selectively used for IoT connections, and among which, low-power wide-area networks (LPWANs) are regarded as promising technologies. LoRa and Narrowband-IoT are the representatives of LPWANs, and they operate mainly

at frequencies below 1 GHz. Having longer wavelengths, the sub-1 GHz signals can penetrate and bypass obstacles easily, and therefore reach further areas. Operating on vacant channels reserved for the licensed broadcasting services, the TV white space (TVWS) has been moved forward initially by regulatory steps and deployments of TV white space devices (TVWSDs) by the Federal Communications Commission (FCC) in the United States [10], [11], and Europe is also proceeding with the finalization of rules and testing of TVWS technology on a large scale [12–14]. Since 2013, the use of TVWS spectrum for IoT received a significant boost with the ratification of the version 1.0 core specification of Weightless standard [15]. Therefore, the high market demand and wide application prospect result in new expectations for the conventional ultra-high frequency (UHF) antennas to be used for the IoT applications.

1.2 Motivations and Contributions

1.2.1 Motivations

Modern devices are tending to be increasingly small and miniaturized antennas are expected to be integrated with them. Nevertheless, antenna size is comparable to its operating frequency, and for example, the length of a half-wave dipole antenna working at 500 MHz is around 30 cm. Therefore, it is important but challenging to design compact antennas for devices operating at sub-1 GHz. Moreover, IoT devices operating over TVWS should not cause harmful interference to primary services in the UHF TV spectrum like broadcasting and wireless microphones, and vacant channels available for TVWS operation are changing with location and time. In the United Kingdom, spectrum reserved for the licensed broadcasting services is from 470 MHz to 790 MHz over the UHF band, which has a fractional bandwidth exceeding 50%. According to FCC, a radio system is ultra-wideband (UWB) if its fractional bandwidth is greater than 20% or its absolute bandwidth is wider than 500 MHz [16]. As a result, antennas for smart TVWSDs should be either reconfigurable or have ultra-wide bandwidths, and

thus TVWSDs as cognitive radio devices are able to operate at vacant channels acquired from spectrum detection using methods like geo-location database access and spectrum sensing [17–20]. Proposed by Garbacz [21] and further developed by Harrington and Mautz [22], [23], the theory of characteristic mode (TCM) gives insight into antenna operation by identifying independent modes able to be supported on a structure and the radiation ability of each mode. Therefore, the characteristic mode analysis (CMA) has become one of the popular methodologies for antenna design in recent years. With physical essences revealed by the CMA, radiating structures could be utilized and optimized efficiently. They also help to understand how the UWB property of an antenna is realized. Furthermore, results drawn from the CMA give instructions on feeding structure design in order to excite one or multiple desired characteristic modes.

1.2.2 Contributions

Based on the motivations presented above, contributions of the thesis are summarized as follows:

- CMA is carried out to discuss the radiation behavior of a circular radiating body with ground in the same plane. The relationship between resonant frequency and dimensions of the planar structure is quantified. The shape of the ground plane is then modified to acquire a more efficient structure with a lower resonant frequency. Moreover, scale factors of resonant frequencies for antennas with substrate having different heights are summarized. After incorporating a feeding loop, a complete miniaturized antenna design guideline is given. A very-low profile UHF small antenna is finally fabricated as an example.
- To support smart operation of IoT devices over TVWS, a printed monopole antenna is designed and optimized to work over the entire UHF TV spectrum. CMA demonstrates modal wideband properties of the proposed radiator, and it also reveals that multiple significant modes have been excited to realize the UWB performance.

- Another UWB antenna is proposed and the CMA is applied to help modify the radiating body and design an appropriate feeding structure to excite all desired modes. Its UWB performance is finally achieved through combining resonances of multiple modes. Moreover, to provide a general design reference for annular ring-shaped antennas, a fitted polynomial is given to clarify the relationship between dimensions of an annular ring and resonant frequencies of its basic modes.
- Characteristics of all the proposed antennas are validated via simulations, measurements, and their combination. In addition, by integrating the proposed antennas onto multiple testbeds, their real-time system performance is appraised. Practical communication tests also verify the transmission advantages of TVWS signals.

1.3 List of Publications

Journal Papers

1. **Q. Zhang**, R. Ma, W. Su, and Y. Gao, "Design of a Multi-Mode UWB Antenna Using Characteristic Mode Analysis," *IEEE Transactions on Antennas and Propagation* (Accepted).
2. **Q. Zhang**, and Y. Gao, "A Compact Broadband Dual-Polarized Antenna Array for Base Stations," *IEEE Antennas and Wireless Propagation Letters* (Accepted).
3. **Q. Zhang** and Y. Gao, "Compact Low Profile UHF UWB Antenna with Characteristic Mode Analysis for TV White Space Devices," *IET Microwaves, Antennas & Propagation*, vol. 11, no. 11, pp. 1629-1635, Sep. 2017.
4. **Q. Zhang** and Y. Gao, "Comprehensive Evaluation of an Antenna for TV White Space Devices," *IET Journal of Engineering*, Feb. 2017.
5. L. Bedogni, A. Trotta; M. Di Felice, Y. Gao, X. Zhang, **Q. Zhang**, F. Malabocchia, L. Bononi, "Dynamic Adaptive Video Streaming on Heterogeneous TVWS and

- Wi-Fi networks,” *IEEE/ACM Transactions on Networking*, vol. 25, no. 6, pp. 3253-3266, Dec. 2017.
6. Y. Gao, R. Ma, **Q. Zhang** and C. Parini, “Design of Very Low Profile Circular UHF Small Antenna Using Characteristic Mode Analysis,” *IET Microwaves, Antennas & Propagation*, vol. 11, no. 8, pp. 1113-1120, Jun. 2017.
 7. D. Tirapu, **Q. Zhang**, Y. Gao, D. Valderas, “UHF Passive RFID-based sensorless system to detect humidity for irrigation monitoring,” *Microwave and Optical Technology Letters*, vol. 59, no. 7, pp. 1709-1715, May 2017.
 8. Y. Gao, R. Ma, Y. Wang, **Q. Zhang**, and C. Parini, “Stacked Patch Antenna with Dual Polarization and Low Mutual Coupling for Massive MIMO,” *IEEE Transactions on Antennas and Propagation*, vol. 64, no. 10, pp. 4544-4549, Oct. 2016.
 9. B. Peng, S. Li, J. Zhu, **Q. Zhang**, L. Deng, Li, Q. Zeng and Y. Gao, “Wideband Bandpass Filter with High Selectivity Based on Dual-Mode DGS Resonator,” *Microwave and Optical Technology Letters*, vol. 58, no. 10, pp. 2300-2303, Oct. 2016.
 10. B. Peng, S. Li, J. Zhu, **Q. Zhang**, L. Deng, Q. Zeng and Y. Gao, “Compact Quad-Mode Bandpass Filter Based on Quad-Mode DGS Resonator,” *IEEE Microwave and Wireless Components Letters*, vol. 26, no. 4, pp. 234-236, Apr. 2016.
 11. **Q. Zhang**, B. Wu, and Y. Gao, “MLFMA-Enhanced Half-Space Characteristic Mode Analysis for Vehicle Platforms,” *IEEE Transactions on Vehicular Technology* (Under review).
 12. W. Su, **Q. Zhang**, S. Alkaraki, Y. Zhang, X. Zhang, and Y. Gao, “Radiation Energy and Mutual Coupling Evaluation for Multimode MIMO Antenna Based on the Theory of Characteristic Mode,” *IEEE Transactions on Antennas and Propagation* (Under revision).

Conference Papers

1. **Q. Zhang**, and Y. Gao, “Embedded Antenna Design on LoRa Radio for IoT Applications,” *12th European Conference on Antennas and Propagation*, London, UK, Apr. 2018.
2. **Q. Zhang** and Y. Gao, “Sensor Node Enabled by a Miniaturized Planar Antenna for IoT Applications at TV White Space,” *2017 International Symposium on Advances in Communications and Computing for Internet-of-things (CCIOT-2017)*, Exeter, UK, Jun. 2017.
3. **Q. Zhang** and Y. Gao, “Design of an UHF UWB Doubled Annular Ring Antenna Using Characteristic Mode Analysis,” *11th European Conference on Antennas and Propagation*, Paris, France, Mar. 2017.
4. **Q. Zhang** X. Zhang, Y. Gao, O. Holland, M. Dohler, J. M. Chareau, and P. Chawdhry, “TV White Space Network Provisioning with Directional and Omnidirectional Terminal Antennas,” *2016 IEEE 84th Vehicular Technology Conference, VTC2016-Fall*, Montreal, Canada, Sep. 2016.
5. **Q. Zhang** Y. Gao, and C. Parini, “Compact U-shape Ultra-wideband Antenna with Characteristic Mode Analysis for TV White Space Communications,” *2016 IEEE International Symposium on Antennas and Propagation*, Fajardo, Puerto Rico, Jul. 2016.
6. B. Peng, S. Li, **Q. Zhang**, Y. Gao, J. Zhu, L. Deng, and Q. Zeng, “CPW-Fed Dual-/Tri-Band Slot Antenna Based on Multi-Mode Slot Line Resonator,” *2016 IEEE International Symposium on Antennas and Propagation*, Fajardo, Puerto Rico, Jul. 2016.
7. B. Peng, W. Hong, **Q. Zhang**, Y. Gao, J. Zhu, L. Deng, S. Li and Q. Zeng, “CPW-Fed Dual-Band MIMO Antenna Based on Harmonic Resonance with High Isolation,” *2016 IEEE International Symposium on Antennas and Propagation*,

- Fajardo, Puerto Rico, Jul. 2016.
8. Y. Gao, R. Ma, **Q. Zhang**, and C. Parini, “UHF Antennas for Machine-to-Machine Communications and Internet of Things,” *10th European Conference on Antennas and Propagation*, Davos, Switzerland, Apr. 2016.
 9. **Q. Zhang**, Y. Gao, and C. Parini, “Miniaturized UHF Antenna Using a Magneto-Dielectric Superstrate for M2M Communications,” *2015 IEEE International Symposium on Antennas and Propagation*, Vancouver, Canada, Jul. 2015.
 10. **Q. Zhang**, Z. Chen, Y. Gao, C. Parini, and Z. Ying, “Miniaturized Antenna Array with Co₂Z Hexaferrite Substrate for Massive MIMO,” *2014 IEEE International Symposium on Antennas and Propagation*, Memphis, USA, Jul. 2014.

1.4 Organisation of the Thesis

Chapter 2 provides a comprehensive overview of the theoretical background knowledge and state-of-the-art technologies on IoT systems, antenna miniaturization, UWB technologies, and TCM.

Chapter 3 proposes a miniaturized circular UHF antenna. Its radiating body is gradually improved by analyzing fundamental modes of the structure with different ground planes via CMA, and a feeding loop is designed for excitation.

Chapter 4 designs a compact and low-profile UHF UWB printed monopole antenna. The UWB operation principle of the proposed antenna is revealed from the point of CMA.

Chapter 5 creates multiple modes with resonant frequencies distributed over the spectrum of interest by manipulating annular rings. A feeding structure is designed correspondingly to excite all the significant modes to realize an UWB antenna.

Chapter 6 integrates predesigned antennas into IoT devices and evaluates their

system performance through a series of measurements. The whole UHF TV spectrum at Queen Mary University of London (QMUL) is also detected.

Chapter 7 draws the conclusions and a plan for future work.

Chapter 2

Background

In this chapter, Section 2.1 gives an overview of the IoT system. Different connectivity technologies for the system are summarized and compared, and among which, the TVWS is presented in detail. Section 2.2 explains fundamental limitations for small antennas and introduces some approaches to antenna miniaturization. The UWB technology and representative UWB antenna types are provided in Section 2.3. Section 2.4 interprets the TCM, and introduces important parameters to evaluate characteristic modes. State-of-the-art applications of CMA on antenna designs are also reviewed in this section. Section 2.5 concludes this chapter.

2.1 Internet of Things Systems

2.1.1 Overview of the Internet of Things

Having a huge market potential, the IoT has attracted significant interest from academics, industry and government. Through the IoT, things can communicate without human intervention, and a frame of the IoT system is illustrated in Fig. 2.1. According to the system framework, data of things are collected by sensors, RFID tags, intelligent



Figure 2.1: IoT Framework.

terminals, etc. based on their location, velocity, temperature, power, motion, illumination, air quality, humidity, and any kind of property. Then the data is disseminated to other things or for cloud processing, and the feedback will finally reach the desired things to stimulate corresponding reactions.

New data from Juniper Research has found that retailers will connect 12.5 billion business assets, such as products, digital signs and Bluetooth beacons, to the IoT platforms by 2021 [24]. Benefits of introducing IoT technology into the retail can be seen from Zara, the worlds largest apparel retailer. Data of its products is stored in RFID chips and sent via radio signals to a scanner. As each item is sold, data from its RFID chip prompts an instant order to the stockroom requesting a replacement, making Zara’s supply chain more responsive to store stock levels and avoiding stock deficiencies [25].

The IoT technology has also been exploited in agriculture, and it significantly benefits food production and food safety. Besides, sensors and smart software decision also help to decrease environmental footprint and foster the sustainability. Mounted on cows tails and gathering over 600 pieces of data a second, the Moocall calving sensors will send an alert to farmers smart phones via the Vodafone managed IoT connectivity platform when

a cow is giving birth [26]. CropX, a Silicon Valley company, has developed an adaptive irrigation platform, and through which farmers can improve yield while reducing water usage [27].

At the beginning of the 21st century, self-driving and connected vehicles were solely presented in science fiction films. Now, driving by the IoT, these fantasies are coming true. Since 2016, the Bavarian motor vehicle (BMW) has collaborated with the International Business Machines Corporation (IBM) to improve the personalized and intuitive driving experience, leveraging the IoT. For example, in the future, we will be informed about the nearby available parking, or in how long parking will be available at a specific location. Also, once our cars are approaching home, the system connected with the house will open the garage and light up lamps outside our house [28].

There is no doubt that the IoT has meld into our daily life and its applications on smart farming, smart retail, industrial internet, smart supply chain, smart home, smart city, smart grid, connected health, etc. are all flourishing and changing our lifestyles.

2.1.2 Connectivity Technologies for the Internet of Things

According to QoS requirements of different applications, IoT systems have various data rates and communication ranges. High-data-rate IoT systems achieve large data throughput and low latency, and it ensures the communication quality of high value services like automotive and live radio [29]. On the contrary, low-data-rate systems need a narrower bandwidth, which makes the system receiver sensitive. The thermal noise is proportional to the bandwidth and therefore lower transmit power is required for low data rate systems. Hence this kind of system yields a high link budget, and is ideal for remote management of fixed assets including tracking, telemetry, smart meter, automated teller machine (ATM) and point-of-sales systems [30].

Depending on various application requirements, various kinds of wireless communication technologies, with different characteristics, are selectively adopted to achieve IoT

Table 2-A: Comparison of different connectivity technologies for the IoT.

Technology	Operating frequency	Peak rate	Maximum range
LoRa	433/868/915 MHz ISM bands	50 kbps	15 km
NB-IoT	In-band, stand-alone and guard-band in GSM UMTS and LTE bands	150 kbps	15 km
Sigfox	868/915 MHz ISM bands	100 bps	50 km
NFC	13.65 MHz	424 kbps	10 cm
WiFi	2.4/5 GHz	600 Mbps	Around 50 m
Bluetooth 4.0	2.4 GHz ISM band	Basic: 1 Mbps Enhanced: 3 Mbps	Around 60 m
Zigbee	868/915 MHz and 2.4 GHz ISM bands	20 kbps @ 868 MHz 40 kbps @ 915 MHz 250 kbps @ 2.4 GHz	100 m
Weightless-W	470-790 MHz	10 Mbps	10 km

connectivity. Popular technologies are summarized in Table 2-A, in which their operating frequencies, peak rates and communication ranges are all specified. For example, WiFi and Bluetooth have very low power consumptions and high data rates, but their coverages are limited. To make the world smart, the IoT needs wide area connectivity–network across cities, not across the office [31]. Cellular networks, although operating over several kilometres, are not extensively applied in the IoT due to their high power consumption and high modem cost. Ultimately, LPWANs are regarded promising to be used for the IoT connectives. LoRa, NB-IoT and Sigfox are the representatives of LPWANs, and they are mainly operated at frequencies below 1 GHz. Having longer wavelength, the sub-1 GHz signals can penetrate and bypass obstacles more easily, and therefore cover wider areas. As a result, fewer base stations or access points are needed, and lower energy will be consumed at nodes and networks, which leads to long battery life and low deployment cost.

However, with the tremendous increase of heterogeneous objects connected in the IoT, unlicensed ISM bands are becoming congested, and new spectrums are expected to support IoT communications. Dynamic frequency allocation will also have to be adopted for efficiency spectrum utilization [32], and fortunately the use of opportunistic

21	22	23	24	25	26	27	28	29	30
470-478	478-486	486-494	494-502	502-510	510-518	518-526	526-534	534-542	542-550
31	32	33	34	35	36	37	38	39	40
550-558	558-566	566-574	574-582	582-590	590-598	598-606	606-614	614-622	622-630
41	42	43	44	45	46	47	48	49	50
630-638	638-646	646-654	654-662	662-670	670-678	678-686	686-694	694-702	702-710
51	52	53	54	55	56	57	58	59	60
710-718	718-726	726-734	734-742	742-750	750-758	758-766	766-774	774-782	782-790
61	62	63	64	65	66	67	68	69	
790-798	798-806	806-814	814-822	822-830	830-838	838-846	846-854	854-862	

TV White
Space

Cleared
Spectrum

PMSE

Figure 2.2: Frequency allocation of channels 21-69 in the spectrum between 470 MHz and 862 MHz in the United Kingdom.

radio resource utilization based on cognitive radio (CR) can provide efficiency as well as reliability [33, 34]. Operating on vacant channels reserved for the licensed broadcasting services, the TVWS offers abundant spectrum resources for cost effective IoT communications.

2.1.3 Overview of TV White Space

Lately, the world has gone through digital switchover, which releases spectrum within 174-230 MHz and 470-862 MHz by transiting terrestrial television broadcasting from analogue to digital [35]. Frequency allocation for channels in the spectrum between 470 MHz and 862 MHz in the United Kingdom is shown in Fig. 2.2. Digital terrestrial television services occupy the frequency band over 470-790 MHz, which is divided into 40 channels from channel 21 to channel 60, and each channel has a bandwidth of 8 MHz. It worth mentioning that over the UHF TV spectrum, the 38th channel is reserved for programme making and special events (PMSEs).

Within an area, the DTT services will not occupy all UHF TV channels at one time,

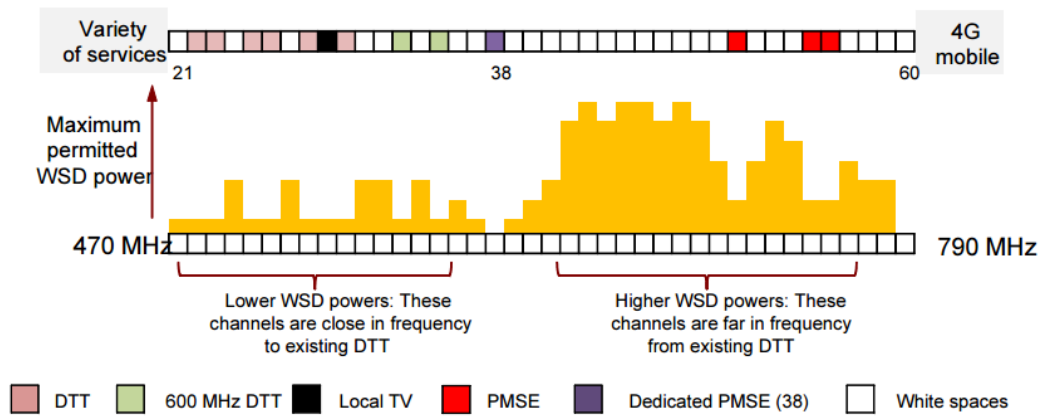


Figure 2.3: UHF TV spectrum usage in London (Crystal Palace) [1].

and the unused spectrum is known as TVWS. An example of spectrum usage over the UHF TV spectrum usage in London is shown in Fig. 2.3. It can be observed that a large portion of the UHF TV spectrum can be used for unlicensed power transmissions. In 2008, the FCC approved unlicensed use of TVWS [10] in the United States. Subsequently, the Office of Communications (Ofcom) has also enabled license-exempt use of TVWS in the United Kingdom [13]. The use of TVWS for IoT applications received a significant boost in April 2013 with the ratification of the version 1.0 core specification by Weightless Special Interest Group (SIG) [15].

In spite of taking the world by storm, the IoT still faces challenges including security, privacy, connectivity, compatibility, etc. This thesis focuses the attention on design of miniaturized and UWB antennas for IoT devices and evaluation of their performance under different scenarios.

2.2 Antenna Miniaturization

Nowadays devices are tending to be increasingly compact, and therefore antennas equipped with them are required to be as small and low profile as possible while keeping good performance. It is a significant challenge for antennas designed for IoT devices because size of antennas are physically restricted by their operating frequencies. In addition, to

realize low power consumption and long battery life, antennas are expected to possess high efficiency and reasonable gain. In the following, fundamental limitations for small antennas and some general approaches to antenna miniaturization are presented.

2.2.1 Fundamental Limitations for Small Antennas

It has been commonly known that antenna efficiency and bandwidth are always sacrificed to realize antenna miniaturization. Therefore, it is important to understand the relationship between antenna efficiency, bandwidth, and its size. In 2005, Yaghjian and Best [36] derived that the quality factor (Q) is inversely proportional to the antenna bandwidth

$$B \approx \frac{1}{Q} \left(\frac{s-1}{\sqrt{s}} \right) \quad (2.1)$$

where B is the bandwidth and s is the specified value of the voltage standing wave ratio (VWSR) at the edge of the band. The quality factor is defined as the ratio of the stored energy (W_{stored}) over the energy dissipated in one cycle ($P_{dissipated}$) [37–40]

$$Q = \frac{2\omega W_{stored}}{P_{dissipated}} \quad (2.2)$$

where ω is the angular frequency and $\omega = 2\pi f$, and f indicates the frequency.

Wheeler [41] firstly proposed fundamental limitations of small antennas in 1947. He defined the radiation power factor for electric antennas (p_e) and magnetic antennas (p_m) as

$$p_e = \frac{G}{\omega C} \quad (2.3a)$$

$$p_m = \frac{R}{\omega L} \quad (2.3b)$$

where C or L is the capacitance or inductance, and G or R is the radiation shunt conductance or series resistance. He demonstrated that the radiation power factor of either kind of antenna is greater than $\frac{1}{6\pi} k^3 V_c$, in which V_c is the cylindrical volume

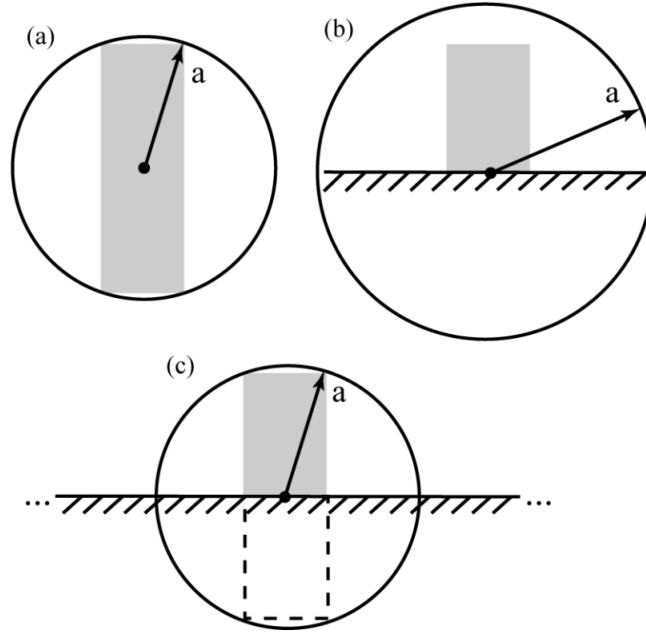


Figure 2.4: The method for determining the radius, a , of the smallest enclosing sphere. (a) For an antenna without ground plane, it is the smallest sphere to enclose the entire antenna. (b) For antennas on a small ground plane with less than $\lambda/4$ radius, or closer than $\lambda/4$ from an edge, the sphere encloses the entire ground plane. (c) For antennas on an electrically large ground plane, the sphere encloses the antenna and its image currents [2].

occupied by the antenna, k is the wave number associated with the electromagnetic field and equals to $2\pi/\lambda$, and λ represents the wavelength.

In the following year, Chu [37] provided a plot of the minimum quality factor of omnidirectional antennas. Later, following Chu's analyses, Hansen [38] and McLean [39] derived an expression for the quality factor of the lowest order mode in terms of the antenna's electrical size

$$Q = \frac{1 + 2(ka)^2}{(ka)^3[1 + (ka)^2]} \cdot \eta \quad (2.4)$$

where η is the radiation efficiency, a is the minimum radius of a sphere enclosing the antenna, and the determination of a for different types of antennas is shown in Fig. 2.4 [2].

Through subtracting the energy density associated with the power flow from the total

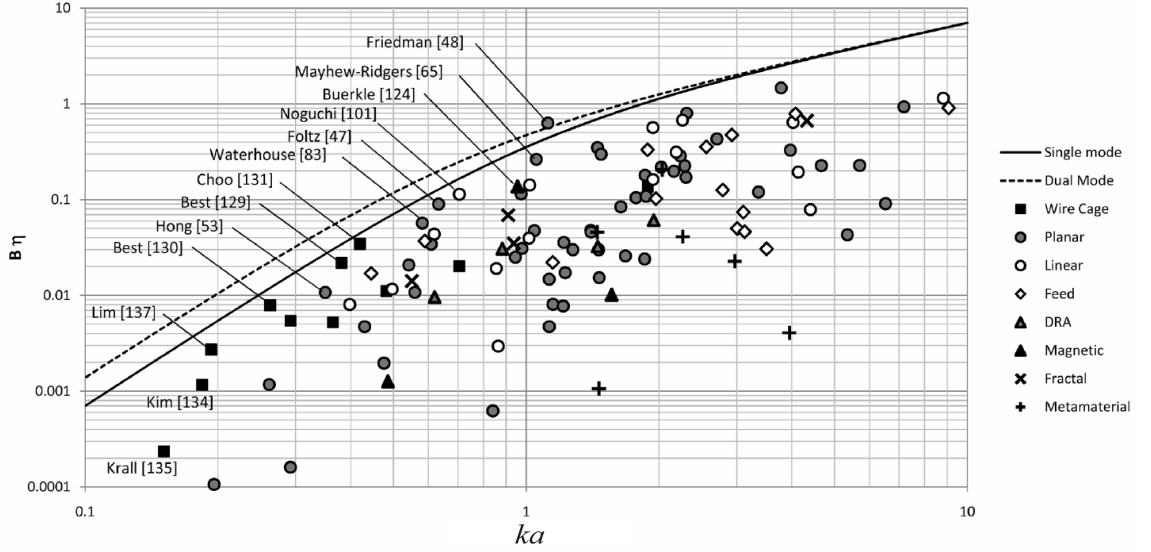


Figure 2.5: The measured bandwidth-efficiency products for 110 antenna designs published in the *IEEE Transactions on Antennas and Propagation* by the end of the year 2010 [2].

energy density, Collin and Rothschild [40] enabled the magnetic and electric reactive energy to be computed, and they simplified the quality factor of the first mode as

$$Q = \frac{1}{(ka)^3} + \frac{1}{ka} \quad (2.5)$$

Discussions introduced above were all for linear polarized antennas, and by combining TE_{01} and TM_{01} fields, McLean [39] obtained the quality factor for circular polarized antennas as

$$Q = \frac{1}{ka} + \frac{1}{2(ka)^3} \quad (2.6)$$

Recently, Sievenpiper *et al.* summarized the products of bandwidths and efficiencies for 110 antenna designs published in the *IEEE Transactions on Antennas and Propagation* since 2010 [2]. The experimental performance data was plotted together with curves of the theoretical limits as shown in Fig. 2.5. Discussions and analyses based on these statistic results validate the theoretical limits and they also reveal the applicability of the limits for antennas that are not electrically small.

2.2.2 Approaches to Antenna Miniaturization

In recent decades, researchers have devoted much effort to making antennas more compact, and state-of-the-art techniques of antenna miniaturization are summarized as follows.

- Lumped element loading

An antenna can be equivalent to a resonant circuit whose resonant frequency is calculated from

$$f = \frac{1}{2\pi\sqrt{LC}} \quad (2.7)$$

Therefore, loading inductors/capacitors significantly lowers resonant frequencies, and in other words, reduces size of antennas resonating at specific frequencies. Chi *et al.* [42] loaded 14 shunt capacitors along the resonant path of a slot-loop antenna, and their design realized a size reduction of about six times. In addition, the input impedance of an electrically small antenna has a large reactive component, which will make most of the dissipated energy be stored as electrical/magnetic energy. A straightforward method to make a small antenna resonate is to compensate its stored energy by loading inductors/capacitors. However, inductors will introduce severe loss and deteriorate antenna efficiency. Capacitors, on the other hand, have a high quality factor, and lead to the reduction of antenna bandwidth [43].

- Material loading

Electromagnetic waves propagate slower in materials than in free space, and the velocity of propagation (u) is

$$u = \frac{c_0}{\sqrt{\mu_r \varepsilon_r}} \quad (2.8)$$

where c_0 is the speed of light in vacuum, μ_r and ε_r is material's relative permittivity and permeability respectively. Therefore, for a fixed physical length and frequency, longer electrical length is achieved with loading materials.

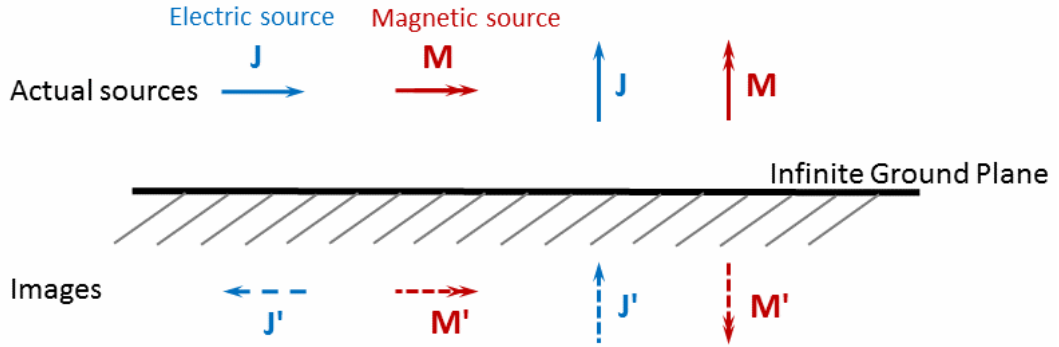


Figure 2.6: Illustration of the image theory.

In [44–46], high-permittivity dielectrics are used to achieve antenna miniaturization. However, this loading leads to the concentration of the electric field in the high permittivity regions, which increases the quality factor and decreases antenna bandwidth. Moreover, a higher permittivity is unfortunately often associated with higher dielectric losses [47].

The wave impedance in a material (η_r) is calculated from

$$\eta_r = \eta_0 \sqrt{\frac{\mu_r}{\epsilon_r}} \quad (2.9)$$

in which η_0 is the wave impedance in free space. Close values of μ_r and ϵ_r will improve the matching of wave impedances in materials and in free space, and make more energy being radiated, which lowers the quality factor. From (2.8), in addition to achieving a wider bandwidth, increasing μ_r also reduces the sizes of antennas by multiple times. Materials with $\mu_r > 1$ are known as magneto-dielectric materials. Many research work has proved, through theoretical analyses or experimental data, that the use of magnetodielectric materials helps to achieve better size-bandwidth characteristics [48–50]. However, currently available magneto-dielectric materials like MFseries (developed by Emerson & Cuming), TTZ series, and Z-type (developed by Trans-Tech) all have large losses over the UHF band, which will lead to low radiation efficiency and gain.

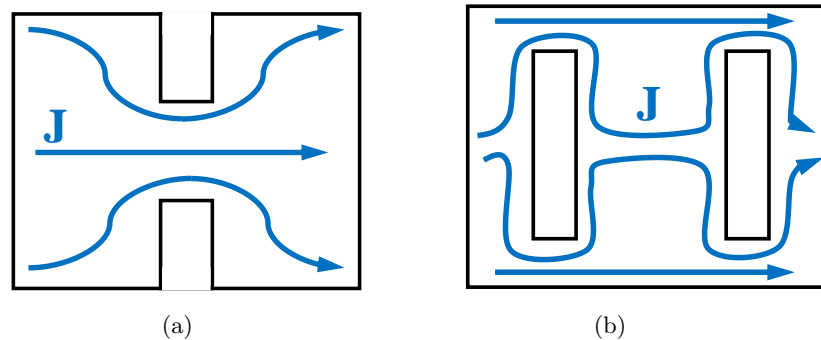


Figure 2.7: The effect of slots and notches on currents on a patch [3].

- Utilizing ground planes and short circuits.

A well known example of reducing antenna size by utilizing ground planes is the transformation from dipole antenna to monopole antenna. Based on the image theory as explained in Fig. 2.6, the length of a monopole antenna mounted above an infinite ground plane is one half of a dipole antenna. The planar inverted-F antenna (PIFA) is a quarter-wavelength patch antenna. Because its patch is shorted at one end, the current at this end of the patch is no longer forced to be zero, and as a result, the PIFA has the same current-voltage distribution as a half-wave patch antenna. Ground planes and short circuits have been used alone or in combination with other techniques widely to achieve antenna miniaturization [51–53].

- Modifying and optimizing antenna geometry

When modifying geometries of antennas, the effective electrical lengths can be increased to achieve more compact antennas. Folding wires repeatedly is a useful method to shorten physical lengths of conventional antennas, and these antennas were classified as meander line antennas by Rashed and Tai [54] in 1991. Chew and Saunders [55] bent the liner element of a conventional printed quadrifilar helix antenna into a rectangular meander, and through which, they reduced the axial length of the conventional antenna by 53%. Moreover, for patch antennas, as shown in Fig. 2.7, slots and notches are often cut to increase electrical lengths.

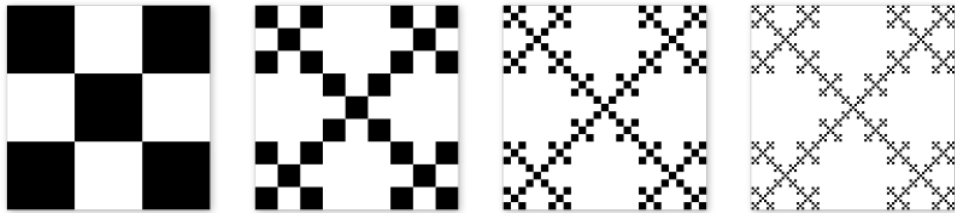


Figure 2.8: The iterative-generation procedure for a Vicsek fractal.

The fractal antenna is another choice for antenna miniaturization. As illustrated in Fig. 2.8, fractals are space-filling geometries that can be used as antennas to effectively fit long electrical lengths into small areas [56].

- Utilizing the environment

After being integrated into devices, properties of small antennas may change and lead to poor radiation. Ban *et al.* [57] divided the metal rim of a smart phone into two strips via a small grounded patch, and the proposed dual-loop antenna was capable to provide hepta-band wireless wide area network and long-term evolution (WWAN/LTE) operation. Operating at very high frequency (VHF), vehicular FM antennas are relatively long, and traditional roof-mounted monopole antennas suffer from lack of durability and undesirable appearance. Therefore, FM antennas printed directly on the rear or quarter glasses of a vehicle has been widely developed [58, 59]. Additionally, rapid development of CMA in recent years enables analyses of electromagnetic characteristics of integration platforms and inspires researchers to make full use of the environment antennas are designed for, which will be introduced in detail in Section 2.4.4.

2.3 Ultra-Wideband Technology

In real communication scenarios, IoT devices communicating over TVWS should operate on one or multiple vacant channels over the UHF TV spectrum based on interactions with geo-location databases, and hence their antennas should be either UWB to cover

the whole UHF TV spectrum or narrowband but reconfigurable to switch over channels. Reconfigurable antennas rely heavily on switching circuits, and the design and integration of these circuits increase the system complexity. Besides, energy will be consumed on switching circuits. More importantly, reconfigurable antennas switch over the fixed bandwidth, and this mechanism prevents TVWSDs to use multiple separated or a bunch of channels at one time, and hence the communication efficiency is restricted. Therefore, this thesis focuses on designs of UWB antennas, and overviews of UWB technology and antennas are given below.

2.3.1 Overview of the Ultra-Wideband Technology

The first UWB signals were generated in experiments by Hertz [60] in 1887, in which he generated sparks and radiated them via wide-band loaded dipoles. Afterwards, the concept of UWB was developed in the early 1960s through research in time domain electromagnetics, where impulse measurement techniques were adopted to characterise the transient behaviour of certain microwave networks [61]. The UWB radio communication received more interest in the 1990s with the improvements in digital signal processing and the invention and investigation of time-hopping impulse radio [62, 63]. In 2002, the FCC [16] defined a radio system to be an UWB system if its bandwidth is wider than 500 MHz or the fractional bandwidth ($FBW = B/f_c$) is greater than 20%.

The Shannon capacity formula gives the upper bound of the capacity (C) of a channel in bits/sec as

$$C = B \log_2(1 + SNR) \quad (2.10)$$

from which C grows logarithmically with the signal-to-noise ratio (SNR) and it grows linearly with bandwidth. Offering extremely large bandwidths, UWB systems exhibit great potential for high data rate communications. Moreover, UWB systems have good multipath immunity. The multipath effect is the out-of-phase addition of light-of-sight (LoS) and/or non-light-of-sight (NLoS) waveforms and it degrades signals. Thanks to the

very short pulses transmitted in UWB systems, the reflected pulse has an extremely short window of opportunity to collide with the LoS pulse and to cause signal attenuation [64]. Besides, transmission powers of unlicensed UWB communications are normally restricted by national regulators. Thence, the low power transmission prevents UWB systems from interfering with other radio systems and achieves longer battery life for mobile devices. Finally, since UWB systems are carrierless, they have simpler transceiver architecture and need fewer RF components than narrowband systems, which makes them more cost effective.

Unique features and advantages make the UWB technology attractive for various applications such as:

- Multimedia communications: the high-data-rate capability of UWB systems for short distances has numerous applications for home networking and multimedia-rich communications in the form of wireless personal area network (WPAN) [64]. Providing wireless connections and high speed transmissions in multipath rich environments with coverage up to 20 m, the UWB technology helps users be able to interact with a cluster of interconnected multimedia devices, such as PCs, cameras, and printers, by a portable device.
- Radar systems: UWB radar pulses are shorter than the dimensions of targets, so signals reflected by targets change not only in amplitude and time shift, but also their impulse shapes. Hence, radar systems established on the UWB transmission exhibit extremely high resolution, and this property can be extended to additional applications such as underground, through-wall and ocean imaging, as well as medical diagnostics and border surveillance devices [65].
- Sensor networks: in a sensor network, a large number of nodes are spread across a geographical area, and low rate communications are combined with precise ranging and geolocation. Key requirements for sensor networks include low cost, low power consumption, and multifunctionality, which can be met by high data rate UWB

communication systems through gathering and disseminating or exchanging an enormous quantity of sensory data in a timely manner [66, 67]. The short-duration pulses also ensure very high time resolution for positioning of nodes.

2.3.2 Ultra-Wideband Antennas

As the equipment to capture and/or transmit radio electromagnetic waves, the UWB antenna is one of the essential elements to enable UWB systems. Based on discussion in Section 2.2, the smaller the antenna is, the narrower the maximum bandwidth will be. Accordingly, it is more challenging to design UWB antennas within limited space. In addition, with the increase of frequency, high order modes will occur and strongly affect the impedance matching and radiation feature. Thence, as well as reaching the bandwidth requirement, to provide stable system performance, UWB antennas are expected to exhibit consistent radiation behaviour over the entire operating frequency. Designs of UWB antennas have been explored for many years and common techniques to achieve UWB antennas include:

- Travelling wave antennas

Antennas like dipole antennas and patch antennas are resonant antennas where standing waves are supported. For this kind of antenna, their operating frequencies are closely related to lengths of structures. One approach to broaden bandwidths of antennas is to make them support travelling waves, which indicates that uniform patterns in current and voltage are distributed on the structures. Travelling wave antennas offer for the guided wave a smooth, almost not recognizable transition with the fields accelerated to free-space propagation speed. The helical antenna is a well-know representative of travelling wave antennas. As shown in Fig. 2.9(a), currents on helical antennas travel along the wire in the shape of a corkscrew. Etched on a dielectric substrate as shown in Fig. 2.9(b), the Vivaldi antenna guides the wave from the feed in a slot line to a wide-band taper, which provides all frequencies within the given bandwidth with proper radiation condition. The

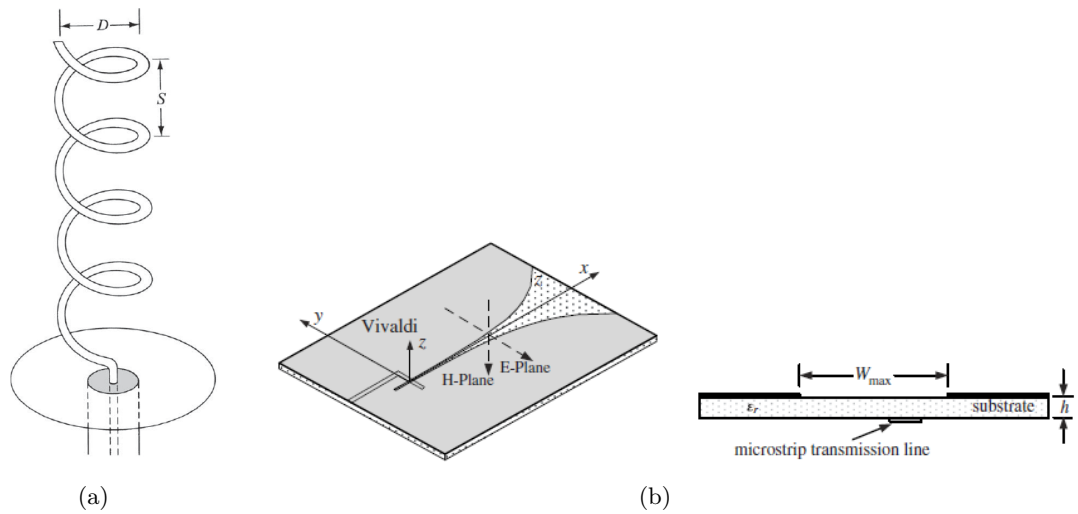


Figure 2.9: Illustrations of (a) helical antenna and (b) Vivaldi antenna [4].

low-profile characteristic makes the Vivaldi antenna well suited for direct planar integration and also for UWB antenna arrays for radar and communications [68].

- Frequency independent antennas

Characteristics such as impedance, radiation pattern, polarization, and so forth, are invariant over an ultra-wide frequency band for frequency independent antennas. This is based on the scaling characteristics of antenna modeling, and to satisfy this, the shape of an antenna should completely be specified by angles. Common frequency independent antennas are the spiral antenna (shown in Fig. 2.10(a)) and the log-periodic antenna (shown in Fig. 2.10(b)).

- Antennas with multiple resonances

By creating multiple resonances and combining them, UWB antennas can be achieved on standing wave antennas like the dipole antenna and PIFA. Through exciting two resonant modes controlled by two radiating arms as shown in Fig. 2.11(a), Chi *et al.* [5] achieved a broadband planar dipole antenna with a step-shaped feed gap to operate over 470-806 MHz with VSWR less than 2.5. See *et al.* [6] proposed an UWB antenna consisting of a driven F-shaped element and a parasitic L-shaped element as illustrated in Fig. 2.11(b). Using a broadband rectangular feeding struc-

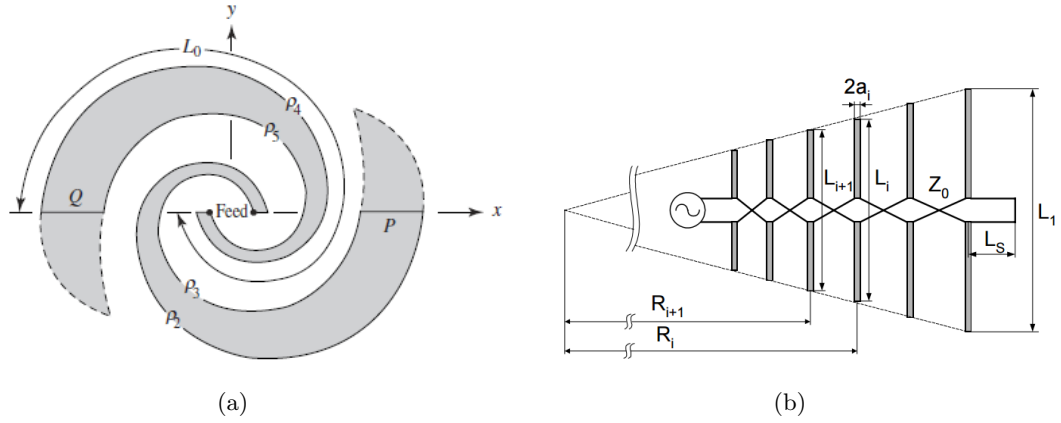


Figure 2.10: Illustrations of (a) spiral antenna and (b) log-periodic antenna [4].

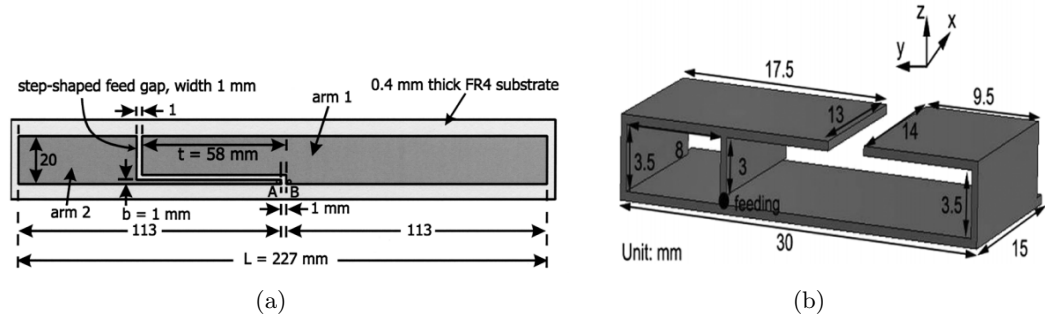


Figure 2.11: Illustrations of two UWB antennas with multiple resonances [5, 6].

ture, the planar inverted-F-L antenna (PIFLA) achieved $|S_{11}| \leq -10 \text{ dB}$ from 2.8 to 5.6 GHz

In addition to the antennas introduced above, the horn antenna, Yagi-Uda antenna, bow-tie antenna, conical antenna, self-complimentary antenna, etc. are also commonly used in UWB systems. This thesis focuses on exciting multiple resonances, having neighboring resonant frequencies, with the help of CMA to achieve UWB performance.

2.4 Characteristic Mode Theory

The TCM was first developed by Garbacz [21] in 1968, and later refined by Harrington and Mautz [22, 23] in 1971. Garbacz obtained the modes of a conducting body with

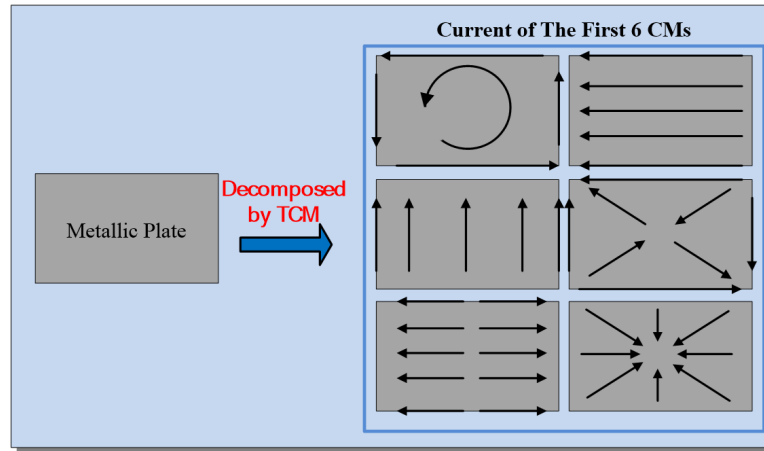


Figure 2.12: Illustration of modal decomposition on a metallic plate.

arbitrary shape by diagonalizing the scattering matrix. Alternatively, Harrington and Mautz arrived at the same results by diagonalizing the generalized impedance matrix of the body. Offering a physical explanation for radiation mechanisms of antennas, the CMA provides one of the methodologies for antenna design. With current distribution and radiation ability of each mode given by the CMA, antenna structures could be efficiently optimized. In addition, different feeding techniques are able to be applied to excite the desired characteristic modes. In this thesis, all simulations related to the CMA are carried out in the commercial electromagnetic simulation software FEKO, while the final antenna optimizations are carried out in the CST Microwave Studio.

2.4.1 Physical Interpretations of Characteristic Modes

Fig. 2.12 gives the first 6 modes of a metallic plate. According to the TCM, these modal currents and their corresponding far-field radiations are orthogonal to each other. Besides, the characteristic modes are only related to the geometry and material of the structure at a certain frequency. To evaluate the characteristics of a mode with and without excitation, key parameters like eigenvalue, modal weight coefficient, modal excitation coefficient, etc. are introduced.

2.4.1.1 Eigenvalue

The eigenvalue (χ_n) is introduced to predict modal capabilities of radiation and energy storage, and it is defined as:

$$\mathbf{X}(\mathbf{J}_n) = \chi_n \mathbf{R}(\mathbf{J}_n) \quad (2.11)$$

where \mathbf{J}_n is the eigencurrent of the n^{th} mode, and \mathbf{X} and \mathbf{R} are reactance and resistance operators, respectively.

Eigenvalue χ_n can be derived by a ratio of the inner products based on (2.12) and it ranges from $-\infty$ to ∞ . According to the deduction in (2.12), where '*' is the notation for conjugate transpose operator, $P_{rect,n}$ is the modal energy storage power and $P_{rad,n}$ is the modal radiation power, a characteristic mode with $\chi_n < 0$ stores electrical energy, whereas a mode with $\chi_n > 0$ stores magnetic energy. A characteristic mode with $\chi_n = 0$ is at resonance, and all energy is radiated.

$$\chi_n = \frac{\langle \mathbf{J}_n^*, \mathbf{X}(\mathbf{J}_n) \rangle}{\langle \mathbf{J}_n^*, \mathbf{R}(\mathbf{J}_n) \rangle} = \frac{P_{rect,n}}{P_{rad,n}} \quad (2.12)$$

2.4.1.2 Modal Significance

For an antenna mainly radiates by a single mode, we can study the eigenvalue of this mode near its resonant frequency. However, for UWB antennas contributed by multiple modes resonating at separate frequencies, their eigenvalues can have significant differences over the wide frequency band, which results in the plot of the eigenvalue against the frequency having a large vertical range and it is difficult to be distinguished near $\chi_n = 0$. Therefore, the modal significance (S_n) is used to compare the significance of each mode, and it is defined as:

$$S_n = \left| \frac{1}{1 + j\chi_n} \right| \quad (2.13)$$

in which $j = \sqrt{-1}$.

According to (2.13), when a mode is at resonance (i.e. $\chi_n = 0$), its significance is 1. If most energy is stored (i.e. $\chi_n \rightarrow \pm\infty$), the significance of this mode is close to 0. Hence, the modal significance S_n ranges from 0 to 1, and modes with significances close to 0 contribute little to radiation, while modes with S_n close to 1 radiate significantly.

2.4.1.3 Modal Characteristic Angle

According to the discussion above, the modal significance describes the radiation ability of a mode, but it fails to reveal whether the stored energy is electrical or magnetic. Characteristic angle (a_n) is therefore employed as another important quantity to describe eigenvalue and it is acquired from:

$$a_n = 180^\circ - \tan^{-1}(\chi_n) \quad (2.14)$$

Characteristic angles are between 90° and 270° . Resonance occurs while a_n is 180° , and otherwise the structure stores electrical energy when $180^\circ < a_n < 270^\circ$, or magnetic energy when $90^\circ < a_n < 180^\circ$. Capable of indicating the type of energy stored by a mode and has a reasonable variation range, the characteristic angle is mainly used in this thesis to discuss UWB antennas achieved by exciting multiple resonating modes.

2.4.2 Bandwidth Estimation

The radiating bandwidth of a mode (B_n) is normally defined as the range of frequencies within which the power radiated by the mode is no less than the power stored by it [69], i.e. $|\chi_n| \leq 1$ according to the definition of eigenvalue given in (2.12).

Take $|\chi_n| = 1$ into (2.13), we can obtain

$$S_n = \left| \frac{1}{1 \pm j} \right| = \frac{1}{\sqrt{2}} \quad (2.15)$$

Furthermore, take $|\chi_n| = 1$ into (2.14), we can obtain

$$\begin{aligned} a_n &= 180^\circ - \tan^{-1}\left(\pm \frac{\sqrt{2}}{2}\right) \\ &= 225^\circ \text{ or } 135^\circ \end{aligned} \quad (2.16)$$

Thus, within the modal radiating bandwidth, the modal significance and characteristic angle satisfy $\frac{1}{\sqrt{2}} \leq S_n \leq 1$ and $135^\circ \leq a_n \leq 225^\circ$.

2.4.3 Excitation of Characteristic Modes

Previous discussions about characteristic modes focus on understanding characteristics of radiating bodies without considering excitations. Given by the TCM in [22], a modal solution for the resultant current \mathbf{J} on a conducting body defined by S in an impressed electric field \mathbf{E}_{in} is a linear superposition of the modal currents \mathbf{J}_n , which is expressed as

$$\mathbf{J} = \sum \alpha_n \mathbf{J}_n \quad (2.17)$$

where α_n is the weight contributed by the n^{th} characteristic mode and it is calculated by

$$\alpha_n = \frac{V_n^i}{1 + j\chi_n} \quad (2.18)$$

in which V_n^i is the modal excitation coefficient, and it is computed by the surface integral as

$$V_n^i = \iint \mathbf{J}_n^* \cdot \mathbf{E}_{in} dS \quad (2.19)$$

Input impedance (Z_{in}), which is important in antenna engineering for matching, can be obtained with the current I_{in} and the voltage V_{in} at the feeding port given as follows

$$I_{in} = \sum \alpha_n J_n^P \quad (2.20)$$

and

$$V_{in} = E_{in}^P \quad (2.21)$$

where J_n^P and E_{in}^P are current and electric field at the feeding port, respectively. Since the input impedance does not satisfy a linear combination, input admittance (Y_{in}), the reciprocal of the input impedance, is given instead as

$$Y_{in} = \frac{I_{in}}{V_{in}} = \sum \frac{V_n^i J_n^P}{1 + j\chi_n} = \sum Y_{in}^n \quad (2.22)$$

According to (2.22), the input admittance is the sum of modal admittances (Y_{in}^n). Thus the modal reflection coefficient (Γ_n) can be acquired from

$$\Gamma_n = \frac{\frac{1}{Y_{in}^n} - Z_0}{\frac{1}{Y_{in}^n} + Z_0} \quad (2.23)$$

where Z_0 is the port impedance.

2.4.4 State-of-the-art Review of Characteristic Mode Analysis on Antenna Designs

The CMA has been applied in various applications including mutual coupling reduction, pattern synthesis, bandwidth enhancement, feeding location selection, etc. and some representative work in recent years is summarized below:

- Platform-conformal/platform-embedded antenna design

The large wavelength of decameter wave brings a lot of practical difficulties to the design of shipboard, vehicular, and aircraft antennas in high frequency (HF) and VHF bands. Besides, antenna performance may deteriorate after being integrated into devices. Instead of tedious trying and evaluating system performance of antennas at different mounting locations, design and deployment of antennas could benefit a lot if electromagnetic characteristics of platforms are known in advance [70–73]. To overcome the difficulty of implementing low coupling multi-

antennas operating below 1 GHz in compact mobile handsets, Li *et al.* [70] created multiple characteristic modes by manipulating the chassis structure, and they realized the multi-antenna structure by exciting these modes individually. Chen and Wang [71] solved characteristic modes to understand the resonant behavior of a ship platform. By making use of these modes, they synthesized radiating currents for the designated radiation patterns. Consequently, the superstructure of the ship acted as the main radiator to operate at 5 MHz.

- Multiple-input multiple-output antenna design

Using only one element to radiate multiple modes with different radiation patterns, multimode antennas avoid the large spatial requirements of conventional multiple-input multiple-output (MIMO) antenna arrays and can be a very competitive candidate in the construction of a massive MIMO systems. The idea of using CMA to identify different radiating modes and choose excitation mechanisms for them to achieve multimode MIMO antennas was firstly introduced by Antonino [74] in 2009. Later, Araghi and Dadashzadeh [75] analyzed the first seven characteristic modes of a triangular-shaped radiator. Exciting the first two characteristic currents that resonate at the same frequency, they obtained two orthogonal radiation patterns, which resulted in the antenna having pattern diversity for MIMO applications. Manteuffel and Martens [76] excited four characteristic modes on a square plate to achieve a compact multimode antenna element with four ports. Afterwards, they extended the optimized 4-port antenna element to a 11×11 array having 484 ports.

- Feeding structure design

With modal current distributions given by CMA, special feeding structures can be designed to excite the desired modes efficiently. Antonino *et al.* [77] proposed a square planar monopole antenna with a double feed. They excited the radiator at two symmetrical points to generate a pure and intense vertical current distribution in the whole structure, and to avoid the horizontal currents that degrade

the polarisation properties and the impedance bandwidth performance. Synthesized currents of the platform-conformal HF shipboard antenna proposed in [71] were excited with inductive coupling elements (ICEs) achieved through cutting nonprotruding slits with voltage sources. Bohannon and Bernhard [78] proposed a novel technique to calculate a quasi-optimal aperture excitation for finite size UWB antenna arrays. The approach was based on using the characteristic modes of the arrays mutual impedance matrix, and the proposed characteristic mode taper provided for wideband matching of all array elements, including those at the edges of the finite array.

- Bandwidth study

By observing and manipulating different characteristic modes, bandwidth properties of antennas can be explored with the help of CMA. Adams and Bernhard [79] investigated the potential of a TM₁₀ antenna by examining different characteristic modes, and the antenna bandwidth was nearly doubled by combining multiple resonances. Wu and Zhang [80] discussed the operating mechanism of an UWB antenna working from 2.8 GHz to 12 GHz from the point of CMA. Effects of ground plane and miniaturization of the antenna by chopping it in half were also discussed by analyzing modal current distributions and VSWRs. Antonino *et al.* [81] embedded a thin slot into an UWB antenna having VSWR less than 2 over 3-12 GHz, and they used CMA to explain the effect of the slot mode to the antenna's band-notched behavior.

2.5 Summary

This chapter presents the fundamental concepts of IoT systems, small antennas, UWB technologies, and the TCM. Antenna miniaturization techniques and state-of-the-art applications of CMA are demonstrated. Additionally, representative UWB antennas are presented.

Chapter 3

Design of a Narrowband Miniaturized Circular Antenna

3.1 Introduction

With the boom of portable IoT devices built in limited areas [82, 83], the demand for compact and low-profile antennas is increasing. This chapter proposes a very low-profile UHF small antenna. The related work on small antennas and the main contributions of this chapter are reviewed in Section 3.1. The proposed radiating body and ground plane are analyzed and modified with CMA in Section 3.2. Section 3.3 discusses modes of the proposed radiator when printing it on different substrates. Next, the feeding structure is designed in Section 3.4. Simulation and measurement results are presented and discussed in Section 3.5. Finally, Section 3.6 concludes this chapter.

3.1.1 Related Work

Extensive research has been devoted to miniaturized and low-profile antenna designs. Monti *et al.* [84] proposed a compact UHF planar antenna. Fractal techniques and

appropriate shorting posts were used to significantly reduce the antenna size to $0.19\lambda \times 0.22\lambda$. Its size reduction with respect to a rectangular patch antenna was 89.8%; whilst an 85.5% and a 45.8% size reduction were reached when the same structure was compared to the fractal and the short-circuited patch antennas respectively. Hong and Sarabandi [82] proposed an extremely short monopole antenna with omnidirectional radiation pattern and vertical polarization. The concept was based on superposition of multiple quarter-wave segments that are meandered and spiraled around to suppress the radiation from horizontal currents above the ground plane. Operating at around 460 MHz, the antenna was around $\lambda/30$ in height and $\lambda/10$ or smaller in lateral dimension.

Providing full characteristics of a radiating body with arbitrary geometry, CMA has been used to analyze and design several small antennas. Ma *et al.* [85] wrapped and flattened the common PIFA to have a circular ground patch in the center and a circular arm along the circumference. The novel circular co-planar inverted-F antenna operated at 480 MHz with radius less than 0.1λ and height less than 0.005λ . Chen and Wang [86] took an electrically small unmanned aerial vehicle (UAV) platform as the radiating aperture and used compact and low-profile probes to excite currents on the UAV body. Their concept avoided mismatching problems caused by the low resistance and large reactance that are always faced in conventional electrically small antennas.

3.1.2 Contributions

Motivated by the previous work, this chapter proposes a miniaturized UHF antenna for IoT applications. Operating at 474 MHz, the small antenna is very low profile with a lateral radius of 0.052λ and a height of 0.005λ . Its miniaturization is based on novel structure design with CMA. The main contributions of this chapter are summarized as follows:

- The shape of a typical monopole is transformed to achieve a compact and low-profile antenna. The ground plane for a monopole is transformed into a small

disk and the monopole is placed in the same plane of the disk and bent around it to become a circular arm. The CMA is carried out to understand the proposed structure from the point of TCM.

- Based on the current distribution of the significant mode, the disk ground plane is modified to different rings. Afterwards, the final ground plane is determined based on modal current and field distributions as well as the eigen values.
- CMA is then performed to discuss the effect of the height of the substrate on the resonant frequency, and thence complete the guidelines of the radiator design.
- A feeding loop is designed to excite the radiator, and its effects on modal excitation coefficient and resonant frequency are explored.
- A prototype of the proposed antenna is fabricated and measured. Eigen values of the final structure with coaxial cable having different lengths are simulated to analyze the difference between results of simulation and measurement.

3.2 Radiating Body Design and Characteristic Mode Analysis

3.2.1 Circular Radiating Body with Disk Ground Plane

Monopoles have been widely adopted for wireless communications during the last decades. It typically has a length of about $\lambda_0/4$ at resonant frequency f_0 , where λ_0 is the wavelength in free space at f_0 . However, the monopole has a high profile because its pole is vertical to the ground plane. In this chapter, a small radiating body with very low profile is designed by shape transformations on the monopole. The ground plane in a typical monopole is transformed into a small disk ground plane with a radius of r_3 . The monopole is placed in the same plane of the disk and bent around the disk to become a circular arm with outer radius of r_1 and inner radius of r_2 , as shown in Fig. 3.1. The

width and average radius of the arm are $w_1 = r_1 - r_2$ and $r_0 = (r_1 + r_2)/2$, respectively. The arc between the open and the short end of the arm is defined as θ .

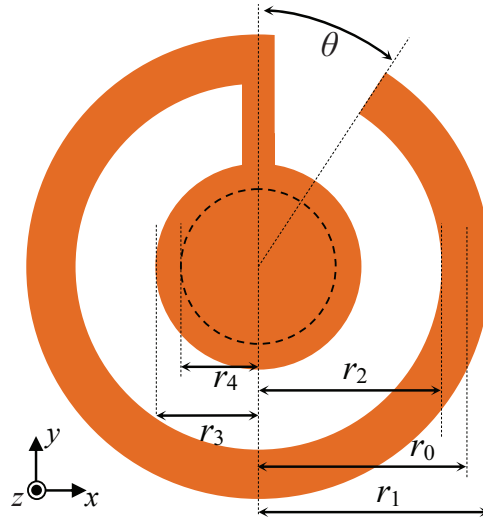


Figure 3.1: The proposed planar circular radiating body with a disk ground plane.

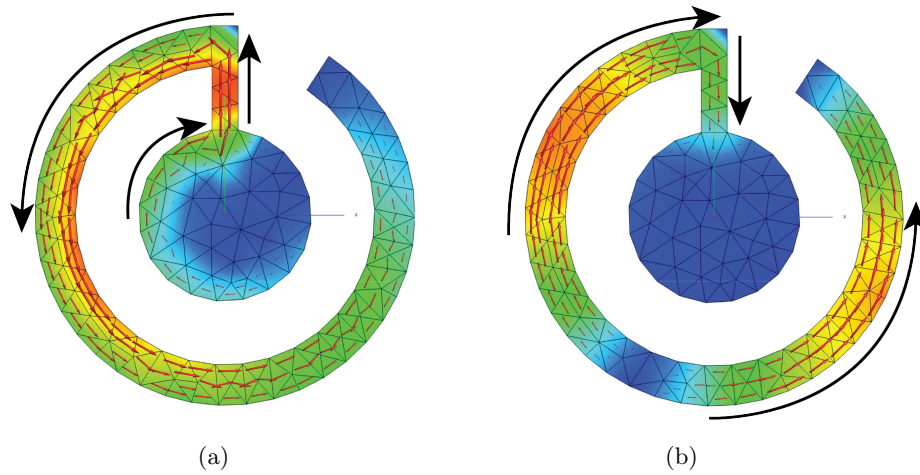


Figure 3.2: Current flows of (a) mode 1 and (b) mode 2.

To better understand and optimize the structure, CMA is carried out on a generic model of the proposed radiating body and modal current flows of the first two significant modes are illustrated in Fig. 3.2. In Fig. 3.2(a), the modal current distribution of mode 1 on the circular arm decreases gradually from the short end to the open end, which is

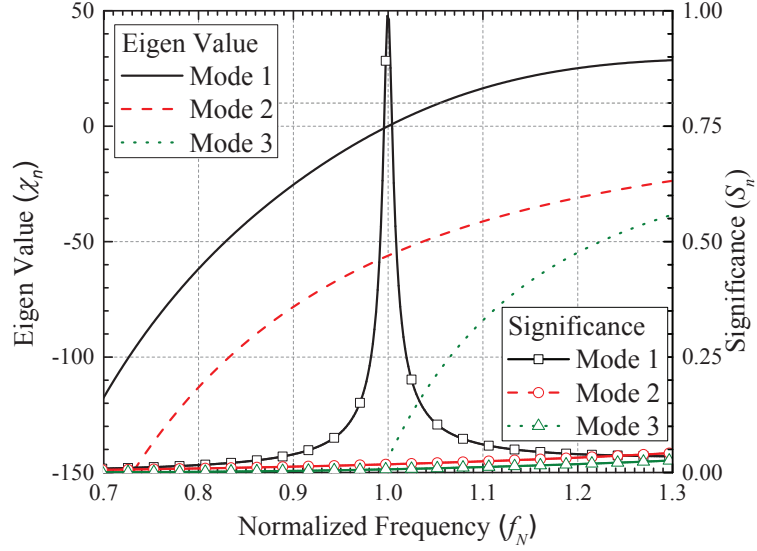


Figure 3.3: Eigen values and modal significances for the first three modes on the structure shown in Fig. 3.1.

similar to that of a typical monopole in its vertical form. However, there are two peaks in the current distribution of mode 2 as shown in Fig. 3.2(b). The mode 1 is therefore selected for the proposed circular radiating body.

The proposed radiating body should tune the resonant frequency of mode 1 at f_0 and suppress the higher modes. According to Chapter 2.4, modes with eigen value $\chi_n = 0$ ($n = 1, 2, \dots$) are at resonance and radiate most efficiently. Based on extensive CMA simulations, mode 1 can resonate at f_0 when the proposed radiating body is at settings of

$$\begin{aligned} r_1 : r_2 : r_3 : \lambda_0 &= 0.065 : 0.051 : 0.03 : 1 \\ \theta &= \pi/6 \end{aligned} \quad (3.1)$$

The effective length of the circular radiating body can be then defined as

$$l_e = \frac{r_0 + r_3}{2} (2\pi - \theta) \quad (3.2)$$

which is about $\lambda_0/4$ similar to a typical monopole.

The eigen values and modal significances of the first three modes for the radiating body with settings in (3.1) are illustrated in Fig. 3.3, where frequency f is normalized to f_N using

$$f_N = f/f_0 \quad (3.3)$$

At $f_N = 1$, χ_1 is equal to 0, while χ_2 and χ_3 are far away from 0. Similarly, S_1 is equal to 1 at $f_N = 1$, while S_2 and S_3 are very small and near 0, which means that mode 1 is the most significant mode at the resonant frequency. This is consistent with modal current distributions shown in Fig. 3.2.

3.2.2 Radiating Bodies with Different Ground Planes

In Fig. 3.2(a), modal currents on the disk are flowing mostly along the left edge. There is hardly any current flow in the center and upper right area of the disk ground plane, which hints that the impact on the current flow could be slight when these areas are removed. Fig. 3.4 illustrates three modified structures with different ring ground planes named as *ring 1*, *ring 2* and *ring 3*. *Ring 1* is formed by only removing the center area with a radius of r_4 from the disk. Simulations show that when $r_4 = 0.022\lambda_0$, impacts on the current flow between radiating body with the disk and the ring ground plane are slight. Based on *ring 1*, *ring 2* is formed by removing the upper right part with arc of

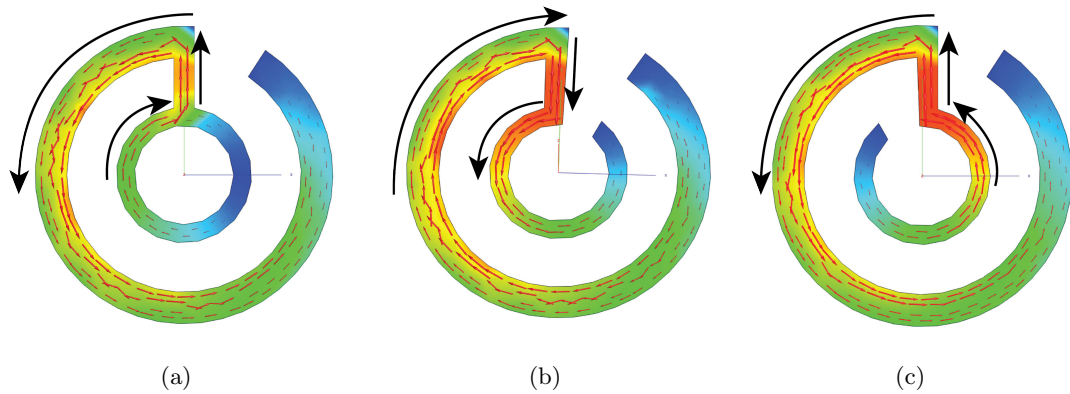


Figure 3.4: Structures with variant grounds and their current flows of mode 1: (a) *ring 1*, (b) *ring 2*, and (c) *ring 3*.

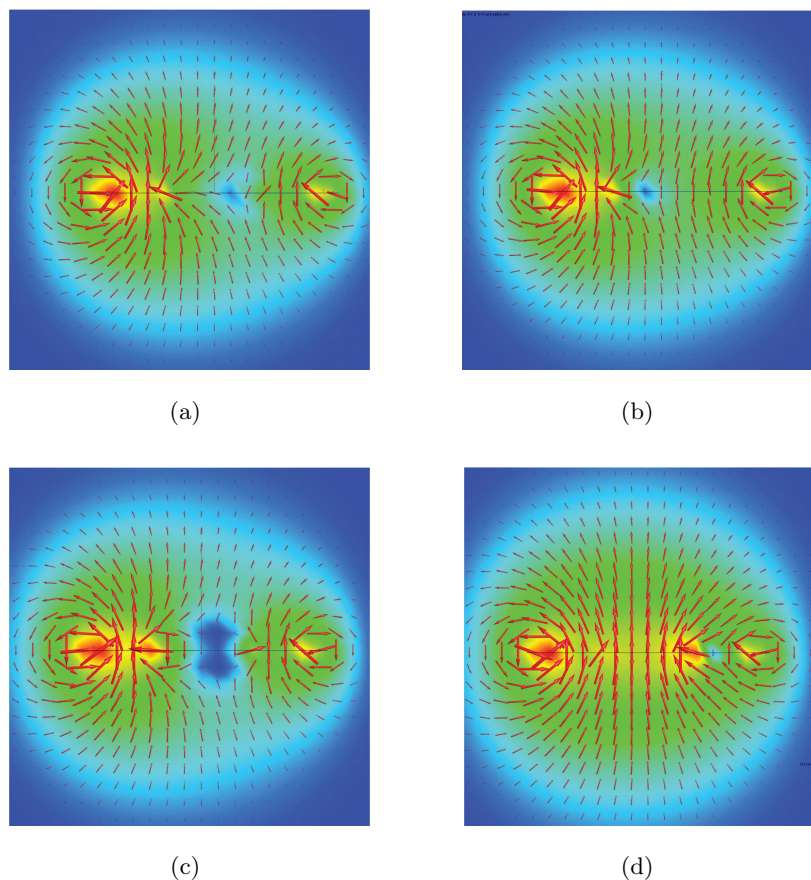


Figure 3.5: Near H-fields in the xz -plane of mode 1 for radiating bodies with different ground planes: (a) disk, (b) *ring 1*, (c) *ring 2*, and (d) *ring 3*.

θ from the whole ring, while *ring 3* is formed by removing the upper left part with arc of θ from the whole ring.

As shown in Fig.3.4(a) and Fig. 3.4(b), the current flows on both *ring 1* and *ring 2* are in the opposite rotation direction to the current flows on the arm, which is the same as the radiating body with disk ground plane in Fig. 3.2(a). However, having an upper left cut, the current flow on *ring 3* is forced in the same rotation direction as the current flow on the circular arm as shown in Fig. 3.4(c), and therefore stronger and more uniform near H-field is generated, as shown in Fig. 3.5. Near H-fields in Fig. 3.5(a)-(c) are very similar, and their magnitudes around the arm are strong while those around the center are weak. However, the near H-field for *ring 3* in Fig. 3.5(d) is nearly uniform

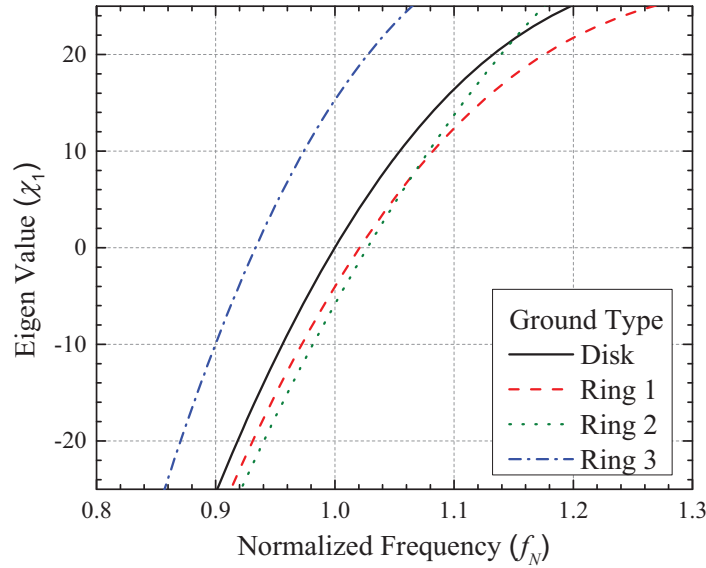


Figure 3.6: Eigen values of radiating bodies with different ground planes.

from the center to the outer edge of the structure. Thus, the radiating body with *ring 3* is more constructive and efficient.

The eigen value χ_1 for each ground plane is plotted in Fig. 3.6. Curves of χ_1 for radiating bodies with *ring 1* and *ring 2* are on the right side and close to the one for using the disk ground plane. This verifies again that the effect of cutting the central area of the disk ground plane is slight, and the proposed radiating bodies with disk, *ring 1* and *ring 2* ground planes have similar radiation behaviors and resonant frequencies. The curve of χ_1 for *ring 3* is on the left side to the curve for the disk, and both curves have similar trend except that there is a wide gap between them. This indicates that the radiating body with *ring 3* not only has the similar radiation behavior as the disk, but also supports lower resonant frequency.

Radiation patterns for the proposed radiating bodies with different ground planes are given in Fig. 3.7. Good agreements are observed in radiation patterns for radiating bodies with different ground planes, especially for disk, *ring 1* and *ring 2*. The radiation pattern for *ring 3* is slightly more omni-directional in the E-plane than patterns for other ground planes. These omni-directional radiation patterns in E-plane are prima-

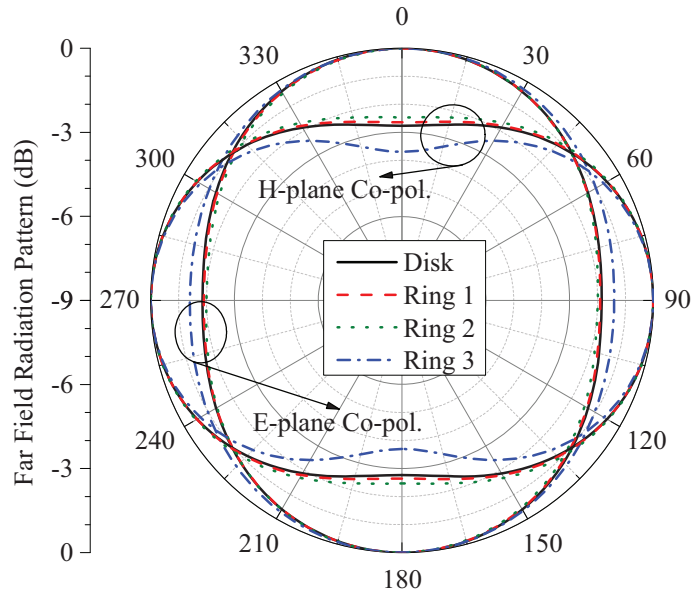


Figure 3.7: Far-field radiation patterns of radiating bodies with different ground planes.

rely resulted from that their circular arm carries current flows with strong magnitudes, and the radiating body generates magnetic field lines passing through most of the area surrounded by the circular arm as shown in Fig. 3.5.

With the aforementioned physical insights via CMA, the radiating body with *ring 3* is selected for design of the antenna with a feeding structure.

3.3 Proposed Radiator on Substrate

Although the proposed structure can be realized by only a thin metal layer, it is more practical to fabricate it on the metal attached to the dielectric substrate by adopting PCB technologies. Therefore, Rogers 5880 substrate with the relative dielectric constant of $\epsilon_r = 2.2$ and height of h is used to model a practical antenna.

The value of h is swept to study performance of the proposed structure on dielectric substrates. The eigen values of radiators with different h are given in Fig. 3.8, indicating that the radiating body with a substrate has lowered resonant frequency. Thus, a smaller

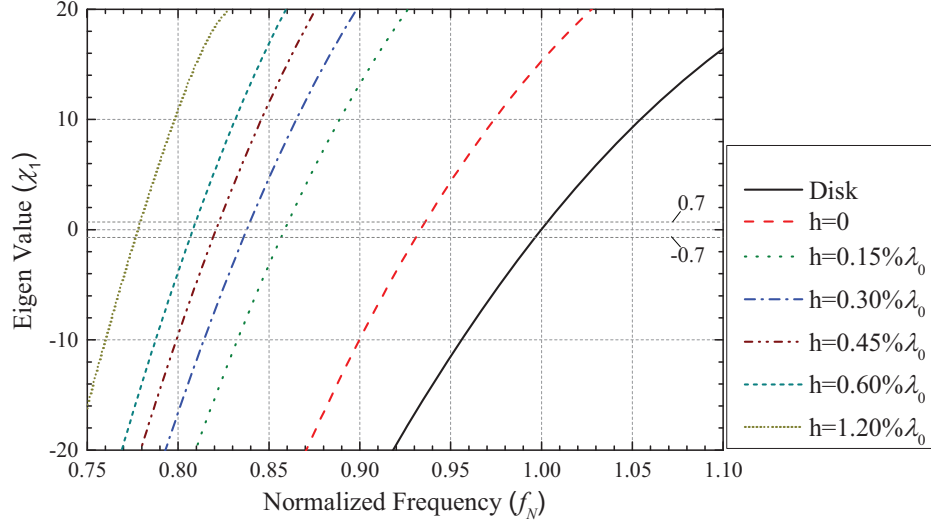


Figure 3.8: Eigen values χ_1 of radiators with substrates at different thicknesses represented by h in terms of λ_0 .

Table 3-A: Normalized resonant frequencies.

h (percentage of λ_0)	0	0.15	0.30	0.45	0.60	1.20
Normalized resonant frequencies (f_{Nc})	0.93	0.86	0.84	0.82	0.81	0.78

antenna can be achieved at the same frequency with existence of a substrate. The normalized resonant frequencies with respect to the resonant frequency of using the disk ground plane for different h are directly obtained from Fig. 3.8 and they are given in Table 3-A as f_{Nc} .

Thence, the proposed radiator can be generally designed at any desired resonant frequency with the aid of Table 3-A and the geometric settings given in (3.1). Considering the tradeoff between very low profile along z -axis and small size in xy -plane, substrate with height of $h = 0.006\lambda_0$ is selected for design of an example UHF radiator operating at its resonant frequency $f_c = 474$ MHz ($\lambda_c = 632$ mm). The radiator is designed through the following process:

- First, according to (3.3), the reference resonant frequency f_0 can be determined by

$$f_0 = f_c / f_{Nc} \quad (3.4)$$

when $f_c = 474$ MHz and $f_{Nc} = 0.81$ for $h = 0.006\lambda_0$ are replaced in (3.4), $f_0 = 585$ MHz can be obtained;

- Then, the corresponding wavelength is calculated as $\lambda_0 = c_0 / f_0 = 512$ mm, where c_0 is the light speed in free space;
- Finally, according to (3.1), the geometric parameters of the example radiator are obtained as $r_1 = 33$ mm (about $0.052\lambda_c$), $r_2 = 26$ mm, $r_3 = 15$ mm, $r_4 = 11$ mm and $h = 3.1$ mm (about $0.005\lambda_c$).

3.4 Proposed Radiator with a Feeding Loop

Previously, the CMA has been utilized to understand the proposed radiating body without considering exciting sources. In this section, combining the radiator and a feeding loop on different sides of the substrate, a planar circular antenna is illustrated in Fig. 3.9(a).

A typical modal flow of mode 1 for the antenna with feeding loop is given in Fig. 3.9(b). It is clear that the rotation directions of current flows on the radiator and the feeding loop are opposite. This indicates that the feeding loop and the radiator act as an air core transformer, which transfers the power from its feed port to the load by magnetic coupling. Around the resonant frequency of mode 1 for the proposed radiating body, the eigen values of higher modes would be far away from zero. Moreover, according to (2.17) given in Chapter 2, if the small loop is placed near the strip connecting the inner ring and the outer circular arm, where the magnitude of the current flow of mode 1 is strongest and the one of mode 2 is weak, J_1 will be the only modal current with

significant coefficient.

The main function of the feeding loop is to excite mode 1 to transfer the energy from source to the radiator, which is equivalent to realize the impedance matching between source and radiator excited in mode 1. The function can be realized by adjusting the

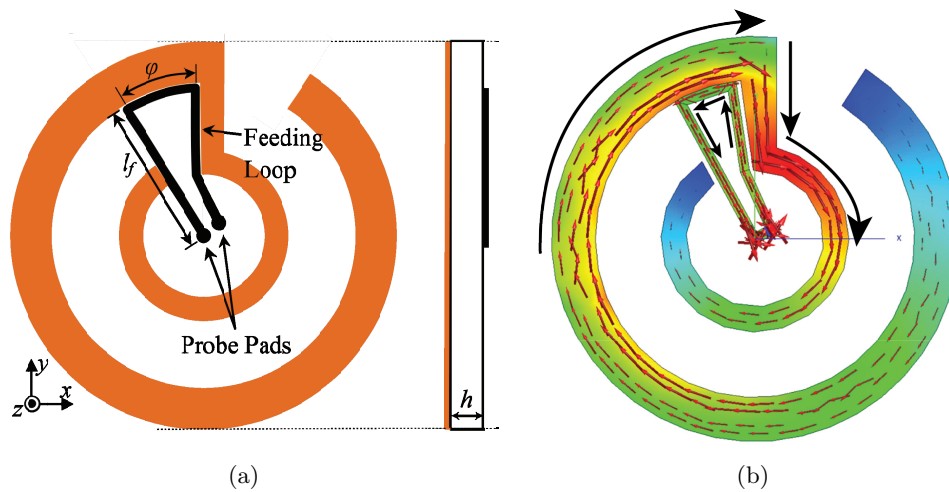


Figure 3.9: (a) Structure layout of the proposed circular antenna with a feeding loop. (b) The current flow of mode 1 for the antenna.

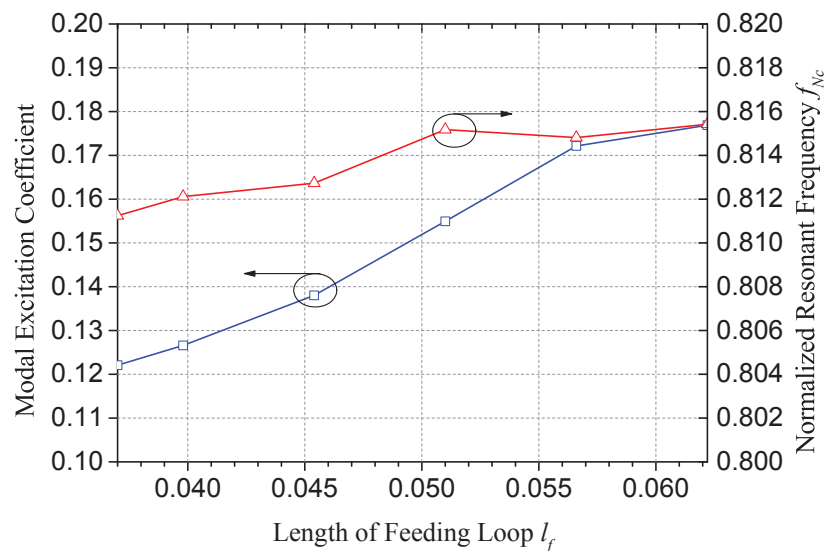


Figure 3.10: Modal excitation coefficients (2.19) and normalized resonant frequencies of mode 1 with respect to length of the feeding loop l_f .

size of the feeding loop. As shown in Fig. 3.9(a), the area of the feeding loop can be controlled by adjusting the length and arc of the feeding loop, indicated as l_f and ϕ . When $\phi = \pi/9$, the modal excitation coefficients and normalized resonant frequency (f_{Nc}) of mode 1 with respect to l_f are extracted from a series of simulations. According to (2.19), the modal excitation coefficient is the inner product of the modal current and the impressed electric field. Since the modal currents are independent of each other, the modal excitation coefficient does not exist a fixed threshold, and its variation trend for a specific mode should be considered to evaluate effects of different feeding structures on this mode. From results given in Fig. 3.10, when l_f increases, resulting in the increase of the loop coupling area, the modal excitation coefficient of mode 1 increases significantly, while its normalized resonant frequency increases slightly. It means that the modal excitation coefficient can be directly adjusted by l_f , and the effect of the feeding loop on the resonant frequency is small.

3.5 Simulation and Measurement Results and Analyses

An example of the proposed circular antenna operating at 474 MHz is then modeled and simulated in the CST microwave studio with parameters of $r_1=33$ mm, $r_2=26$ mm, $r_3=15.5$ mm, $r_4=11.5$ mm and $h=3.1$ mm. The antenna was fabricated and measured at QMUL. The prototype is shown in Fig. 3.11(a) and (b) where a customized SMA connector is soldered on the probe pads through holes.

Fig. 3.12 presents the VSWR and radiation efficiency of the proposed antenna. Resonant frequency and $VSWR < 2$ bandwidth are about 474 MHz and 2.2 MHz in simulation, and 471 MHz and 3.3 MHz for measurement. The simulated radiation efficiency is 84% at 474 MHz. The measured VSWR has a lower center frequency and a wider bandwidth than the simulated one, which will be discussed later. The radiation patterns of the proposed antenna is also simulated by CST and given in Fig. 3.13. It is clear that the radiation patterns of the proposed antenna agree well with the ones of the radiator

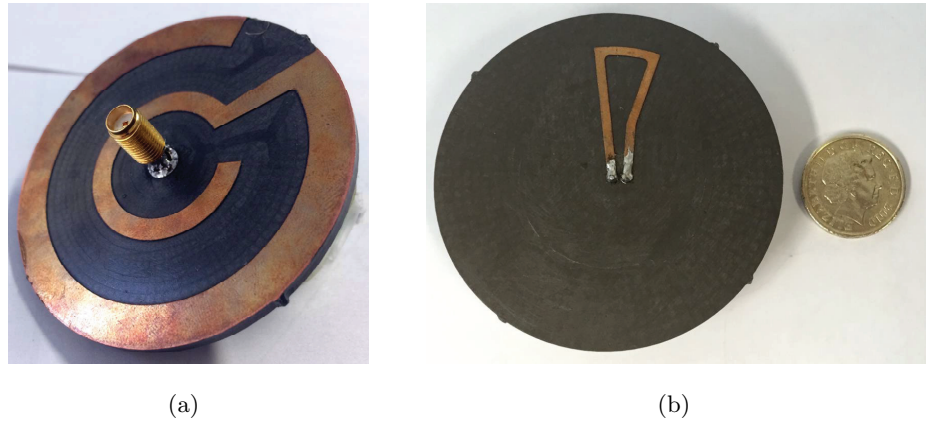


Figure 3.11: Prototype of the proposed antenna: (a) radiator side view and (b) feeding loop side view. ($r_1=33\text{mm}$, $r_2=26\text{mm}$, $r_3=15.5\text{mm}$, $r_4=11.5\text{mm}$, and $h=3.1\text{mm}$ corresponding to parameters in Fig. 3.1).

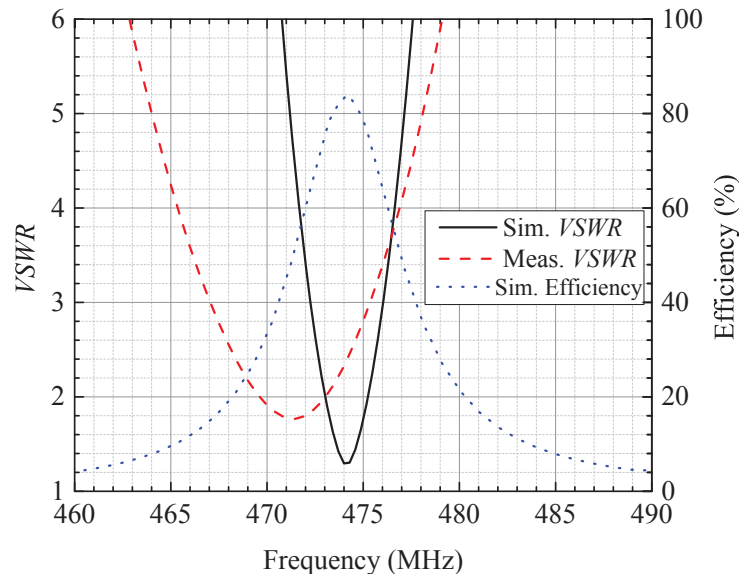


Figure 3.12: VSWR and radiation efficiency of the proposed antenna.

given by CMA. This means the radiation patterns of the CMA can be used to predict the radiation behavior of the proposed antenna.

As shown in Fig. 3.11(a), the antenna prototype is measured with a SMA connector and test cable, which generally affects the near field around the radiating body for such a UHF band compact antenna with small ground structure although calibration is carried

out. To make sure the difference between simulation and measurement results in Fig. 3.12 is introduced by the measurement setup, CMA is carried out again with cables having different lengths of l . As shown in Fig. 3.11(a) and (b), the cable is located in the center of the proposed antenna, and Fig. 3.14 gives the χ_1 obtained with corresponding l .

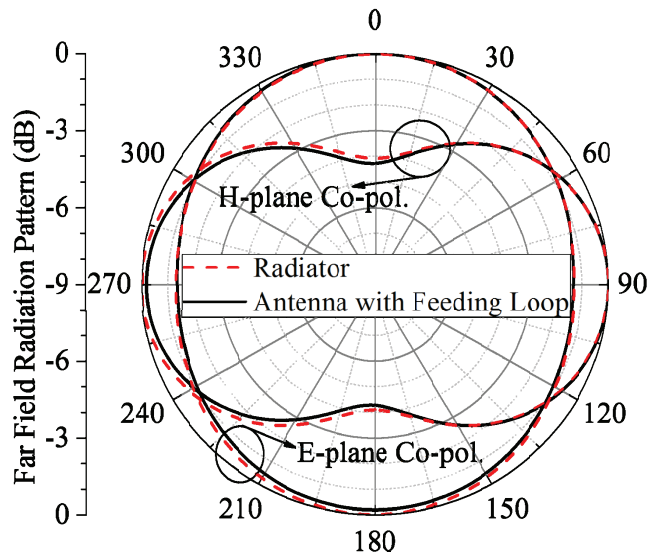


Figure 3.13: Radiation patterns of the proposed antenna.

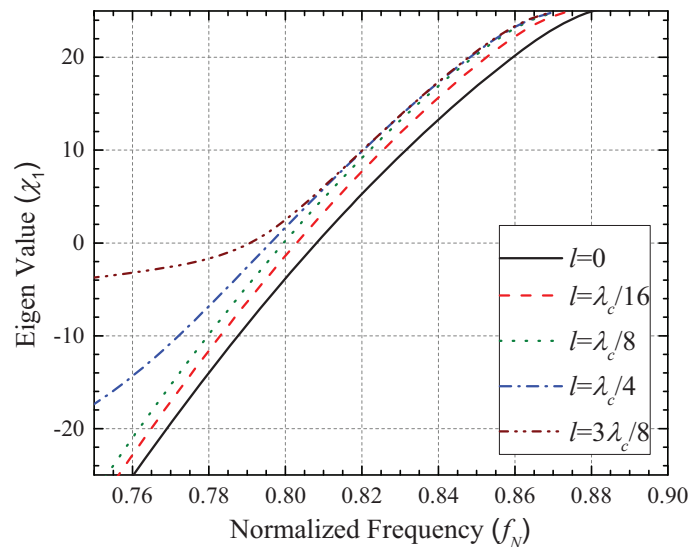


Figure 3.14: Eigen value χ_1 of the proposed circular radiator with a test cable at different lengths.

It can be observed that the resonant frequency of the antenna decreases when the

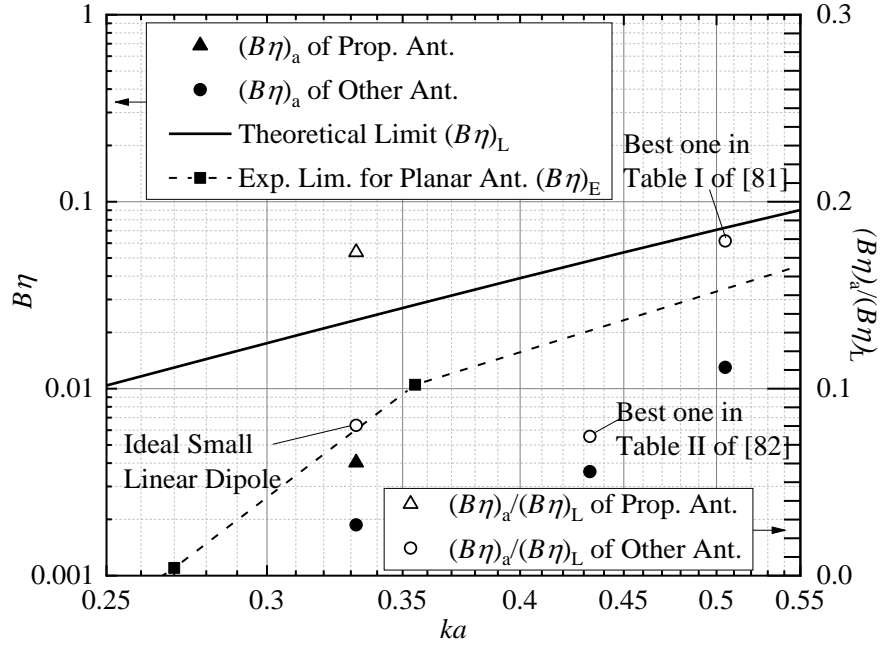


Figure 3.15: Comparison of bandwidth-efficiency product between the proposed antenna and other antennas.

length of cable increases. When $l < (\lambda_c/8)$, only resonant frequency decreases slightly while the fractional bandwidth remains unchanged, indicated by the unchanged slope around the resonant frequency. When $l > (\lambda_c/4)$, resonant frequency still decreases while the fractional bandwidth begins to increase, because the slope around the resonant frequency decreases. When $l \approx (\lambda_c/2)$, the cable becomes a dipole with strong radiation at the operating frequency, it will strongly affect the desired radiation mode of the proposed small antenna. So, the proposed circular antenna can keep its performance for compact devices without a feeding cable, e.g. directly connecting to a small sensor whose system performance will be tested and demonstrated in Chapter 6.

Finally, to evaluate performance of the proposed circular antenna, its bandwidth-efficiency product versus electrical size is compared with various antennas as illustrated in Fig. 3.15. The ideal dipole antenna has the same electrical size and resonant frequency as the proposed one. The experimental limit of bandwidth-efficiency product for planar antennas is obtained from products of the best planar antennas in [2]. The performance data contains the bandwidth-efficiency product of each antenna $(B\eta)_a$, the theoretical

bandwidth-efficiency product limit $(B\eta)_L$, the experimental bandwidth-efficiency product limits $(B\eta)_E$, and the ratio of the bandwidth-efficiency product of each antenna to the theoretical limit with the same electrical size $(B\eta)_a/(B\eta)_L$. In Fig. 3.15, solid and hollow symbols with the same electrical size represent $(B\eta)_a$ and $(B\eta)_a/(B\eta)_L$ of the same antenna. It is observed that all $(B\eta)_a$ are below the curve of $(B\eta)_L$, and the change trend of gap between $(B\eta)_L$ and $(B\eta)_E$ indicates that the smaller the antenna is, the more difficult the design of a planar small antenna is.

3.6 Summary

A miniaturized circular UHF antenna is proposed in this chapter. CMA is used to analyze and design the antenna whose radiating body is transformed from a monopole. After comparing radiation behaviors and sizes of radiating bodies with different ground planes, the one with an improved ring ground plane is selected. CMA also points out that the size of radiator fabricated on a substrate is smaller than the one with only conductor, and the normalized resonant frequency for the radiator fabricated on substrate is a scale factor of the substrate height. Then, a feeding loop is designed to excite the radiator through magnetic coupling. Finally, an example of the proposed antenna is designed and fabricated to resonate at 474 MHz with a radius of 33 mm (0.052λ) and a height of 3.1 mm (0.005λ). CMA of the proposed antenna with a test cable having different lengths is applied to explain the difference between simulated and measured VSWRs.

Chapter 4

Design of an UWB U-shaped Printed Monopole Antenna

4.1 Introduction

As introduced in Chapter 2, operating frequencies of TVWSDs are dynamically obtained from geo-location database, spectrum sensing or their combination. Thence, antennas covering the entire TV spectrum are preferred for IoT devices operating over TVWS, and a compact and low-profile candidate is proposed in this chapter. Specifically, the related work on UHF TV antennas and the main contributions of this chapter are reviewed in Section 4.1. CMA on the radiating body and the proposed antenna are carried out in Section 4.2. Section 4.3 presents a parameter study, simulation and measurement results discussions. Finally, Section 4.4 concludes this chapter.

4.1.1 Related Work

Begun by some European countries around 2006, the digital television transition switches analog broadcast television to digital. From 2009, full-power television stations

nationwide have been required to broadcast exclusively in a digital format in the United States [87]. Since then, new types of digital television (DTV) receiving antennas have attracted significant interest from both the academia and the industry. These antennas are required to not only offer a wide operating bandwidth covering the whole digital video broadcasting —terrestrial (DVB-T) band (470-862 MHz), but also be compact enough to be integrated into mobile communication devices such as laptop, mobile phone, vehicles, etc. [5, 88–90]. Chi *et al.* [5] separated a rectangular plate by a step-shaped feed gap to create a dipole consisting of two asymmetric radiating portions. By exciting two resonant modes centered at 530 MHz and 730 MHz, they realized a DVB-T antenna with VSWR lower than 2.5 from 470 MHz to 806 MHz. Printed on a FR4 substrate, the proposed antenna had a volume of $227\text{ mm} \times 20\text{ mm} \times 0.4\text{ mm}$. Caso *et al.* [88] proposed a DVB-T antenna based on PIFA. Again, this antenna consisted of two radiating elements, and the driven one was the primary element governing the lowest resonant frequency. The upper resonant frequency was controlled by the other coplanar parasitic branch. This antenna covered 470-862 MHz with less than -6 dB return loss within a dimension of $217\text{ mm} \times 12\text{ mm} \times 8\text{ mm}$. To reduce the antenna size, Ma and Chu [89] folded a radiation patch to inverted-U shape and cut a notch on the patch to increase the equivalent electrical length. In addition, a folded parasitic arm surrounding the patch was introduced to broaden the bandwidth. On a $157\text{ mm} \times 70\text{ mm}$ system ground plane, the proposed antenna occupied a size of $70\text{ mm} \times 42\text{ mm}$, and its measured impedance bandwidth (3:1 VSWR) reached 360 MHz (460-820 MHz). Chen [90] meandered a printed monopole to create the first low-frequency resonance within a compact space. In addition, he extended two sleeves from the ground, which, on the one hand, lengthened the current path of the second resonant mode to lower the resonant frequency of the second mode; on the other hand, improved impedance matching over the entire operating frequency band by increasing effective electrical length of the ground. Finally, this antenna achieved -10 dB bandwidth from 459 MHz to 891 MHz and its size was $174\text{ mm} \times 48\text{ mm} \times 1.6\text{ mm}$. Nevertheless many antennas have been designed to cover the UHF TV spectrum, most of existing designs were mainly based on parameter opti-

mization, and further physical insights are expected to reveal how the UWB property is fulfilled. Fortunately, those CMA-based bandwidth study introduced in Section 2.4.4 inspire me to design and understand an UWB antenna for IoT devices working at TVWS with the help of CMA.

4.1.2 Contributions

In this chapter, a compact and low profile UHF UWB antenna is proposed with CMA, and the main contributions of this chapter are summarized as follows:

- A U-shaped patch is transformed from a rectangular plate following physical essence revealed by the CMA.
- Based on patch's modal characteristics, specific modes are selected to be excited for the UWB operation. Corresponding feeding location is also decided.
- Characteristics of significant modes are studied again after printing the radiating body onto a thin substrate. Characteristic angles, modal current distributions, and their contributions to the total radiation are discussed, which helps to understand the operating mechanism of an UWB printed monopole antenna from the point of TCM.
- Effects of significant parameters on the antenna performance are discussed, and the whole antenna geometry is optimized. An antenna prototype is fabricated and measured to verify its ultra-wide impedance bandwidth and monopole-like radiation patterns. Realized gain and radiation efficiency over the UHF TV spectrum are also measured.
- The bandwidth efficiency product against antenna electrical size is calculated and compared with the theoretical limit and classical antenna designs.

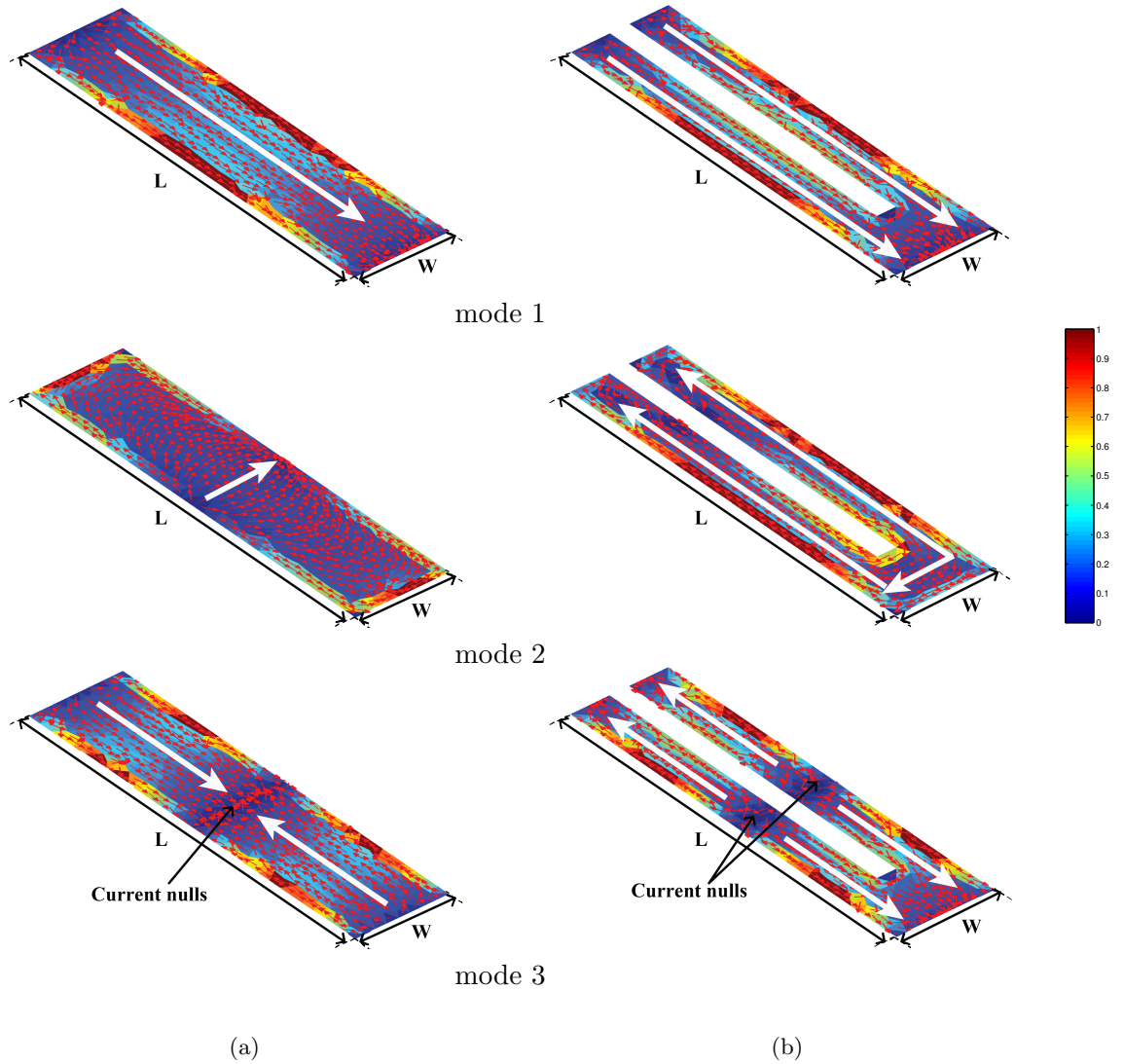


Figure 4.1: Normalized current distributions of the first three modes for (a) rectangular plate and (b) U-shaped plate in simulation.

4.2 Antenna Design

4.2.1 Radiating Body Design and Characteristic Mode Analysis

The metal rectangular plate has been commonly adopted as a radiating body in UWB antennas [91], [92]. Here, based on the TCM discussed in Section 2.4, characteristic modes of a metal rectangular plate having a length of L and a width of W are analyzed. Currents of its first three modes are illustrated in Fig. 4.1(a), and according to which,

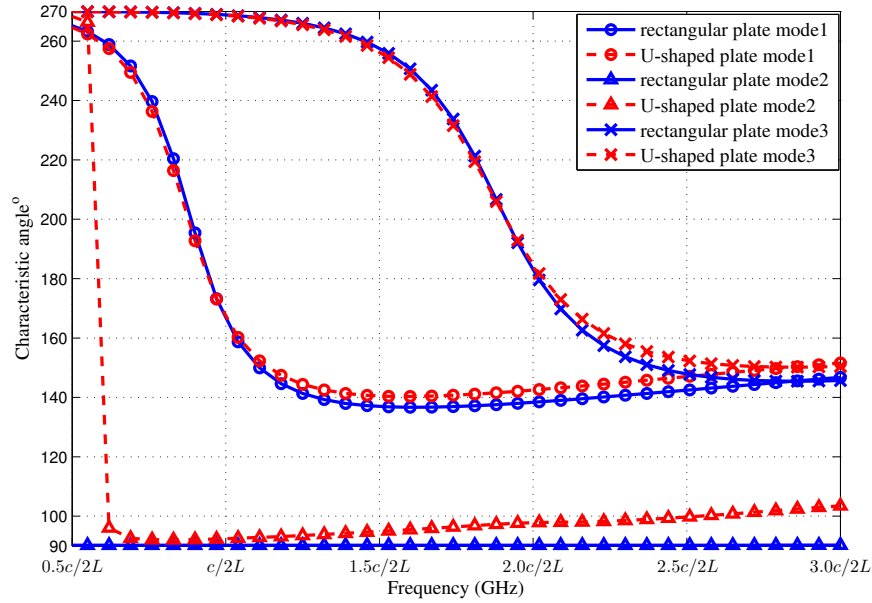


Figure 4.2: Simulated characteristic angles of the first three modes for rectangular (solid curves) and U-shaped (dashed curves) plates. Modes 1, 2, and 3 are noted by 'o', ' Δ ', and '+', respectively. L is the length of the plate and c is the speed of light.

mode 1 and mode 2 are characterized by currents flowing along the long axis and the short axis of the plate, respectively. Having the current along the long axis of the plate, mode 3 is a high order mode of mode 1 and has a current null. Characteristic angles of the rectangular plate are shown as solid curves in Fig. 4.2. It is seen that modes 1 and 3 resonate at around $c_0/2L$ and c_0/L , i.e. L is half wavelength and one wavelength of the resonant frequencies of modes 1 and 3. Characteristic angles of modes 1 and 3 pass through 180° smoothly, which indicates that they have the potential to contribute to wideband operations, and hence currents of these two modes in Fig. 4.1(a) are further explored.

It is noticed that the current strengths of both modes 1 and 3 are weak in the middle of the plate, and thus parts of the plate are removed and a U-shaped plate appears. Currents of the first three modes supported by the U-shaped plate are plotted in Fig. 4.1 (b), according to which, currents of modes 1 and 3 are along the long axis of the plate as the corresponding modal currents of the original plate. However, some new

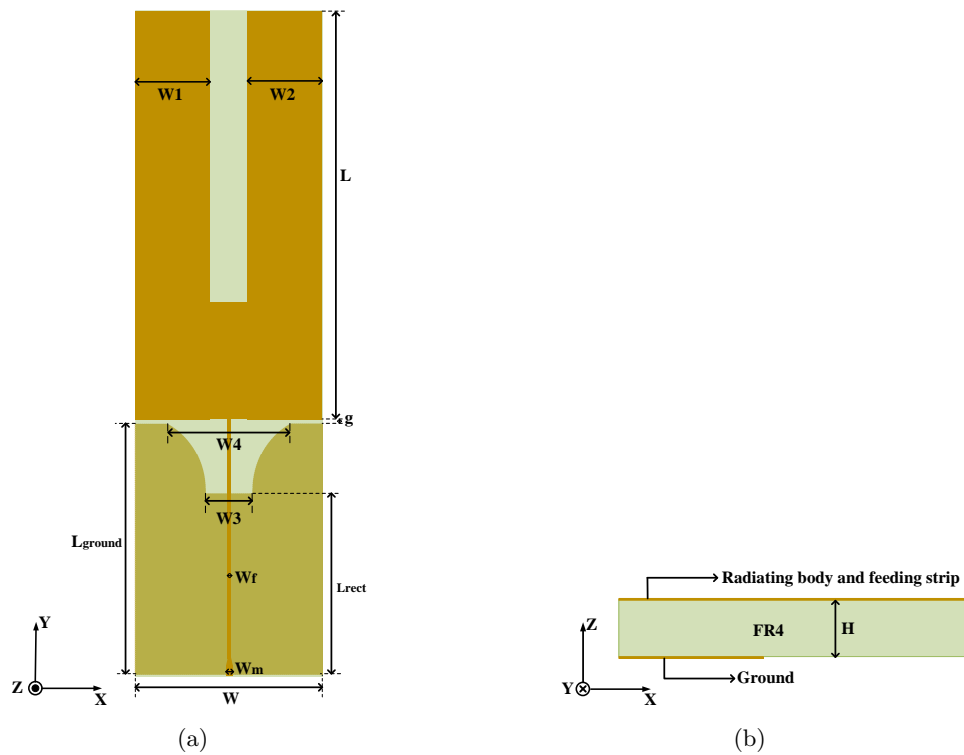


Figure 4.3: Geometry of the proposed antenna (a) top view and (b) side view.

modes come up after cutting the slot, and for instance, the second mode illustrated in Fig. 4.1 (b). Modal characteristic angles of the U-shaped plate are given in Fig. 4.2 as dashed curves together with those of the original plate. Mode 2 of the U-shaped plate passes through 180° exceedingly sharply, and hence it is impossible to contribute to the wideband performance. Therefore, modes to be utilized to realize UWB property are those having currents along the long axis of the plate. Comparing characteristic angles of the rectangular and the U-shaped plates, it can be found from Fig. 4.2 that resonant frequencies of modes 1 and 3 keep invariant, but characteristic angles of the U-shaped plate have slightly flatter gradients near their resonances, which is helpful to achieve wider bandwidth.

4.2.2 Characteristic Mode Analysis on the Proposed Antenna

The U-shaped $L \times W$ plate is then printed on a 0.8 mm-thick FR4 PCB board backed by a ground plane for easier fabrication. According to analyses conducted in [69], the presence of the ground and the substrate would not significantly alter modal current distributions on the radiating plate, although they would affect modal resonances. To excite modes capable of radiating efficiently over a wide range of frequencies like mode 1 and mode 3 discussed in Section 4.2.1, and other high order modes having currents along the long axis of the plate, a microstrip line is adopted to feed the radiating body from the bottom of its long axis as Fig. 4.3 shows. The feeding is applied at the center to preserve the symmetry of the structure and avoid unexpected modes, having current components along the short axis of the radiating body, being excited. Based on [93], cutting a notch on the ground can improve impedance matching of printed monopole antennas. For this antenna, instead of inserting a notch to improve the matching, the edges of the notch are optimized to arcs to extend the electrical length of the ground. Afterwards, characteristic modes of the whole structure are analyzed with a 50 Ω -impedance excitation being taking into account.

After applying an excitation voltage on the structure, modal reflection coefficients can be obtained following deductions given in Section 2.4.3 and modal VSWRs ($VSWR_n$) can then be acquired from

$$VSWR_n = \frac{1 + |\Gamma_n|}{1 - |\Gamma_n|} = \frac{1 + \left| \frac{1}{Y_{in}^n} - Z_0 \right|}{1 - \left| \frac{1}{Y_{in}^n} + Z_0 \right|} \quad (4.1)$$

When the long axis of the radiating body is 145 mm, the total VSWR combined by all modes is less than 2 from 500 MHz, and hence $L = 145 \text{ mm}$ is used for the following simulations to discuss performance of the antenna over the UHF TV spectrum. Modes become complex after having ground, feeding strip and substrate, and five significant modes are depicted in Fig. 4.4. For the first mode shown in Fig. 4.4(a), currents on

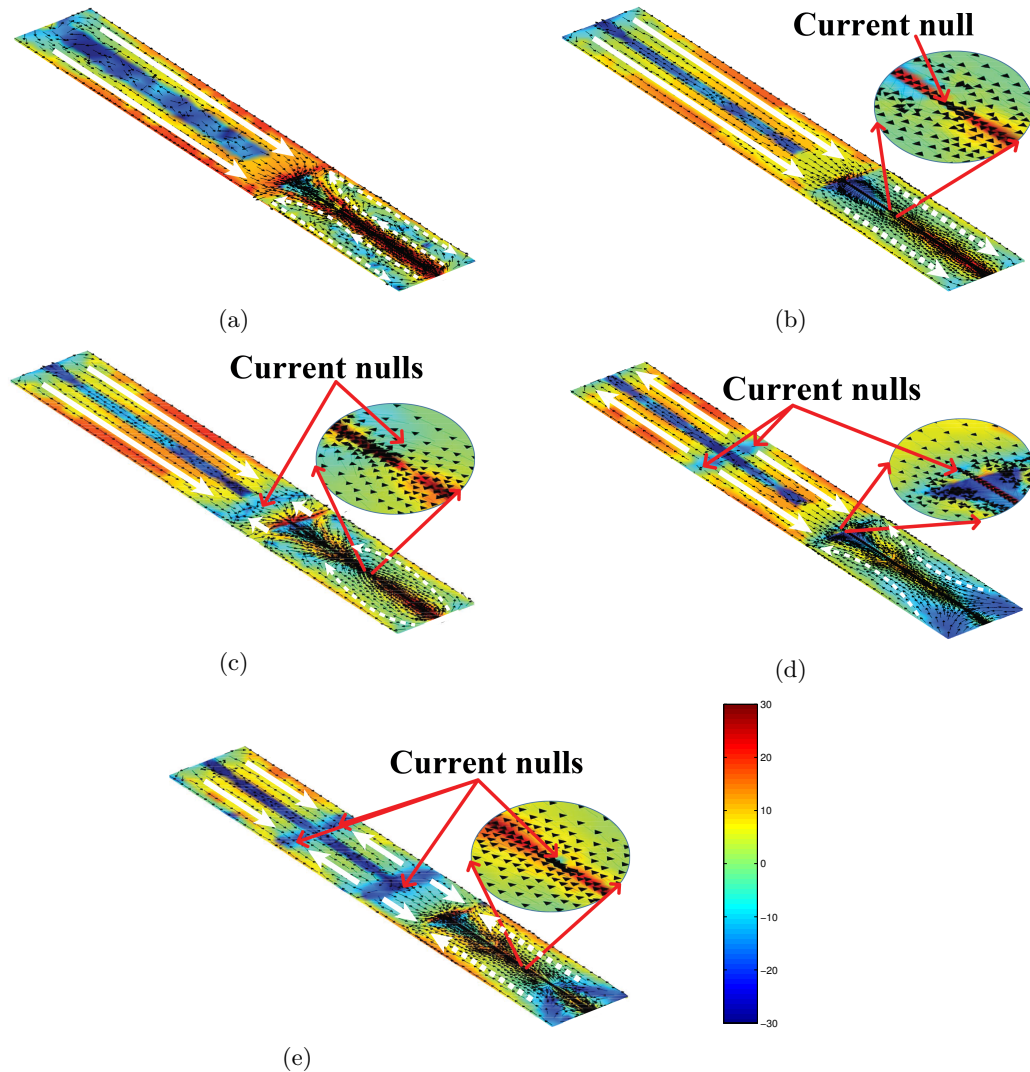


Figure 4.4: Simulated modal current distributions of (a) mode 1 at 370 MHz, (b) mode 2 at 700 MHz, (c) mode 3 at 1080 MHz, (d) mode 4 at 1010 MHz, and (e) mode 5 at 1300 MHz on the proposed antenna (current indicators on the U-shaped radiator are noted by solid lines, while those on the ground are noted by dashed curves).

the radiating body and the feeding strip have the same direction, while in Fig. 4.4(b) a current null appears on the feeding strip in the second mode. The third mode has a null at the bottom of the radiating body and another on the feeding strip as Fig. 4.4(c) shows. For the fourth mode illustrated in Fig. 4.4(d), there are nulls at the middle of the radiating body and around the junction of the feeding strip and the radiating body. In Fig. 4.4(e), two nulls emerge on the radiating body in the fifth mode and its feeding

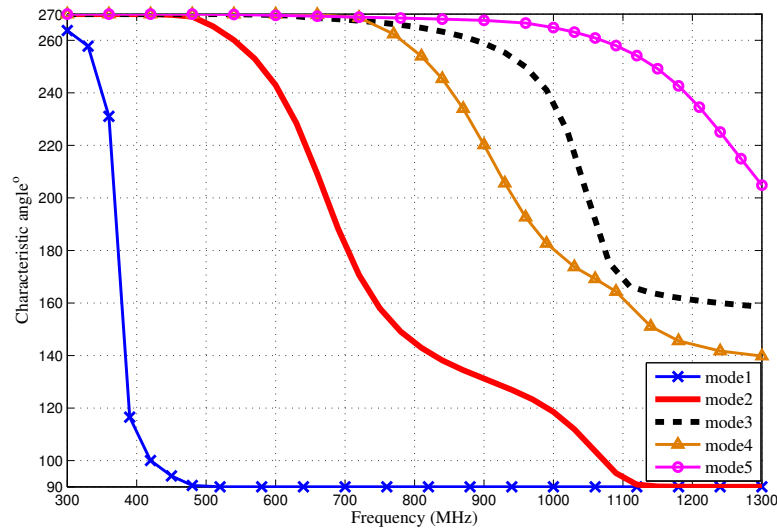


Figure 4.5: Simulated characteristic angles of modes 1-5 on the proposed antenna.

strip also sees one current null. On the radiating body, all the five significant modes have currents along its long axis as expected.

The proposed antenna is simulated with 10 MHz frequency interval over 300-1300 MHz, and characteristic angles of the five significant modes are plotted at Fig. 4.5, in which some markers are removed to ensure they do not overlap with each other. According to Fig. 4.5, except for mode 1 whose characteristic angle passes through 180° steeply at 370 MHz, all other modes present wideband potential. It is also noticed that characteristic angles of mode 3 and mode 4 are very close to each other at around 1100 MHz, and they seem to be mixed up. Therefore, to avoid unreliable mode tracking due to similar current distributions, the proposed antenna is simulated again over a narrower frequency range (1050-1150 MHz) and with denser frequency interval (2 MHz). The recalculated characteristic angles of mode 3 and mode 4 from 1050 MHz to 1150 MHz are the same as those given in Fig. 4.5 within the same frequency range, and current distributions of each mode are checked manually to make sure the same current distribution exists at each frequency.

Subsequently, modal VSWRs of the five modes are plotted in Fig. 4.6 together with the total VSWR simulated by FEKO. Based on Fig. 4.6, antenna performance over

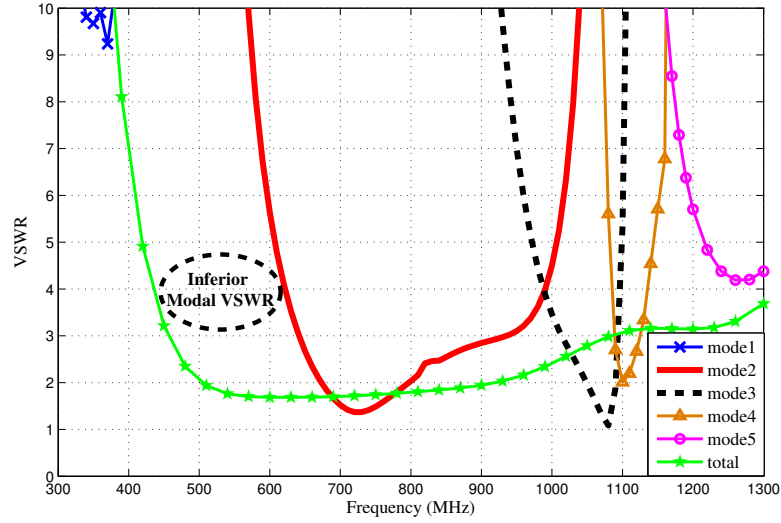


Figure 4.6: Simulated modal VSWRs of modes 1-5 and the total VSWR on the proposed antenna.

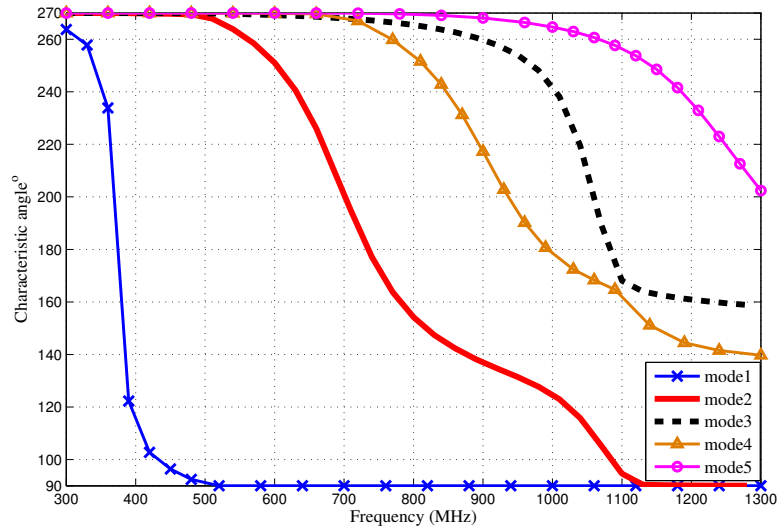


Figure 4.7: Simulated characteristic angles of modes 1-5 after reducing L_{rect} used in Fig. 4.5 by 8 mm.

600-1000 MHz is determined mainly by mode 2. Mode 3 and 4 are dominant within 1000-1150 MHz. And the highest resonance is contributed by mode 5. However, the VSWR between 450 MHz and 600 MHz is worth a discussion. Within this frequency range, modal VSWRs of all the five modes are inferior, but the total VSWR is less than 3. Observing modal currents ($\alpha_n J_n$) of all modes at frequencies within this region, it is found that the imaginary part of the modal current of the dominant mode, which is

mode 1 at frequencies lower than 485 MHz and mode 2 within 485-600 MHz, is far from 0, but multiple non-radiating modes (whose eigenvalues are far from 0) contribute to obtain an imaginary part of the cumulative current close to 0, and as a result, good total impedance matching and low overall VSWR are achieved.

The five significant modes are analyzed again with different sizes of the notch. Characteristic angles of modes 1-5 are plotted in Fig. 4.7 after reducing L_{rect} by 8 mm and keeping L_{ground} invariant. Comparing modal characteristic angles given in Fig. 4.5 and Fig. 4.7, it is noticed that characteristic angles of the second mode have a significant frequency shift, and its resonance moves from 700 MHz to 735 MHz. Observing the current distribution on the radiating body of this mode, it can be found that the distribution is the same as that of mode 1 labeled in Fig. 4.1(b) whose resonance is $c_0/2L$, which is 1034 MHz when L is 145 mm, according to the discussion in the Section 4.2.1. Hence, the presence of the ground and the substrate affect modal resonances, and the resonances are also affected by size of the notch.

4.3 Parametric Study and Measurement

4.3.1 Parametric Study

After understanding the operating mechanisms of the proposed structure, all parameters are optimized through simulation in the CST Microwave Studio. The width of the feeding strip is set to $W_m = 1.6$ mm at the bottom of the antenna to match with the 50Ω SMA connector, and it tapers to 1.1 mm ($W_f = 1.1$ mm) to match with the impedance of the radiating body. Significant parameters are discussed in this part to obtain the optimal

Table 4-A: Dimensions of the proposed antenna.

Parameter	L	W	H	L_{rect}	L_{ground}	g
Value (mm)	145	35	0.8	58	85	1
Parameter	W1	W2	W3	W4	Wm	Wf
Value (mm)	14	14	6	19.4	1.6	1.1

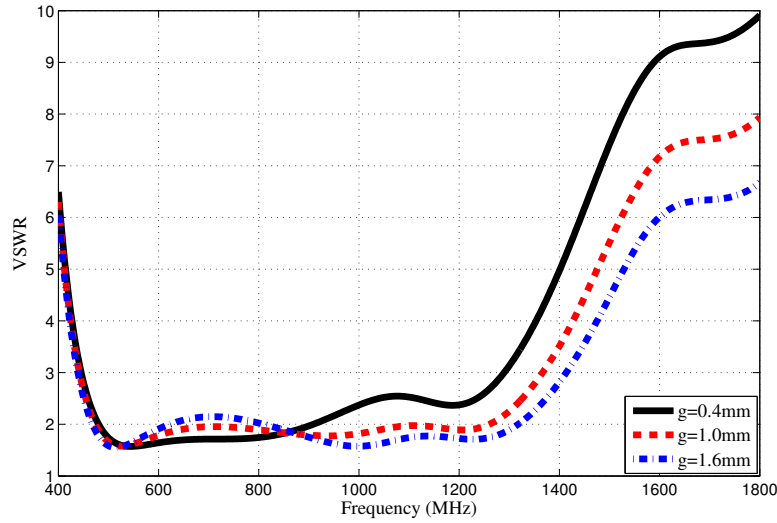


Figure 4.8: Simulated VSWRs for different widths of the slit between the radiating body and the ground.

antenna performance.

1) Slit between the radiating body and the ground

According to current distributions shown in Fig. 4.4, currents of all dominant modes are concentrated near the slit (noted by g in Fig. 4.3) between the radiating body and the ground. The effect of adjusting width of the slit is indicated in Fig. 4.8. When increasing g , the $VSWR < 2$ impedance bandwidth starts from slightly lower frequency, but VSWRs at high frequencies of the UHF TV spectrum deteriorate. Consequently, the antenna exhibits multiband instead of UWB property as expected. However, an excessive narrow slit results in shrinking of the antenna bandwidth and unsatisfying performance at low frequency band of the UHF TV spectrum. After extensive simulation, a 1 mm-wide slit is chosen to enable the antenna to cover all channels of the UHF TV spectrum and to realize the widest bandwidth.

2) Size of the notch

Based on analyses in Section 4.2.2, the notch on the ground affects resonances of modes exhibiting wideband potential, and hence it plays a crucial role for the proposed antenna to achieve UWB performance. The ground can be regarded as a combina-

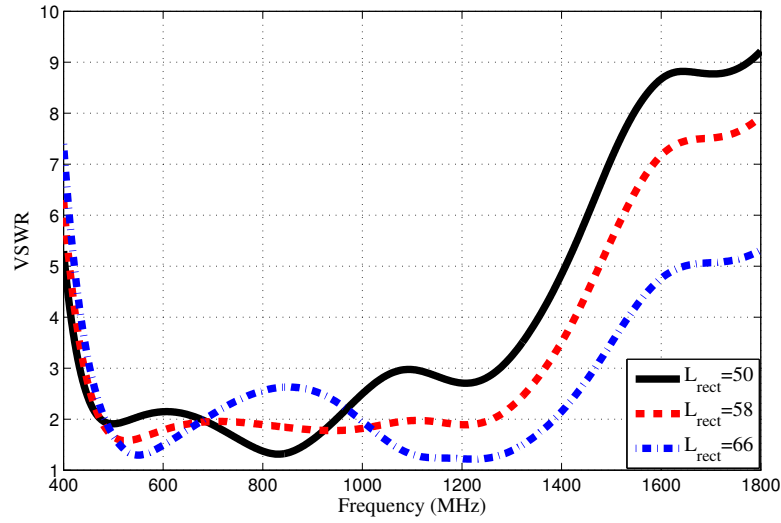


Figure 4.9: Simulated VSWRs for different dimensions of the notch on the ground.

tion of a rectangular having length L_{rect} and two truncated 1/4 ellipses. Keeping total length L_{ground} of the ground constant, portions of the rectangle and truncated 1/4 ellipses decide depth and width of the notch and, as a result, affect impedance matching. As Fig. 4.9 illustrates, increasing L_{rect} , which makes the rectangle part take higher proportion, leads to better matched impedances at low frequencies of the UHF TV spectrum, and hence lower VSWRs. But VSWRs become worse at high frequency bands of the UHF TV spectrum due to poorer matching. Increasing the proportion of the truncated 1/4 ellipses by decreasing L_{rect} causes opposite results to appear. Ultimately, a trade-off is made to set L_{rect} as 58 mm, and the widths of upper and lower edges of the notch W_4 and W_3 are 19.4 mm and 6 mm, respectively.

4.3.2 Antenna Measurement

With the optimized parameters indicated in Table 4-A, a prototype is fabricated and measured in QMUL. Photos of the antenna prototype are shown in Fig. 4.10. The simulated and measured VSWRs are depicted in Fig. 4.11. As shown in the figure, the simulated $VSWR < 2$ impedance bandwidth is from 474 MHz to 1260 MHz, and it is from 474 MHz to 1212 MHz in measurement. Measured VSWRs agree well with those

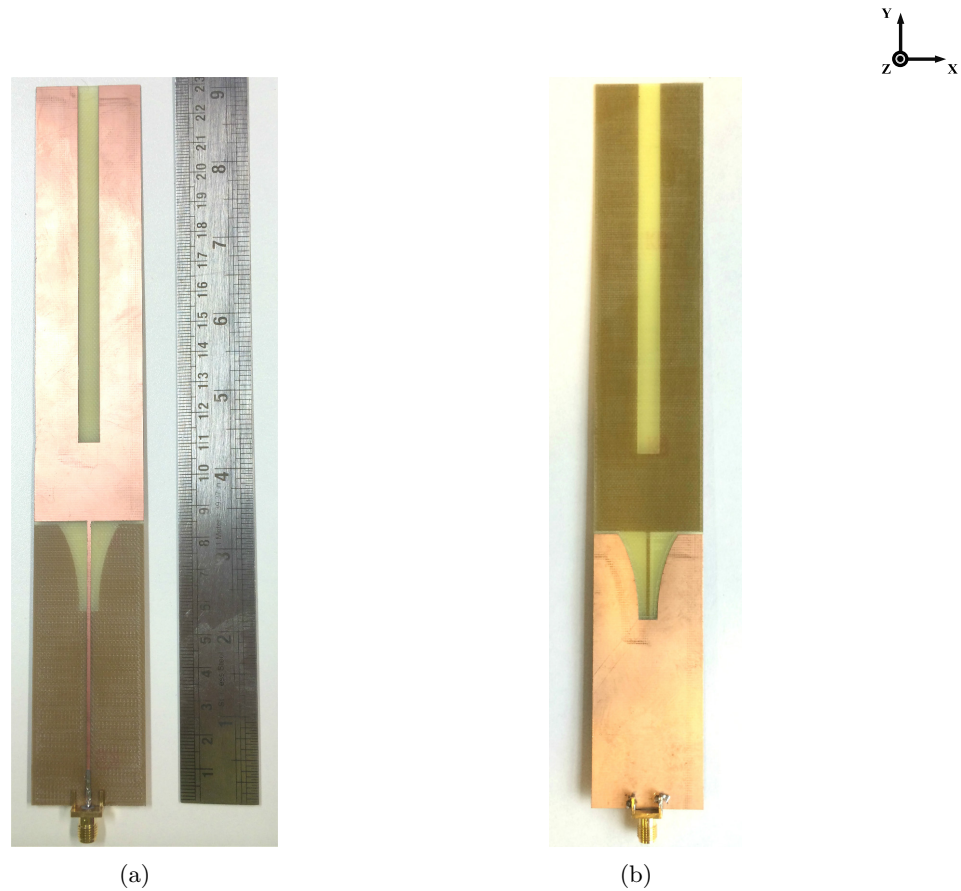


Figure 4.10: Prototype of the proposed antenna (a) top view and (b) back view.

in simulation, and differences could be introduced from the cable loss and fabrication imperfections. Table 4-B compares the impedance bandwidth and the size of the proposed antenna with those of other antenna designs operating over the UHF TV spectrum. And according to the table, the proposed antenna exhibits strong competitiveness on the compactness and the bandwidth.

To observe radiation patterns of the proposed antenna over the UHF TV spectrum, radiation patterns at three significant frequencies 474 MHz, 630 MHz, and 786 MHz, which are central frequencies of the first, the middle, and the last channels of the UHF TV spectrum, were simulated in the CST Microwave Studio and measured inside an anechoic chamber. Radiation patterns of the proposed antenna on both electric field and magnetic field planes at these frequencies are shown in Fig. 4.12. It is noticed that radiation

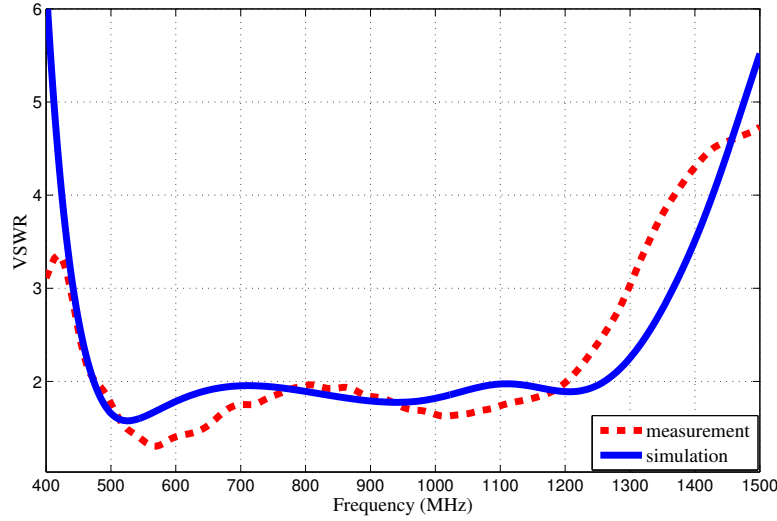


Figure 4.11: Simulated and measured VSWRs of the proposed antenna.

patterns on the H-plane correspond well to those obtained in simulation, and they are omnidirectional at all these frequencies. Two radiation nulls appear on the E-plane like patterns of a traditional monopole. Small discrepancies between measurement and simulation results could be caused by the effects introduced by cables and unavoidable scatterings in the chamber.

Realized gain and radiation efficiency of the proposed antenna over the UHF TV spectrum are then measured to evaluate its performance at the maximum radiation direction and all areas surrounding it, respectively [96].

The gain-transfer method is used during measurement in the anechoic chamber to

Table 4-B: Bandwidths and sizes of antennas covering the UHF TV spectrum (λ_L is the wavelength of the lowest operating frequency).

Antenna	VSWR	BW (MHz)	BW (%)	Size (mm^3)	Electrical size
[5]	2.5 : 1	470 – 810	53.1%	$227 \times 22 \times 0.4$	$0.36\lambda_L \times 0.03\lambda_L \times 0.001\lambda_L$
[88]	3.0 : 1	470 – 862	58.9%	$217 \times 12 \times 8.0$	$0.34\lambda_L \times 0.02\lambda_L \times 0.010\lambda_L$
[90]	1.9 : 1	459 – 891	64.0%	$174 \times 48 \times 1.6$	$0.27\lambda_L \times 0.07\lambda_L \times 0.002\lambda_L$
[94]	2.0 : 1	458 – 960	76.6%	$242 \times 35 \times 0.8$	$0.37\lambda_L \times 0.05\lambda_L \times 0.001\lambda_L$
[95]	2.5 : 1	463 – 871	61.2%	$241 \times 26 \times 0.8$	$0.37\lambda_L \times 0.04\lambda_L \times 0.001\lambda_L$
Proposed	2.0 : 1	474 – 1212	87.5%	$231 \times 35 \times 0.8$	$0.36\lambda_0 \times 0.06\lambda_L \times 0.001\lambda_L$

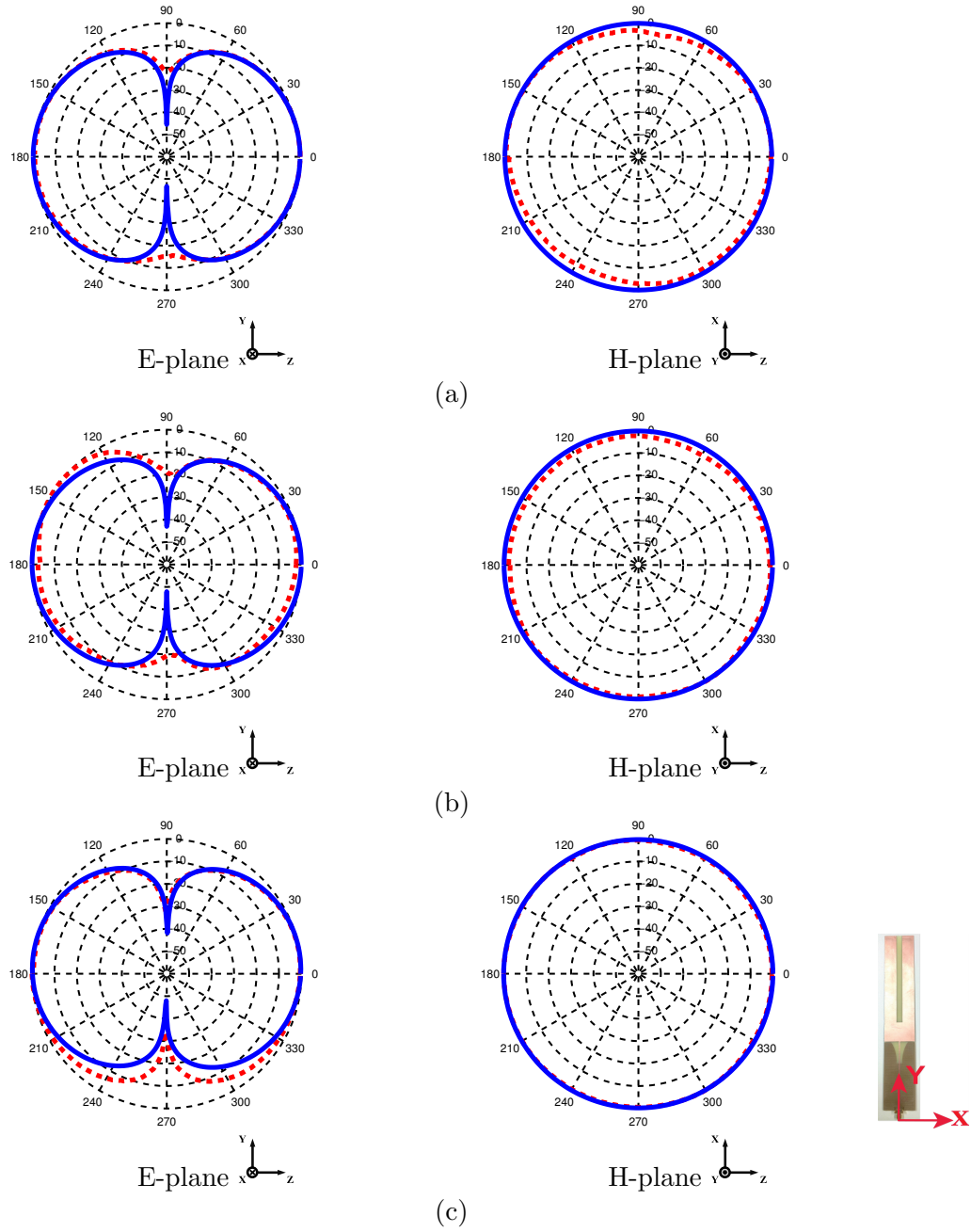


Figure 4.12: Simulated (solid curves) and measured (dashed curves) E-plane and H-plane radiation patterns at (a) 474MHz, (b) 630MHz, and (c) 786MHz.

measure the gain of the proposed antenna [97].

$$(G_T)_{dB} = (G_S)_{dB} + 20 \log_{10} \left(\frac{E_T}{E_S} \right) \quad (4.2)$$

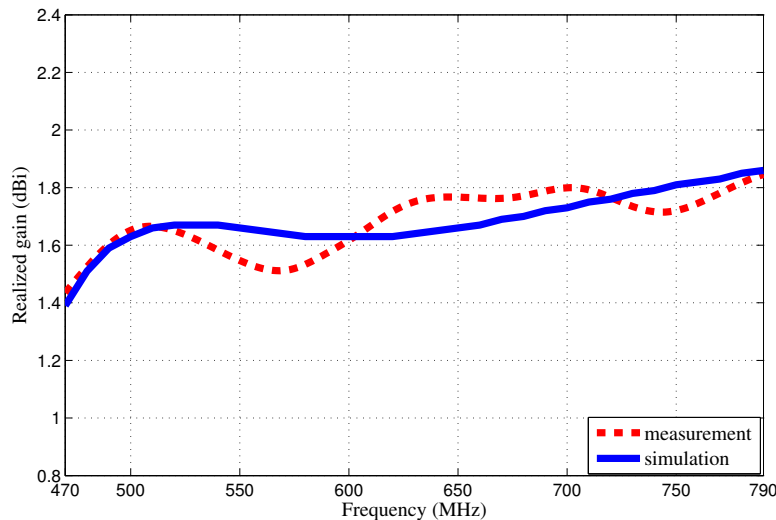


Figure 4.13: Simulated and measured realized gains over the UHF TV spectrum.

where $(G_T)_{dB}$ and $(G_S)_{dB}$ are gains (in dB) of the antenna under test and the standard gain antenna. E_T and E_S are electric field intensities of the two antennas measured in an anechoic chamber. A discone antenna is used as the standard gain antenna and its gain has been measured in the National Physical Laboratory in U.K. After measuring electric field intensities of both the antenna under test and the discone antenna, the gain of the proposed antenna over the UHF TV spectrum is calculated and plotted in Fig. 4.13. Its simulated gain is given in the same figure for comparison. Ranging from 1.4 dBi to 1.9 dBi, the measured gain reaches 1.7 dBi in average over 470-790 MHz, and it is close to the simulated result. The difference could be caused by cables and unavoidable scattering in the chamber, and the imprecise levels of height among the reference discone antenna, the proposed antenna, and the transmitting horn antenna may also introduce discrepancies.

Traditional radiation efficiency measurement methods include pattern integration method, Wheeler Cap method, directivity/gain method, etc. However, these methods are limited by high uncertainties or narrowband appliance [98, 99]. Reverberation chambers, basically shielded rooms, use a metallic rotating paddle to create a continuously changing boundary condition of the electromagnetic fields in the chambers. Offering a



Figure 4.14: Set up of the antenna radiation efficiency measurement using two-antenna method in a reverberation chamber.

statistical environment, the reverberation chamber is becoming popular as an alternative test facility for both electromagnetic and electromagnetic compatibility measurements [100]. In recent years, different methods have been explored to measure radiation efficiencies of antennas in reverberation chambers, e.g. the reference antenna method, the one-antenna method, and the two-antenna method. The antenna efficiency measurement in the reverberation chamber has its own advantages compared with other methods: it is robust (no need for high precision mechanical system), broadband, and with no need for a reference antenna [101].

In this work, the proposed antenna is measured in a reverberation chamber at the University of Liverpool based on the two-antenna method [102], [103]. As Fig. 4.14 demonstrated, duplicate antennas under test are placed in the reverberation chamber at the same time, and the radiation efficiency can be calculated from:

$$\eta = \frac{\langle |S_{21,s}|^2 \rangle}{1 - \langle |S_{11}|^2 \rangle} \sqrt{\frac{2C_{RC}}{\omega\tau_{RC} \langle |S_{22,s}|^2 \rangle}} \quad (4.3)$$

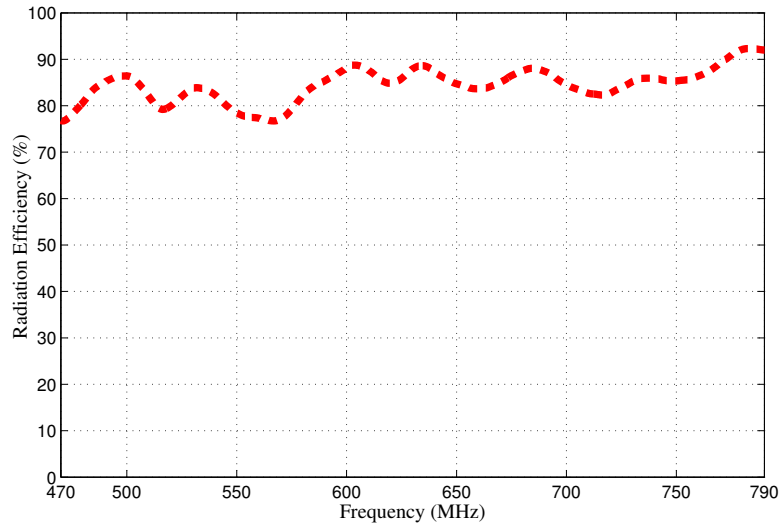


Figure 4.15: Measured radiation efficiency of the proposed antenna over the UHF TV spectrum.

where S_{11} and S_{22} are reflection coefficients of the the two antennas under test respectively and S_{21} is the transmission coefficient between them. $\langle \cdot \rangle$ means the average value of the S-parameters. $S_{*,s}$ is the stirred part of the S-parameters and it can be obtained by the well-known vector average subtraction $S_{*,s} = S_* - \langle S_* \rangle$ [104]. τ_{RC} is the chamber decay time and $C_{RC} = 16\pi^2 V / \lambda^3$ is the chamber constant, in which V is the volume of the reverberation chamber.

Measured radiation efficiency over the UHF TV band is shown in Fig. 4.15, and according to which, the radiation efficiency is between 76.2% and 92.4% across 470-790 MHz. Thus, most power delivered to the antenna is capable of being radiated. Based on measurements and discussions above, both gain and radiation efficiency of the proposed antenna are almost uniform over the UHF TV spectrum, and these measurement results indicate that the proposed antenna could be a competitive antenna candidate for IoT devices operating over TVWS.

4.3.3 Bandwidth-Efficiency Product against Antenna Electrical Size

As discussed in Section 2.2, the maximum bandwidth of an antenna is constrained by its electrical length. Therefore, to appraise the overall performance of the proposed antenna, its product of bandwidth and efficiency is compared with the theoretical limit and products of other classic designs.

For the proposed printed monopole antenna, its center operating frequency is 843 MHz and the minimum radius of the sphere enclosing the antenna is $a = 116.8 \text{ mm}$. The electrical size is $ka = 2.06$. With the measured fractional bandwidth (87.5%) and the average radiation efficiency (86.4%), its bandwidth-efficiency product is $87.5\% \times 86.4\% = 0.756$. The bandwidth-efficiency product against electrical size of the proposed antenna is plotted in Fig. 4.16 together with those of antennas given in [2] for comparison. Since the electrical size of the proposed antenna is 2.06, in Fig. 4.16, antennas having electrical size smaller than 0.5 and larger than 3 are omitted. According to Fig. 4.16, performance of the proposed antenna is very close to the theoretical limit, and its bandwidth-efficiency product has exceeded most designs having similar electrical size. This discussion proves that full radiation potential on the compact printed monopole antenna has been explored by the CMA.

4.4 Summary

A novel compact antenna designed for IoT devices is proposed in this chapter. The CMA is employed to analyze modal characteristics of a rectangular plate and to guide the slot cutting in the middle of the plate. After applying a microstrip feed and optimizing the ground, the proposed antenna realizes 87.5% $VSWR < 2$ impedance bandwidth from 474 MHz to 1212 MHz within a dimension of $0.36\lambda_0 \times 0.06\lambda_0 \times 0.001\lambda_0$ (λ_0 is wavelength of the minimum operating frequency 474 MHz). The CMA is further utilized to reveal that the UWB behavior is achieved by exciting multiple modes able to radiate efficiently

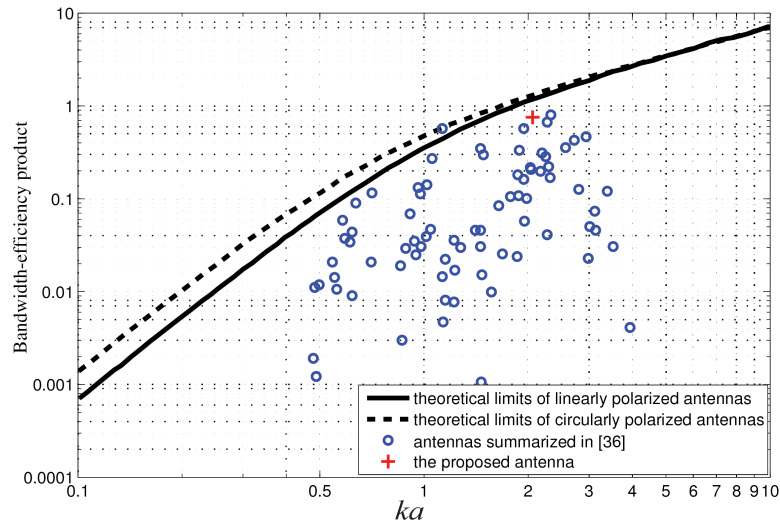


Figure 4.16: The measured bandwidth-efficiency product for antenna designs summarized in [2] (noted by 'o') and the proposed antenna (noted by '+').

over different frequency bands. It has been observed that the radiation pattern of the antenna is omnidirectional over the UHF TV spectrum, and 1.7 dBi average gain and high radiation efficiency are achieved within its operating frequency band. Furthermore, the bandwidth-efficiency product reached by the proposed antenna is closer to the theoretical limits than most of previous antenna designs. Owing to its compactness, low profile, UWB property, high radiation efficiency and reasonable gain, the proposed antenna can be a strong contender for smart IoT devices operating at TVWS.

Chapter 5

Design of an UWB Dual Annular Ring Antenna

5.1 Introduction

In Chapter 4, a printed monopole antenna achieving the UWB property over UHF was proposed and studied. It has been revealed by CMA that multiple radiating modes contribute together to achieve the wide bandwidth. In this chapter, the TCM will be fully applied to realize a TVWS antenna for IoT communications. The related work on bandwidth enhancement with CMA and feeding structure design, as well as the main contributions of this chapter are reviewed in Section 5.1. Section 5.2 carries out CMA on an annular ring and proposes a feeding structure to excite the desired modes on the ring. Then, both the ring and the feeding structure are modified in Section 5.3 to create more radiating modes and excite them efficiently. The final antenna is optimized in Section 5.4 where simulation and measurement results are also presented and discussed. Finally, Section 5.5 concludes this chapter.

5.1.1 Related Work

Since the CMA can distinguish characteristic modes on a structure and determine their resonating frequencies, researchers have utilized multiple modes to broaden antenna bandwidth. Adam and Bernhard [79] proposed the "resonance-antiresonance conductance ratio" to estimate an antenna's multiresonant potential even when the conductance values are not centered around the desired system conductance. They then appraised a low order TM_{10} -like mode and a higher-order TM_{10} -like mode to broaden bandwidth of the original TM_{10} mode. Finally, the antenna's bandwidth was nearly doubled by combining resonances of the TM_{10} mode and the higher-order TM_{10} -like mode. Shih and Behdad [105] enhanced the bandwidth of a vehicular VHF antenna by utilizing the vehicle platform as the major part of the radiating structure. A meandered monopole antenna mounted on the rear operated as a capacitive coupling element to excite a desired set of characteristic modes of the platform. As well as determining the modes of interest, applying a suitable excitation is also important to enable the antenna designed through CMA. Martens *et. al* [106] categorized the coupling elements used for the selective excitation of specific characteristic modes into the inductive coupling element (ICE) and the capacitive coupling element (CCE). They demonstrated the ICE placed at the current maxima and the CCE placed at the current minima could excite a specific current independently. They also concluded that ICE offered advantages over CCE in terms of mode purity. After analyzing characteristic modes of a folded radiating ground plane, Fabr es [107] utilized a small planar monopole to excite the structure. Follow-up analyses demonstrated that this feeding monopole behaved as a wideband impedance transformer between the feeding port and the upper plate, providing better performance than the classical coaxial probe that created a distributed voltage difference between the lower and upper plates.

5.1.2 Contributions

Motivated by the previous work, this chapter proposes a multi-mode UWB antenna design procedure guided by the CMA. The main contributions of this chapter are summarized as follows:

- Annular ring is one of the common antenna structures. With eigenvalues given by CMA, this chapter demonstrates that its resonant frequency obtained from the traditional estimation is not accurate enough. Therefore, a closed-form estimation is given to clarify the relationship between dimensions of an annular ring and resonant frequencies of the basic modes (mode 1 and mode 2) and to provide a general design reference for annular ring-shaped antennas.
- The fitted polynomial is firstly used to determine size of the original annular ring. Afterwards, to create new modes resonating at higher frequencies, the polynomial is used again on a smaller ring inserted into the original one.
- Slots are cut on the annular ring to reduce modal resonant frequencies. Decisions about positions to cut slots and the effects to different modes are analyzed with the help of CMA.
- Rectangular metal strips are used as the feeding structure. These strips operate as dipoles and the electromagnetic energy is coupled to the annular rings to produce induced currents. To excite all the modes of interest to cover the whole UHF TV spectrum, the feeding structure is carefully designed and refined.
- A prototype of the proposed antenna is fabricated and measured to verify its UWB performance. Radiation patterns at different frequencies are presented to prove the change of dominant resonating modes.
- Furthermore, antennas connect with other circuits or sources through coaxial connectors, which are directly connected to the balanced strips on the proposed

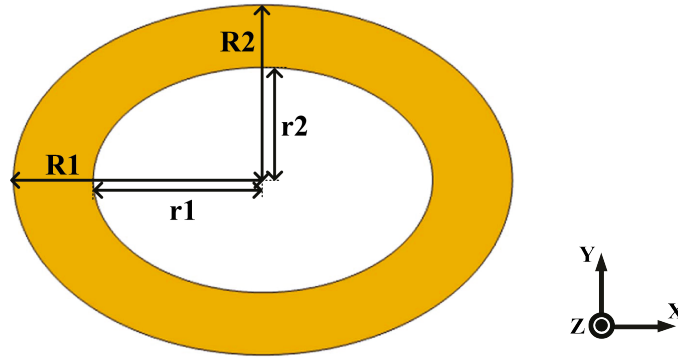


Figure 5.1: Geometry of an annular ring ($R_1=100$ mm, $R_2=70$ mm, $r_1=68$ mm, and $r_2=45$ mm).

antenna. Without a balun structure, leaky current on the outer surface of the unbalanced coaxial cable may also radiate, and as a result, distort the antenna radiation pattern. Thence, this chapter finally discusses effects of the coaxial cable to the antenna performance when it is used for IoT devices.

5.2 Characteristic Mode Analysis on an Annular Ring and Feeding Structure Design

5.2.1 Characteristic Mode Analysis on an Annular Ring

Before getting into details of the proposed antenna, I first perform the CMA on a metal annular ring which is selected as the basic structure of the UWB antenna owing to multiple modal resonant frequencies contributed by its axes with different lengths. For a ring depicted in Fig. 5.1, modal current distributions and radiation patterns of its first three modes are presented in Fig. 5.2. In this thesis, modal current distributions and radiation patterns are given at resonant frequencies of the corresponding modes, which, according to Fig. 5.3, are 708 MHz for mode 1 and 794 MHz for mode 2. As shown in Figs. 5.2(a) and (b), the currents of mode 1 and mode 2 flow along the long and the short axes of the ring, respectively, and corresponding to their orthogonal current distributions, mode 1 has a donut-like radiation pattern with nulls at the x-axis, while

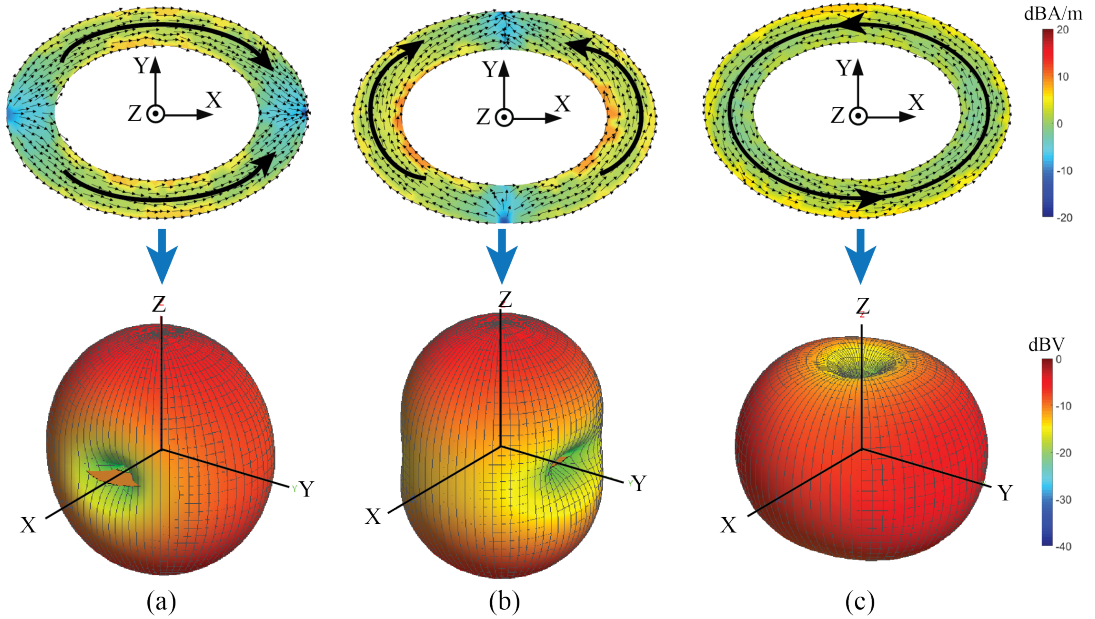


Figure 5.2: Modal current distributions and radiation patterns of (a) mode 1 at 708 MHz, (b) mode 2 at 794 MHz, and (c) mode 3 at 950 MHz on the annular ring shown in Fig. 5.1.

nulls of the radiation pattern turn 90° to the y -axis for mode 2. The current of mode 3 flows as a closed loop, and thus it behaves inductively, which can also be verified from Fig. 5.3 where its characteristic angles are all below 180° over the entire simulated spectrum. Because mode 3 cannot resonate, its current distribution and radiation pattern at the centre frequency of the simulated band (i.e. 950 MHz) are given as illustrations, which also applies to Fig. 5.5(c) and Fig. 5.7(d).

As introduced above, mode 1 and mode 2 behave like half-wave resonators whose resonant frequencies are $c_0/4R$, where $2R$ is the effective electrical length. Using $R = R_1 = 100$ mm for mode 1 and $R = R_2 = 70$ mm for mode 2, the calculated resonant frequencies are 750 MHz and 1071 MHz for the two modes, while their resonant frequencies are 708 MHz and 794 MHz in CMA simulation. The significant difference between the estimated and simulated results is because the annular ring is elliptically shaped and the currents always concentrate near the edge, and thus the effective modal electrical lengths used for estimation are not accurate. Moreover, these lengths also vary with geometry

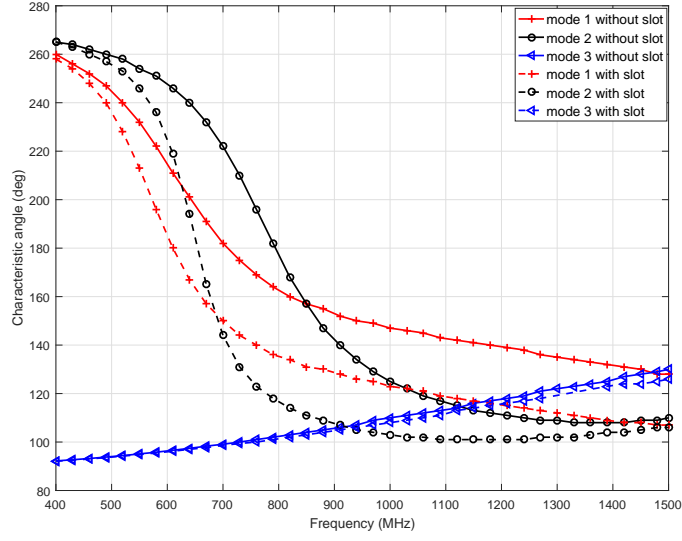


Figure 5.3: Characteristic angles of modes 1-3 for annular rings with and without slots.

parameters of annular rings. Therefore, to provide a general design reference for annular ring-shaped antennas, it is crucial to clarify the relationship between dimensions of the annular ring and resonant frequencies of the basic modes (mode 1 and mode 2). Fortunately, with the help of CMA, resonant frequencies of the two modes for structures with arbitrary dimensions can be found numerically.

For a given R_1 , another three parameters are introduced here: the axis ratio of the outer ellipse $k_0 = R_2/R_1$, the ratio of horizontal axes of the inner and the outer ellipse $k_1 = r_1/R_1$, and the ratio of their vertical axes $k_2 = r_2/R_2$ to determine dimensions of the annular ring structure. Then resonant frequencies (in MHz) of mode 1 and mode 2 can be approximated by a polynomial of k_1 and k_2 :

$$f(k_1, k_2) = p_{00} + p_{10}k_1 + p_{01}k_2 + p_{20}k_1^2 + p_{11}k_1k_2 + p_{02}k_2^2 \quad (5.1)$$

The polynomial coefficients deciding resonant frequencies of mode 1 and mode 2 for different k_0 when $R_1 = 100$ mm are presented in Table 5-A and Table 5-B. For different R_1 , the resonant frequencies can be obtained through the scaling relation. Since modal currents have strong intensities near the inner edge of the annular ring, as k_1 and k_2 decrease

Table 5-A: The polynomial coefficients of (5.1) calculating the resonant frequency (in MHz) of mode 1.

Parameter	$k_0 = 0.3$	$k_0 = 0.4$	$k_0 = 0.5$	$k_0 = 0.6$	$k_0 = 0.7$
p_{00}	818.3	806.9	894.8	924.2	1008
p_{10}	-244.6	-202.8	-322.6	-303.6	-385.5
p_{01}	103.3	134.7	50.48	-18.61	-139.2
p_{20}	186.7	178.7	235.9	236.9	295.5
p_{11}	13.89	-30.38	31.39	13.81	23.06
p_{02}	-217.2	-250.9	-271.6	-254.4	-225

Table 5-B: The polynomial coefficients of (5.1) calculating the resonant frequency (in MHz) of mode 2.

Parameter	$k_0 = 0.3$	$k_0 = 0.4$	$k_0 = 0.5$	$k_0 = 0.6$	$k_0 = 0.7$
p_{00}	2929	2646	2580	2244	2001
p_{10}	-4020	-3325	-3299	-2570	-2135
p_{01}	-184	-396.6	-555.8	-525	-521.2
p_{20}	1855	1429	1463	1015	782.8
p_{11}	4.11	83.59	176.6	158.1	182.3
p_{02}	192.6	311.7	368.7	339.1	322.5

dramatically, the effective electrical length also decreases, and thus the corresponding resonant frequency increases rapidly. To preserve the accuracy of the polynomial fitting, k_1 and k_2 in (5.1) are confined to be larger than 0.3.

Based on the fitted polynomial above, with geometry parameters given in Fig. 5.1 (i.e. $k_0 = 0.7$, $k_1 = 0.68$, and $k_2 = 0.64$), the estimated resonant frequencies are 710 MHz and 789 MHz for mode 1 and mode 2, which are quite close to the simulated results (708 MHz and 794 MHz).

5.2.2 Cutting Slots on the Annular Ring

As introduced in Chapter 2, cutting slots can increase the effective modal electrical lengths and reduce modal resonant frequencies. According to Fig. 5.4(b-1), for mode

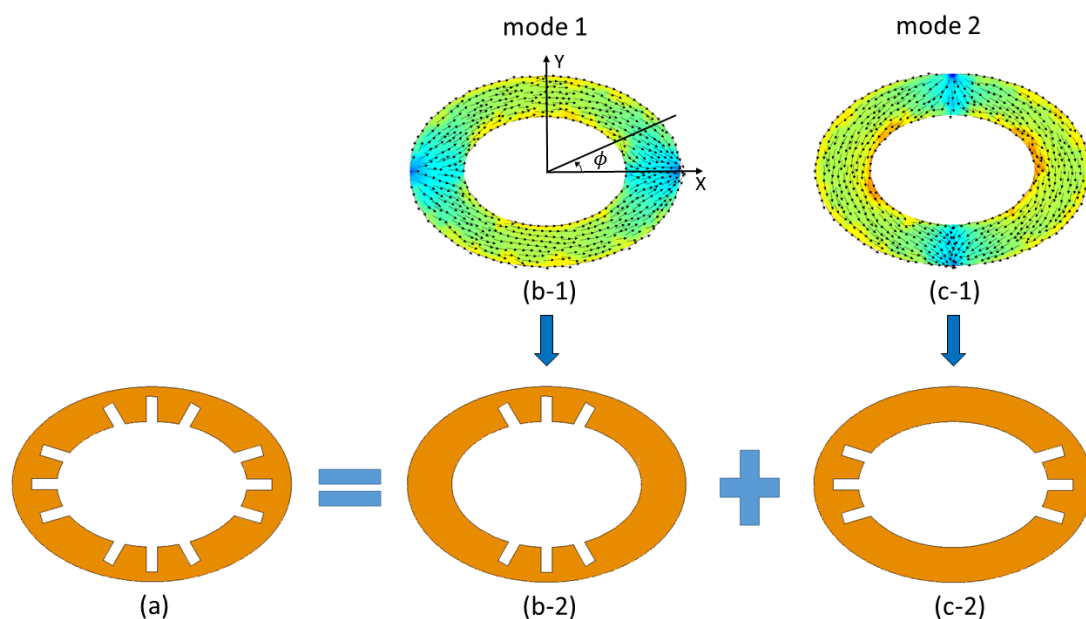


Figure 5.4: Current distributions of mode 1 and mode 2 on the original ring and illustrations of different slot cuttings.

1, nulls appear at $\phi = 0^\circ$ and 180° , and its current strength gets stronger when ϕ is closer to $\pm 90^\circ$. When slots are only cut at around $\phi = \pm 90^\circ$ on the ring as illustrated in Fig. 5.4(b-2), the resonant frequency of mode 1 is reduced to 614 MHz, while that of mode 2 has a very slight reduction to 781 MHz. This verifies that cutting slots at locations with strong currents can significantly reduce modal resonant frequencies, while slots at locations with weak current strengths barely affect the resonances. Similarly, the current strength of mode 2 is stronger when ϕ is closer to 0° and 180° , and when slots are cut as Fig. 5.4(c-2) depicted, the resonant frequency of mode 2 is reduced to 657 MHz, while that of mode 1 is 700 MHz. Resonant frequencies of mode 1 and mode 2 on the original ring and rings with different slots are summarized in Table 5-C. In addition, current strengths for both the two modes are stronger at the inner edge of the ring, and hence slots are cut at the inner edge to maximally increase effective modal electrical lengths.

For the number of slots, the work aims to use the minimum number of slots and keep symmetry of the ring (otherwise more modes will be generated which complicates

Table 5-C: Resonant frequencies of mode 1 and mode 2 on rings with different slot cuttings.

Structures	Without slot	With slots cut as Fig. 5.4(a)	With slots cut as Fig. 5.4(b-2)	With slots cut as Fig. 5.4(c-2)
mode 1	708 MHz	610 MHz	614 MHz	700 MHz
mode 2	794 MHz	654 MHz	781 MHz	657 MHz

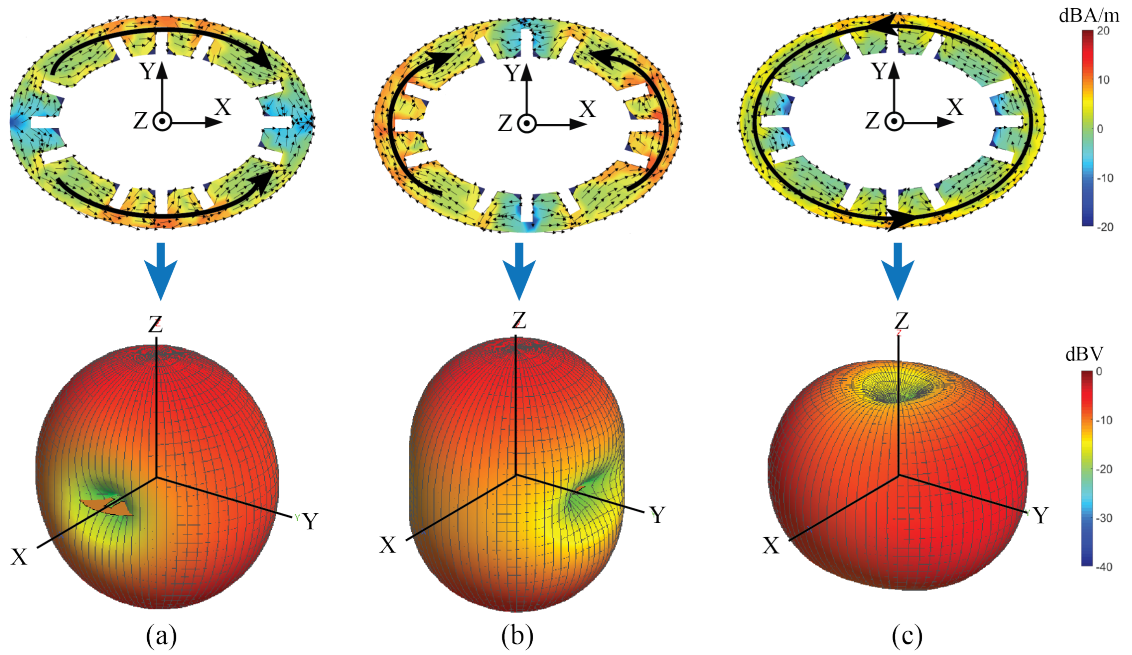


Figure 5.5: Modal current distributions and radiation patterns of (a) mode 1 at 610 MHz, (b) mode 2 at 654 MHz, and (c) mode 3 at 950 MHz on the annular ring with slots.

the analysis). After a thorough simulation study, it is found that with dimensions of the annular ring fixed, at least three slots at each area with strong modal currents are needed to reach the lowest band of the desired frequency. The structure with slots is illustrated in Fig. 5.5 where updated modal current distributions and radiation patterns of the slotted annular ring are also provided.

Characteristic angles of modes 1-3 are simulated again for the slotted annular ring, and results are plotted in Fig. 5.3 together with those of the ring without slots. It is noticed that the resonant frequencies of modes 1 and 2 have reduced to 610 MHz and 654 MHz, respectively. The characteristic angle curve of mode 3 remains unchanged since

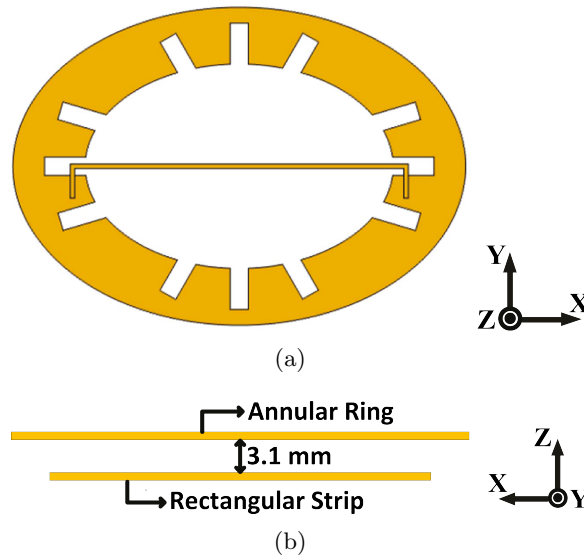


Figure 5.6: Structure layout of the slotted annular ring with a rectangular strip (a) top view and (b) side view.

the modal current flow is barely affected by the inserted slots, which can be seen from current distributions of Fig. 5.2(c) and Fig. 5.5(c). Moreover, according to radiation patterns given in Fig. 5.2 and Fig. 5.5, cutting slots on the ring has very slight effect on modal radiation patterns.

5.2.3 Characteristic Mode Analysis with Feeding Structure

A rectangular metal strip, serving as the feeding structure, along the long axis of the annular ring is then placed 3.1 mm below the ring as shown in Fig. 5.6. Normally, new characteristic modes would be introduced after adding new components to the existing structure. Thus, CMA is performed on the new whole structure whose modal currents and radiation patterns are illustrated in Fig. 5.7.

For this new structure, modes having currents along the long axis of the ring, illustrated in Figs. 5.7(a) and (b), exhibit similar radiation behavior as that of mode 1 given in Fig. 5.2(a). Therefore, the two modes are named as mode 1^a and mode 1^b . The difference between these two modes is that currents on the rectangular strip and the annular

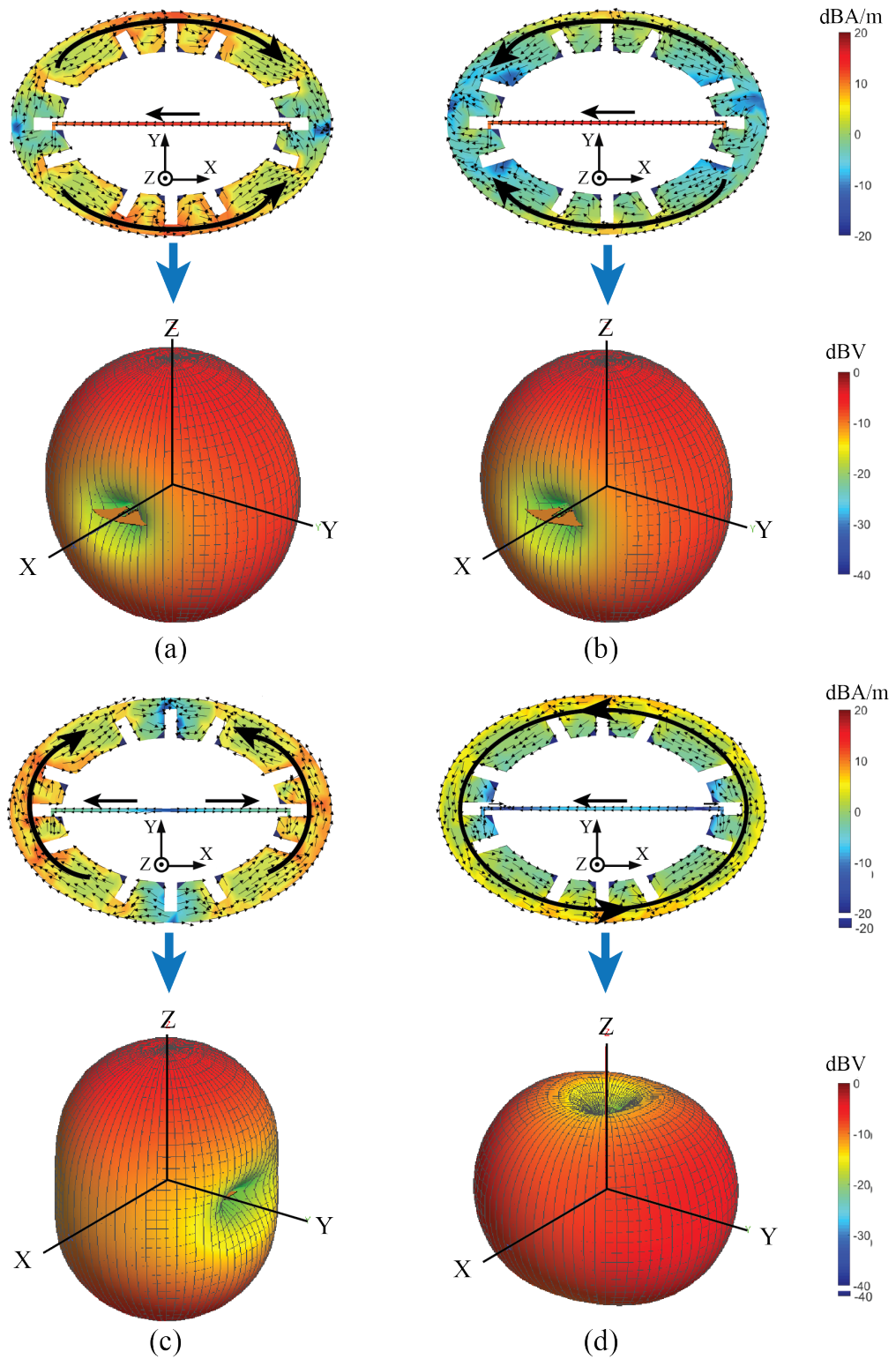
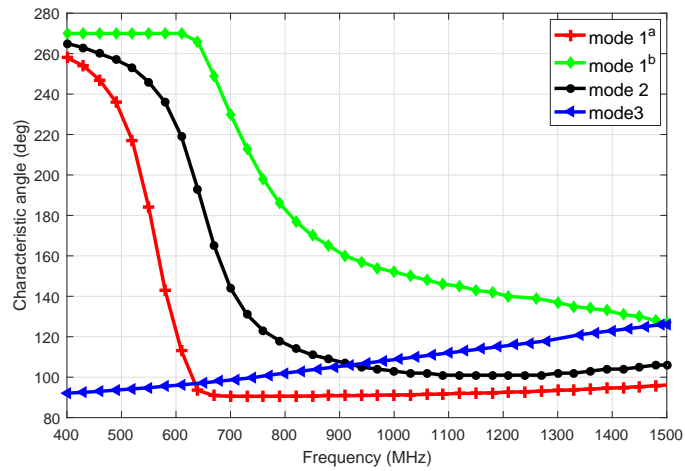
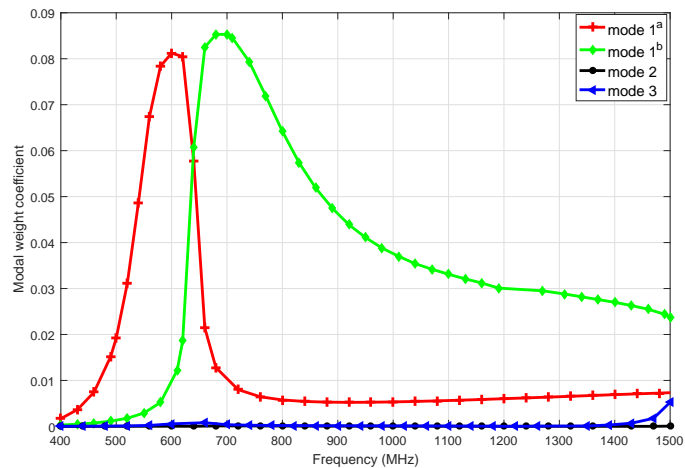


Figure 5.7: Modal current distributions and radiation patterns of (a) mode 1^a at 553 MHz, (b) mode 1^b at 809 MHz, (c) mode 2 at 654 MHz, and (d) mode 3 at 950 MHz on the structure containing a ring and a rectangular strip.



(a)



(b)

Figure 5.8: (a) Characteristic angles and (b) modal weight coefficients of modes 1^a , 1^b , 2, and 3 given in Fig. 5.7.

ring have opposite directions for mode 1^a , while their directions are the same for mode 1^b . Radiation patterns and current distributions on the ring structure in Figs. 5.7(c) and (d) are almost identical to those without a strip, and thus we still name them as mode 2 and mode 3.

Characteristic angles of mode 1^a , mode 1^b , mode 2, and mode 3 are presented in Fig. 5.8(a). According to these characteristic angle curves, mode 1^a resonates at 553 MHz, while mode 1^b resonates at 809 MHz. The resonant frequency of mode 2 is 654 MHz, and characteristic angles of mode 3 are still below 180° over the whole simulated

spectrum.

Applying a delta-gap source at the middle of the strip, the rectangular strip operates as a dipole. Its maximum near-field radiation is at the direction where the annular ring sees the maximum characteristic currents for mode 1^a and mode 1^b . Thence, the energy is well coupled to the annular ring and produces an induced current, and therefore the ring structure is excited. The modal weight coefficients of mode 1^a , mode 1^b , mode 2, and mode 3 are obtained and shown in Fig. 5.8(b). As we can see from this figure, only two modes (mode 1^a and mode 1^b) are significantly excited. Apparently, these two modes are not sufficient to cover the entire UHF TV spectrum, and hence more characteristic modes resonating in the UHF band are required to satisfy the UWB requirement.

Based on analyses above, in this work, variations of mode 1 and mode 2 will be utilized to contribute to the total radiation. Since mode 2 behaves similar to mode 1 but with current along an orthogonal direction, mode 1 and its variations are discussed next in detail.

5.3 Structure Modification and Feeding Refinement

5.3.1 Structure Modification

Since the resonant frequencies of modes 1^a and 1^b are 553 MHz and 810 MHz, respectively, to achieve a fractional bandwidth over 50% as required by the TV frequency band, a higher resonance at around 1200 MHz is expected. Therefore, a smaller ring is inserted into the original one as shown in Fig. 5.9 to generate more characteristic modes. Choosing $R_1 = 50$ mm and $k_0 = 0.6$, when $k_1 = 0.6$ and $k_2 = 0.83$ (i.e. $r_1 = 30$ mm and $r_2 = 25$ mm), the resonant frequency of mode 1 is 1287 MHz based on (4). In addition, the final resonant frequency might be smaller than the estimation because of the capacitance between feeding dipoles and rings.

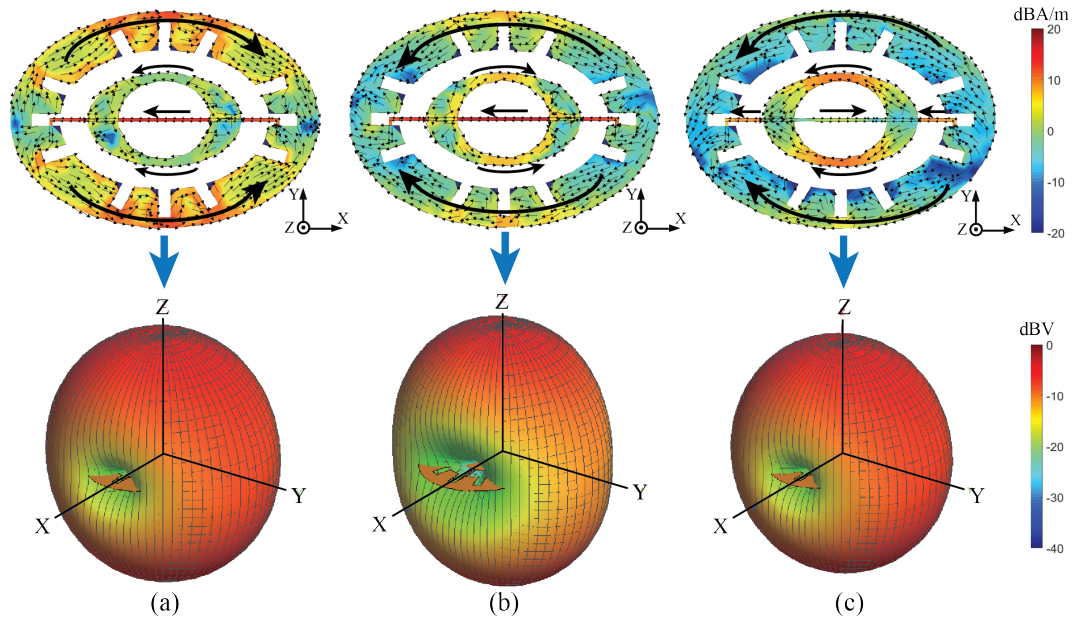
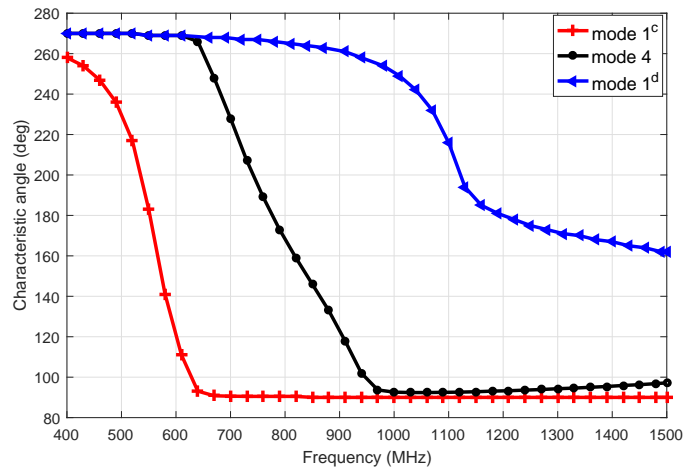


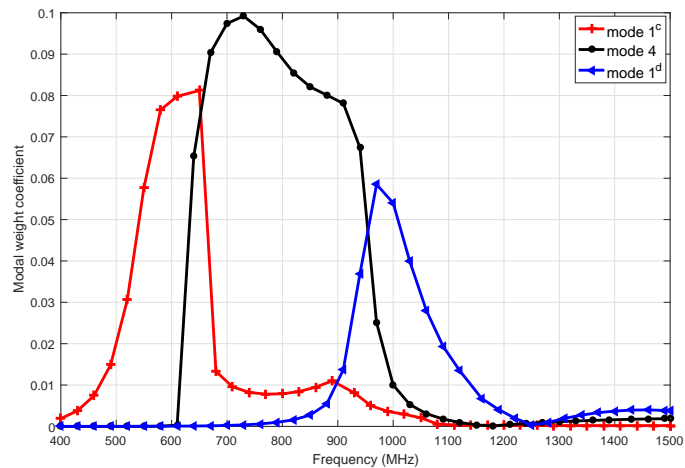
Figure 5.9: Modal current distributions and radiation patterns of (a) mode 1^c at 552 MHz, (b) mode 4 at 776 MHz, and (c) mode 1^d at 1198 MHz on the structure containing dual rings and a rectangular strip.

CMA simulation is then performed on the structure with dual rings and modes with currents along the long axis of the ring are given in Figs. 5.9(a), (b), and (c), which are named as mode 1^c , mode 4, and mode 1^d , respectively. All the three modes can be regarded as variations of mode 1 owing to similar radiation patterns with that of mode 1, and their characteristic angles are presented in Fig. 5.10(a). From Fig. 5.8(a) and Fig. 5.10(a), the characteristic angle curve of mode 1^c overlaps with that of mode 1^a , which is reasonable because the two modes have almost identical current distributions on the outer ring, and the current of mode 1^c is weak on the inner ring. The reason the mode with current distribution shown in Fig. 5.9(b) is named as mode 4 is that its currents on the outer and inner rings have close strengths but opposite directions, and more importantly, this is a new mode whose property is contributed by both the two rings. Based on Fig. 5.9(c), mode 1^d is mainly determined by the inner ring and it resonates at 1198 MHz, which is close to the estimation before.

Using the thin strip as a driven element, the modal weight coefficients of modes 1^c ,



(a)



(b)

Figure 5.10: (a) Characteristic angles and (b) modal weight coefficients of modes 1^c, 4, and 1^d given in Fig. 5.9.

4, and 1^d are plotted at Fig. 5.10(b). It can be seen that weights of mode 1^c and mode 4 are high at frequencies close to their resonances, which indicates that they are properly excited. Comparing Fig. 5.8(b) and Fig. 5.10(b), it is observed that adding an inner ring not only creates higher resonances, but also achieves high modal weight coefficients over wider band. However, although the design at this stage has the potential to realize a good radiation from 1200 MHz to 1500 MHz due to the existence of mode 1^d, the long strip cannot excite this mode efficiently.

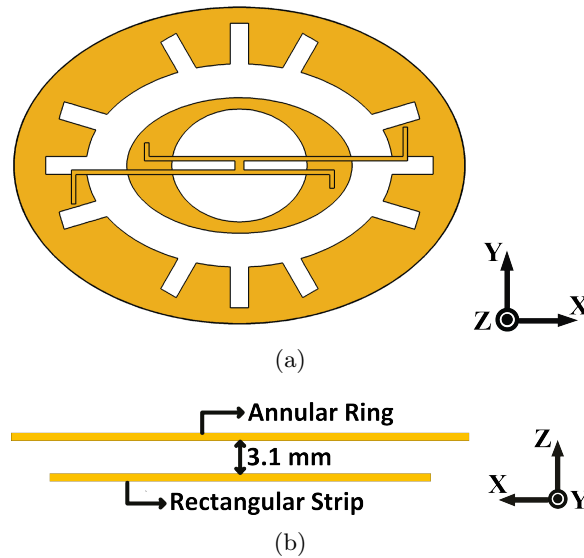


Figure 5.11: Structure layout of dual rings with two rectangular strips (a) top view and (b) side view.

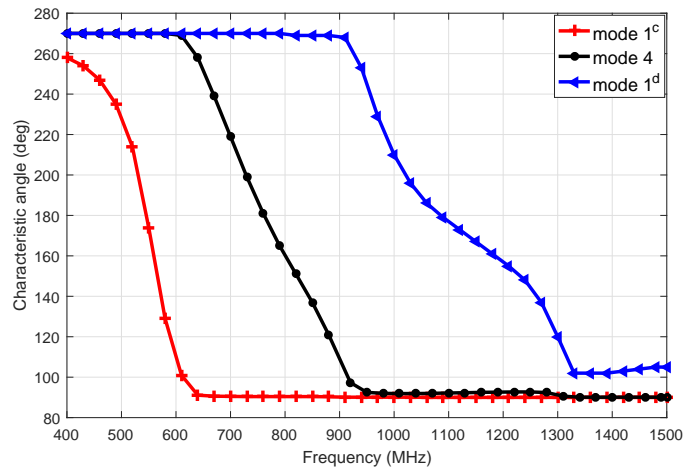
5.3.2 Feeding Refinement

To excite mode 1^d and to improve the antenna performance at the high frequency band, a shorter strip is added to the original feeding structure as illustrated in Fig. 5.11. With the additional strip, characteristic angles and modal weight coefficients of mode 1^c , 4, and 1^d are presented in Figs. 5.12(a) and (b). Comparing results in Fig. 5.12(a) and Fig. 5.10(a), it is noticed that adding a shorter strip has little effect to mode 1^c and mode 4, while characteristic angles of mode 1^d become less flat near its resonance. Nevertheless, after the feeding structure refinement, weights of mode 1^d near its resonance are higher as shown in Fig. 5.12(b).

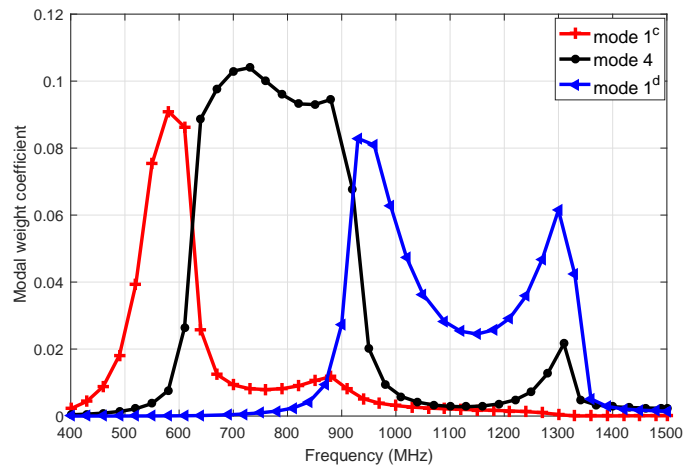
5.4 Antenna Optimization and Measurement

5.4.1 Antenna Optimization

After exciting all the expected modes having currents along the long axis of the ring, two dipoles along the short axis are used to excite variations of mode 2, and characteristic



(a)



(b)

Figure 5.12: (a) Characteristic angles and (b) modal weight coefficients of modes 1^c , 4, and 1^d corresponding to structure shown in Fig. 5.11.

modes of the whole structure are analyzed. As shown in Figs. 5.13(a) and (b), mode 2^c corresponds to mode 1^c , whose radiation mainly depends on the outer ring, but currents of mode 2^c are along the short axis of the ring. Similarly, mode 5 and mode 2^d are corresponding to mode 4 and mode 1^d , respectively. However, for mode 5, when the longer vertical strip is in operation, the shorter horizontal strip begins to work with the increase of frequency, and hence positions of current nulls are rotated. Operation of strips orthogonal to the original modal current directions also make current nulls of modes 1^d and 2^d rotate. It is worth mentioning that mode 2^d has not resonated over the

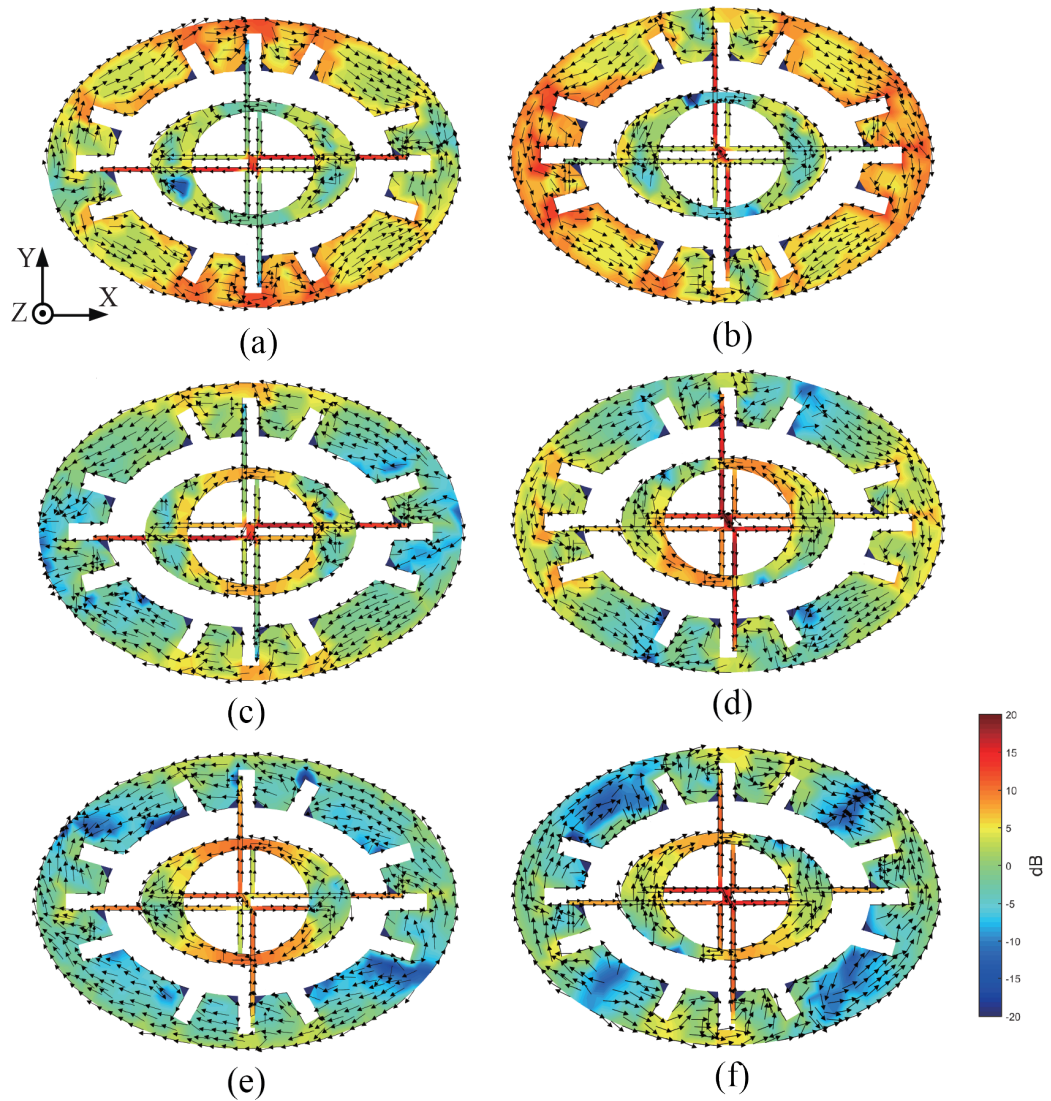
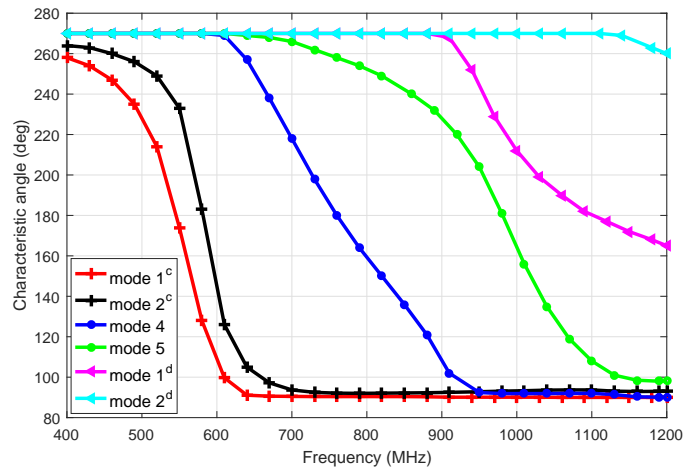


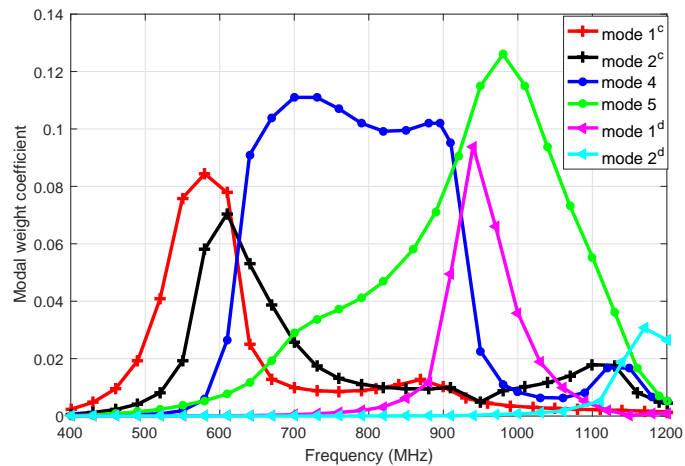
Figure 5.13: Modal current distributions on the structure containing two rings and four strips (a) mode 1^c at 546 MHz, (b) mode 2^c at 581 MHz, (c) mode 4 at 760 MHz, (d) mode 5 at 981 MHz, (e) mode 1^d at 1102 MHz, and (f) mode 2^d at 1500 MHz.

simulated frequency band according to Fig. 5.14(a), so its current distribution is given at 1500 MHz where the characteristic angle is the closest to 180° .

Characteristic angles and modal weight coefficients of modes 1^c , 2^c , 4, 5, 1^d , and 2^d are given in Fig. 5.14. According to Fig. 5.14(a), resonant frequencies of modes 1^c , 2^c , 4, 5, and 1^d are 546 MHz, 581 MHz, 760 MHz, 981 MHz, and 1102 MHz, respectively.



(a)



(b)

Figure 5.14: (a) Characteristic angles and (b) modal weight coefficients of modes 1^c , 2^c , 4, 5, 1^d , and 2^d given in Fig. 5.13.

In addition, modal weight coefficients shown in Fig. 5.14(b) indicate that the 5 modes contribute to the final radiation in turn.

As shown in Fig. 5.15, the structure is then printed on a 3.1 mm-thick Rogers5880 PCB board (with relative permittivity of 2.2 and loss tangent of 0.0009) for easier fabrication and further operating frequency reduction. The proposed structure is further simulated and optimized in the CST Microwave Studio with substrate included, and the final dimensions are summarized in Table 5-D.

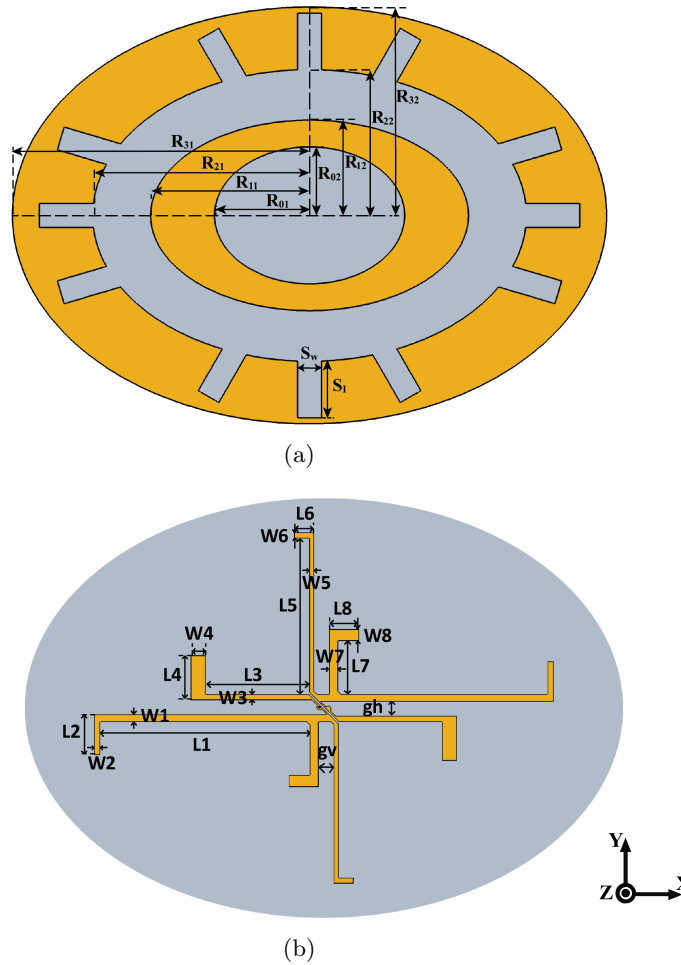


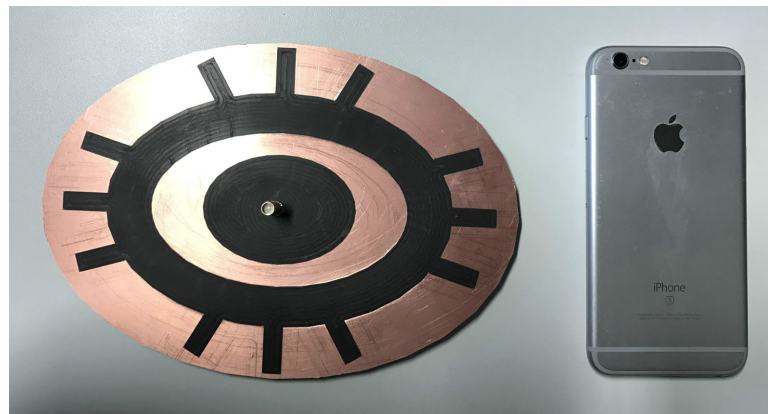
Figure 5.15: Structure layout of the final antenna (a) top view and (b) bottom view.

5.4.2 Antenna Measurement

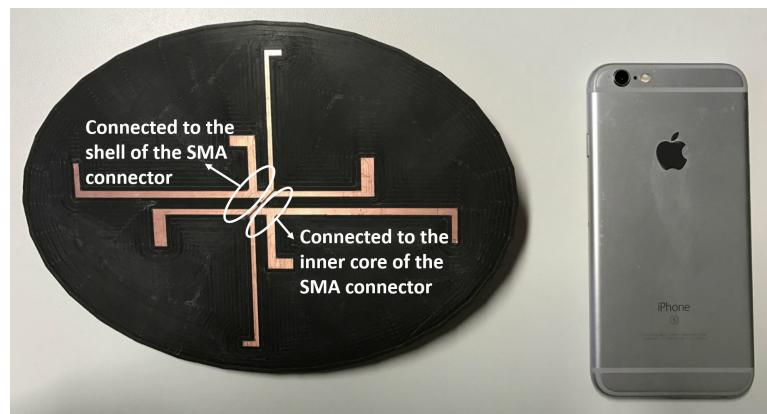
An antenna prototype is then fabricated and measured in Queen Mary University of London. Photos of the antenna are shown in Fig. 5.16. The simulated and measured reflection coefficients are given in Fig. 5.17(a), according to which, the proposed antenna achieves -10 dB impedance bandwidth from 470-987 MHz in measurement, and the simulated operation spectrum is from 470 MHz to 951 MHz. Fig. 5.17(b) gives the peak realized gain for the proposed antenna over 470-1000 MHz. It is observed that the measured gain is between 2.5 dBi and 3.8 dBi over the UWB operating frequency band. The measurement results agree well with those in simulation, and small differences might

Table 5-D: Dimensions of the proposed antenna.

Parameter	R_{01}	R_{02}	R_{11}	R_{12}	R_{21}	R_{22}	R_{31}
Value (mm)	30.9	21.5	55.1	31.2	73.0	49.0	100.0
Parameter	R_{32}	S_I	S_w	gh	gv	L1	W1
Value (mm)	70.0	19.1	8.0	4.6	5.6	69.9	2.2
Parameter	L2	W2	L3	W3	L4	W4	L5
Value (mm)	14.5	1.9	36.0	2.1	13.4	5.0	51.3
Parameter	W5	L6	W6	L7	W7	L8	W8
Value (mm)	1.8	6.2	1.9	18.0	2.8	9.9	3.9



(a)



(b)

Figure 5.16: Prototype of the proposed antenna (a) top view and (b) bottom view.

be introduced from measurement environment and fabrication imperfections.

The simulated and measured radiation patterns at 500 MHz, 600 MHz, 700 MHz, and 800 MHz in the XZ and YZ planes are shown in Fig. 5.18. Effects of cables and

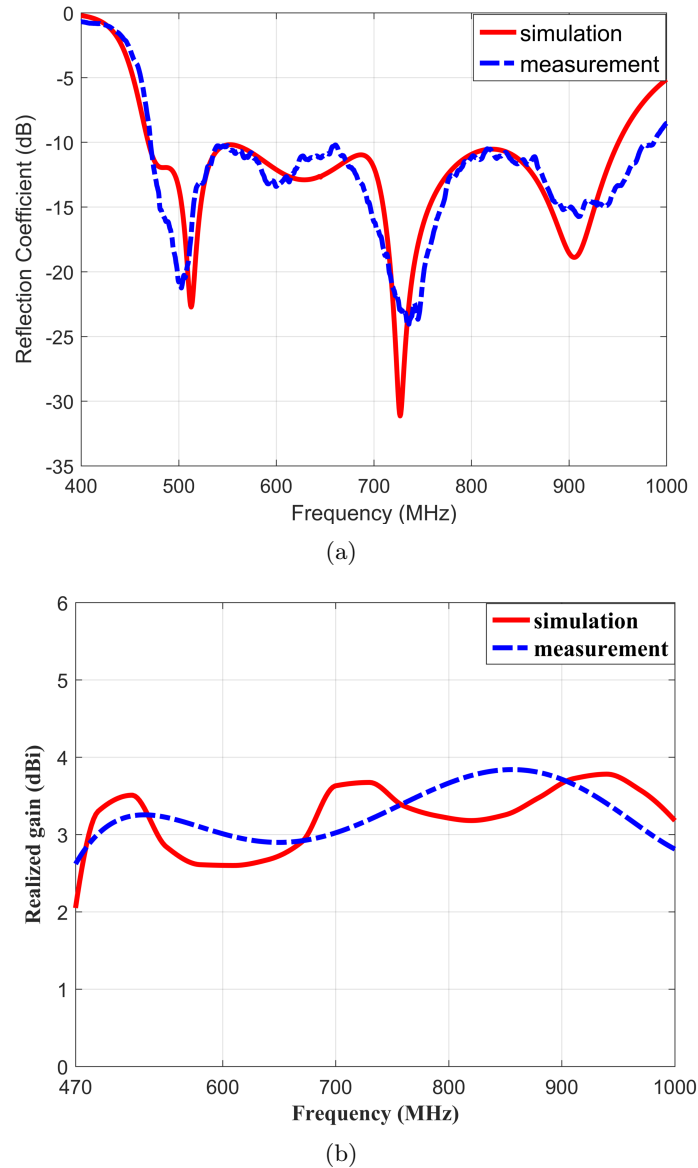


Figure 5.17: Simulated and measured (a) reflection coefficients and (b) realized gains of the proposed antenna.

unavoidable scattering in the chamber could be the source of discrepancies between measurement and simulation results. It is observed that the relative magnitudes of E_θ and E_ϕ vary with frequency, which is because multiple modes having orthogonal polarization directions are excited to different extents and the dominant resonant mode changes over the operating band. In practical, due to the random device directivities and the multipath effects resulted from complex IoT communication environment, signals have

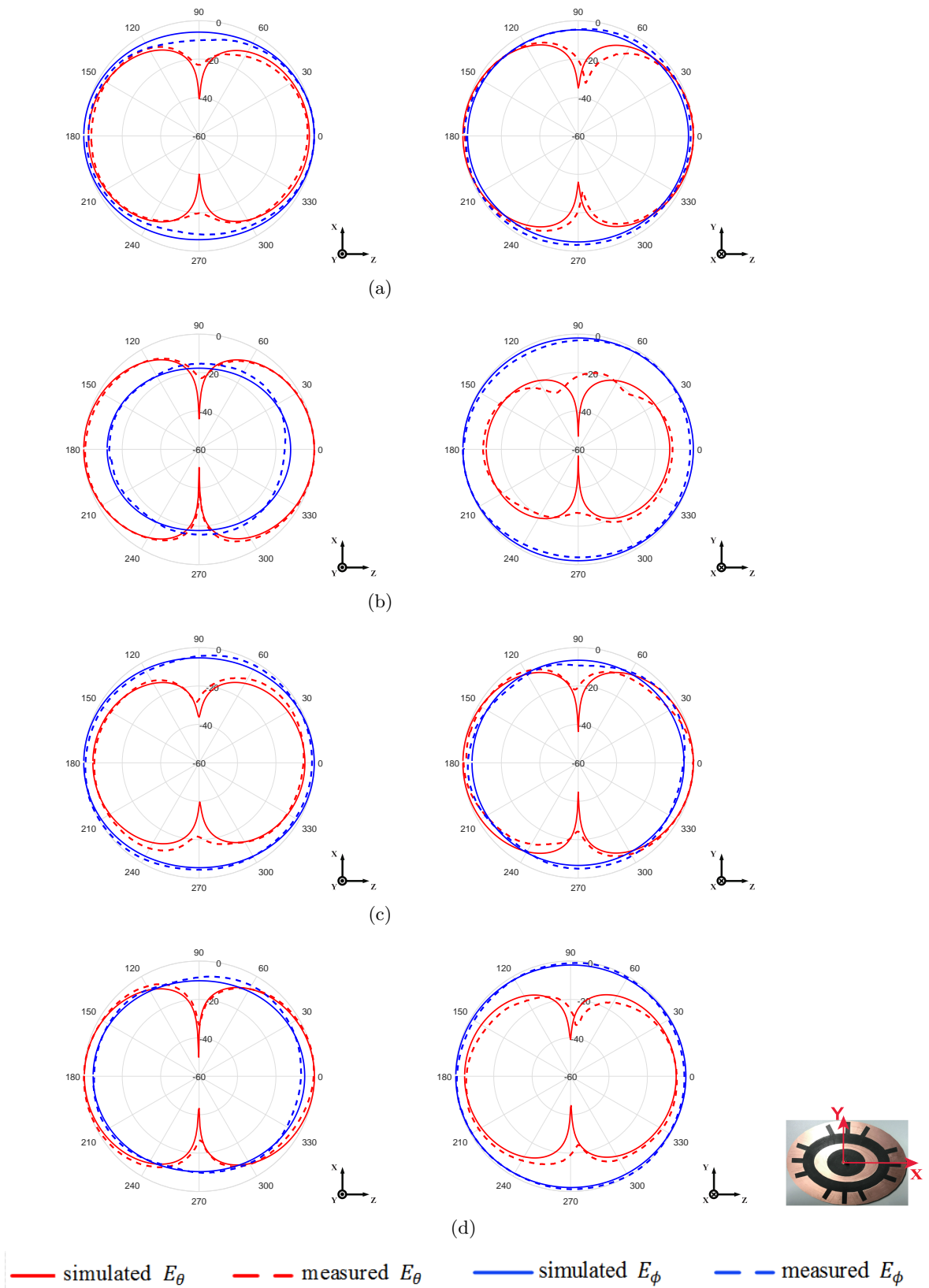


Figure 5.18: Simulated and measured radiation patterns at (a) 500 MHz, (b) 600 MHz, (c) 700 MHz, and (d) 800 MHz in the xz and yz plane.

random polarization directions. Nevertheless, a near-omnidirectional radiation pattern over the entire operating band is advantageous for practical applications [108, 109].

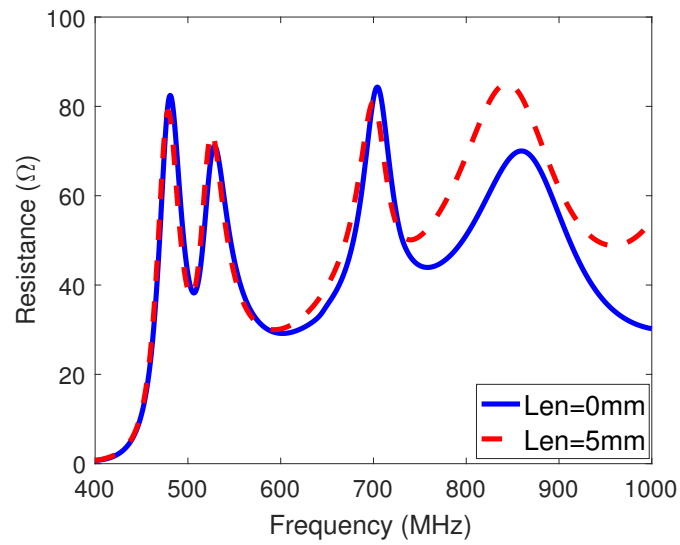
5.4.3 Discussions on the Unbalanced Coaxial Cable

It is noticed that feeding coaxial cable of the proposed antenna is directly connected to balanced strips. Since the coaxial cable is an unbalanced structure, currents on both arms of the strips are asymmetric and the leaky current on the outside surface of the coaxial cable will produce undesirable radiation and cause pattern distortion. In this section, effects on antenna performance introduced from the feeding coaxial cable are discussed in detail.

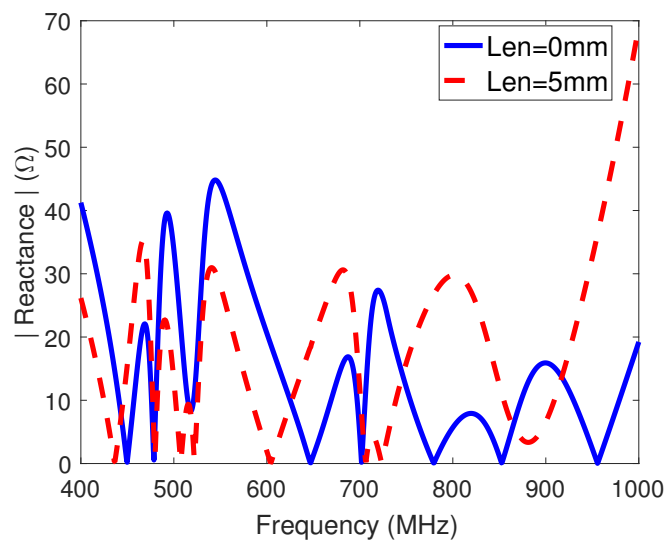
The proposed antenna is designed for IoT devices whose antennas are integrated with devices directly rather than connected through a long coaxial cable. Therefore, the proposed antenna is simulated with length of the coaxial cable (Len) swept as: $Len = 5\text{ mm}$, $Len = 25\text{ mm}$, and $Len = 45\text{ mm}$. In addition, I delete all components of the coaxial cable and use a discrete port to excite the antenna, which is noted as $Len = 0\text{ mm}$ in the following discussion.

Firstly, I compare input impedances for coaxial cable-fed and discrete port-fed structures. As a typical transmission line structure, the coaxial cable transforms the input impedance of the proposed antenna. Thence, when comparing with the discrete port excitation, the coaxial cable having length of $Len = 5\text{ mm}$ is used to avoid differences introduced by impedance transformation, and we can regard the impedance not being transformed on a 5mm-long coaxial cable over antenna's low operating frequency (below 1 GHz).

The complex impedance ($Z = R + jX$) of an antenna includes a resistance (R) and a reactance (X). The resistance is related to the electromagnetic energy loss from the port including radiation loss and dissipation loss. Substrates used for antenna and coaxial cable are Rogers 5880 with a loss tangent of 0.0009 and Teflon with a loss tangent



(a)



(b)

Figure 5.19: (a) Resistances and (b) absolute resistances for antennas fed by a discrete port and a 5 mm coaxial cable.

of 0.0002. Due to the very low material loss, for the sake of simplicity, I assume R is purely radiation impedance in the following discussion. The reactance is related to the electromagnetic energy storage in the near field region [110]. The resistances and absolute reactance for $Len = 0 \text{ mm}$ and $Len = 5 \text{ mm}$ are plotted in Fig. 5.19.

From Fig. 5.19(a), below 740 MHz, resistances for antennas with discrete port and

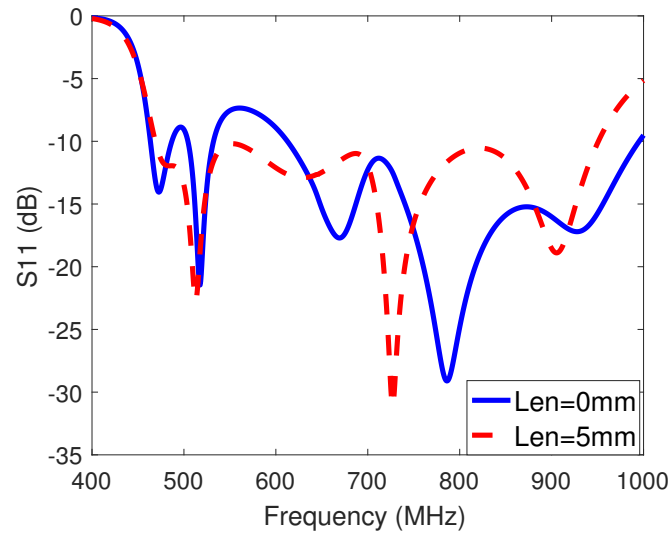


Figure 5.20: Reflection coefficients for antennas fed by a discrete port and a 5 mm coaxial cable.

coaxial cable are almost identical. As frequency goes higher, resistance of the antenna with coaxial cable becomes larger than that of using discrete port. This indicates that the leaky current on coaxial cable gradually contributes to radiation as frequency increases. Based on Fig. 5.19(b), the coaxial cable also affects the reactance impedance. However, regardless which feeding method is used, within the TVWS spectrum, the input impedance of the whole structure is around 50Ω and good impedance matching is ensured as proved by the reflection coefficients given in Fig. 5.20.

Furthermore, the proposed antenna fed by coaxial cables having different lengths are simulated and their reflection coefficients are given in Fig. 5.21. According to the results, good and stable impedance matching is achieved over the required spectrum when using short coaxial cables.

Based on the discussion about impedance, the coaxial cable does have some influence on port characteristics. Therefore, it is important to examine the distortion level of radiation pattern resulted from the leaky current. Radiation patterns of the proposed antenna with different cable lengths at 500 MHz and 800 MHz are presented in Fig. 5.22 and Fig. 5.23. Compare results in these two figures, we can see minor differences in YZ

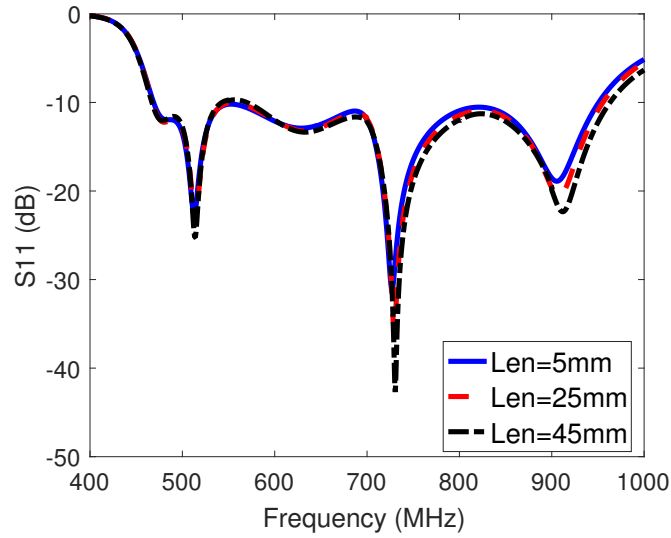


Figure 5.21: Reflection coefficients for antennas with different cable lengths.

and XZ planes for different cable lengths. In the XY plane, at 500 MHz, the difference between E_θ and E_ϕ is 34 dB when $Len = 0$ mm, and it grows to 30 dB when $Len = 45$ mm. At 800 MHz, the difference is 34 dB when $Len = 0$ mm and 22 dB when $Len = 45$ mm. Although the difference between E_θ and E_ϕ in the XY plane grows slowly as cable length increases, the cross polarizations are generally at the same level, and the radiation pattern is barely affected by short coaxial cables.

Apparently, with the increased length of coaxial cable or frequency, the radiation pattern of the proposed antenna would be gradually affected by the leaky current on coaxial cable. However, this is not a severe problem in my design owing to short electrical lengths of coaxial cables for IoT devices operating over TVWS. Therefore, there is no need to add a special balun structure and complicate current antenna design.

5.5 Summary

This Chapter presents a design procedure of a UWB antenna for IoT devices working at TVWS. Starting from a simple annular ring structure, the CMA is used as a powerful tool to provide insights into generating and exciting multiple modes to achieve wideband

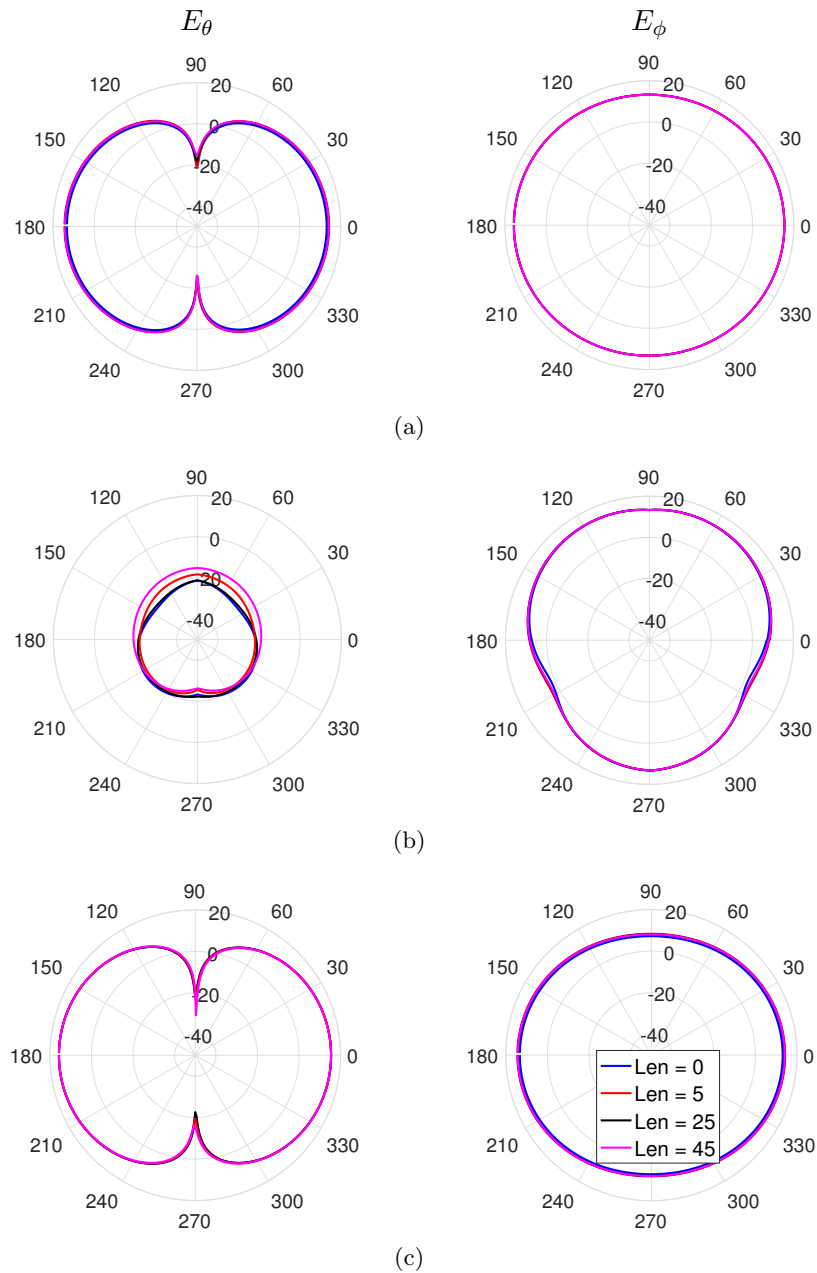


Figure 5.22: Radiation patterns of the proposed antenna with coaxial cables at different lengths at 500 MHz in (a) yz plane, (b) xy plane, and (c) xz plane.

performance. Based on current distributions of the desired characteristic modes on the annular ring, slots are cut on the structure to decrease modal resonant frequencies. In addition, by inserting a smaller ring into the original one, more characteristic modes resonating in the interested frequency band are generated and the UWB property is

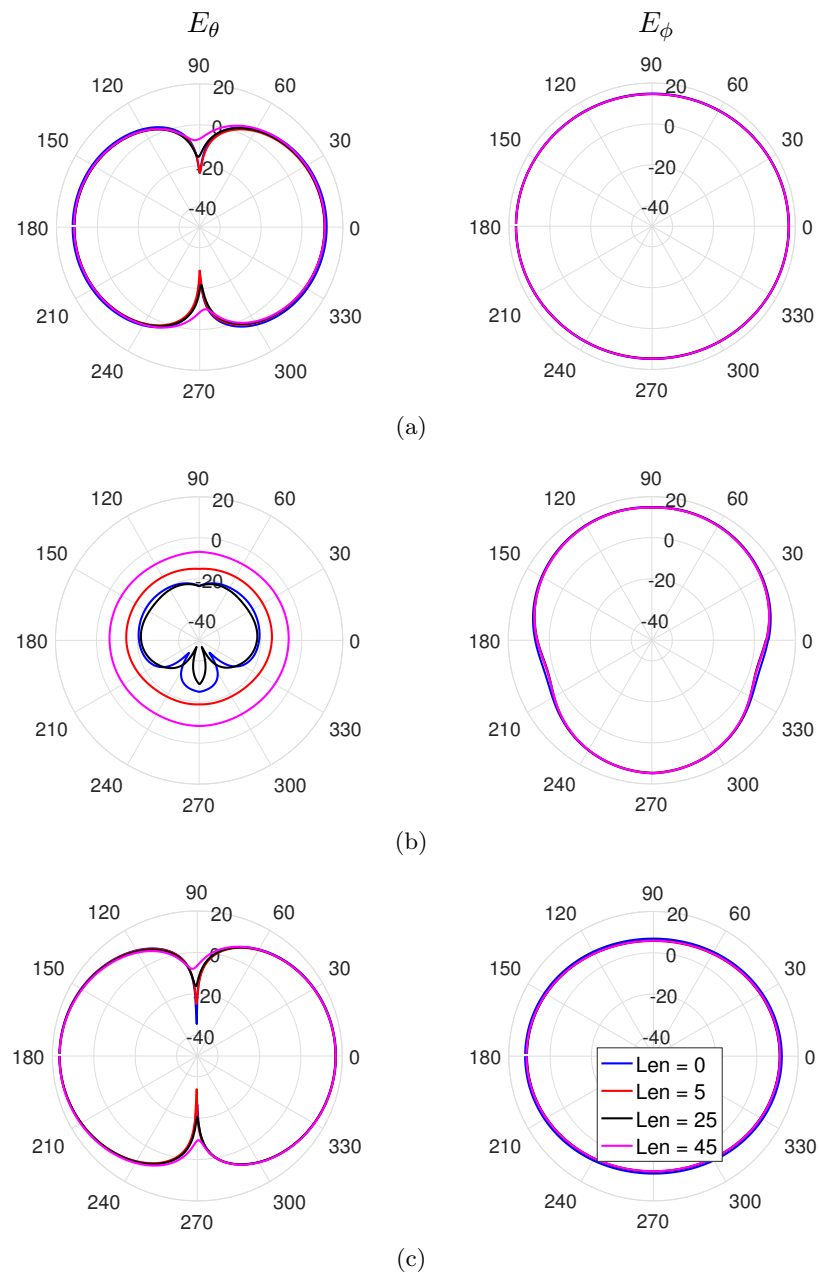


Figure 5.23: Radiation patterns of the proposed antenna with coaxial cables at different lengths at 800 MHz in (a) yz plane, (b) xy plane, and (c) xz plane.

established. By observing properties of each mode, the feeding structure is designed to excite all the desired modes efficiently, and the UWB performance is finally achieved through combining resonances of multiple modes. Although the final antenna structure is complicated, the design methodology and the functionality of each component are

clear. Furthermore, the resonant frequency of each characteristic mode can be tuned by changing dimensions of the two rings, and the modes can be excited selectively. Therefore, this design procedure for UWB antenna using CMA could be flexibly applied to satisfy various antenna design requirements. For example, by tuning modal resonances to widely separated frequencies, multi-band antennas could be achieved.

Chapter 6

System Measurement

6.1 Introduction

Both narrowband and wideband TVWS antennas have been designed and discussed in previous chapters. However, performance of these antennas was verified by just measuring themselves in anechoic or reverberation chambers. Through integrating in-house developed antennas into IoT devices operating over TVWS, this chapter measures their system performance in practical scenarios. Moreover, potentials of TVWS for enabling sensor nodes and establishing network within a cluster of buildings are also explored. Specifically, the related work on IoT and TVWS systems measurements, as well as the main contributions of this chapter are reviewed in Section 6.1. Section 6.2 integrates the miniaturized antenna proposed in Chapter 3 into a sensor node and measures its system performance. The UHF TV spectrum at QMUL is monitored and discussed in Section 6.3. Then, the UWB antenna designed in Chapter 4 and a commercial antenna are connected to a TVWS device (TVWSD), and their system performance on different communication links are measured and analyzed in Section 6.4. Finally, Section 6.5 concludes this chapter.

6.1.1 Related Work

Researchers have built and evaluated various IoT systems. Alonso *et. al* [111] proposed a low cost humidity sensor tag consisted of a dipole antenna and a chip. Attached the tag to a plant pot, signal strengths received by the reader varied with different substrate permittivities resulted from different soil humidities. System tests demonstrated that increasing the water from 0 mL to 100 mL, the received signal strengths ranged from -24 dBm to -31 dBm. Focused on dynamic adaptive video streaming, Luca *et. al* [112] built a TVWS network to connect to the Internet. Presenting the results of field tests, they showed that the TVWS exhibited larger communication range than other 802.11 protocols. Gao *et. al* [113] pointed out that TVWS approaches were very promising means to handle the billions of connected IoT devices in a highly flexible, reliable and scalable way. They proposed a cognitive radio enabled time division (TD)-LTE test-bed to realize the dynamic spectrum management over TVWS. They also proposed a hybrid framework for the dynamic spectrum management of machine-to-machine networks.

In addition, in previous research, the indoor and outdoor measurements of spectrum utilization have been conducted with single or multiple measurement campaigns. Kliks [114] *et. al* carried out indoor measurements in Barcelona and Poznan, which exhibited different occupations of the TV channels for heterogeneous networks (HetNets). Experimental analyses of the indoor TV signals propagation characteristics were also given. Islam *et. al* [115] measured the 24-hour spectrum usage ranging from 80 MHz to 5.85 GHz on the roof of Institute for Infocomm Researchs building for 12 weekday period in Singapore. Taher *et. al* [116] conducted similar fixed node measurement in Spain ranging from 75 MHz to 3 GHz in Nord campus of Universitat Politcnica de Catalunya.

6.1.2 Contribution

Most of the previous work evaluated the whole IoT/TVWS systems or communication environments from the field tests. On the contrary, integrating predesigned antennas

into IoT devices and testing them at different environments, this work focuses more on assessing antennas' characteristics from systems' point of view. Inspired by worldwide spectrum utilization measurements, the TV spectrum at QMUL is also measured. The main contributions of this chapter are summarized as follows:

- The miniaturized antenna proposed in Chapter 3 is integrated into a compact sensor node. With the node pointing in different directions, signals transmitted by it are detected by both another node with a commercial antenna and a spectrum monitoring system when measuring in an anechoic chamber.
- The UWB U-shaped printed monopole antenna designed in Chapter 4 is integrated with a spectrum monitor, and the whole UHF TV spectrum at QMUL is detected to distinguish spectrum resources for TVWS. To ensure accurate measurements, the spectrum is detected again with the monitor being equipped with a commercial antenna.
- Communications are established over a licensed TVWS channel. The UWB U-shaped printed monopole antenna is connected to a TVWS client, and pointing in different directions, its system performance is compared with that of a commercial directional UHF antenna. Complicated transmission environments imposed by factors like communication distances (from 10 m to over 120 m), offices, construction facilities, etc. are considered.

6.2 Sensor Node Enabled by a Miniaturized Narrowband Antenna

6.2.1 System Description

A sensor node for the IoT applications is illustrated in Fig. 6.1. Its diameter and height are 103 mm and 95 mm, respectively, and the battery is embedded inside of it. Operating



Figure 6.1: Sensor node with (a) a commercial spiral antenna and a serial port extension and (b) the in-house developed antenna.

at 474 MHz, the transmitting power of this node is 17 dBm. The node in Fig. 6.1(a) uses a spiral antenna for signal transmission and reception. In Fig. 6.1(b), the miniaturized planar disc antenna developed in Chapter 3 is integrated into the node. According to Chapter 3, at 474 MHz, the realized gain of the in-house developed antenna is around -2 dBi.

Communication is set up in an anechoic chamber as Fig. 6.2 demonstrated to avoid undesired noise like digital broadcasting signals transmitted near 474 MHz. The node with the in-house developed antenna is placed at point **P** (as marked in Fig. 6.2) and acts as a transmitter. At the other side of the chamber, another node having spiral antenna is fixed at point **Q** and operates as a receiver. RS232 serial port is extended from the receiver to enable the received data being accessible by external equipment as shown in Fig. 6.1(a). Having the same height, the transmitter and the receiver are 4.5 m away from each other. Since nodes are usually arbitrarily placed, which leads to signals having random polarization directions in practical, the transmitting node is rotated in the horizontal plane during measurement to observe system performance of the in-house developed antenna.

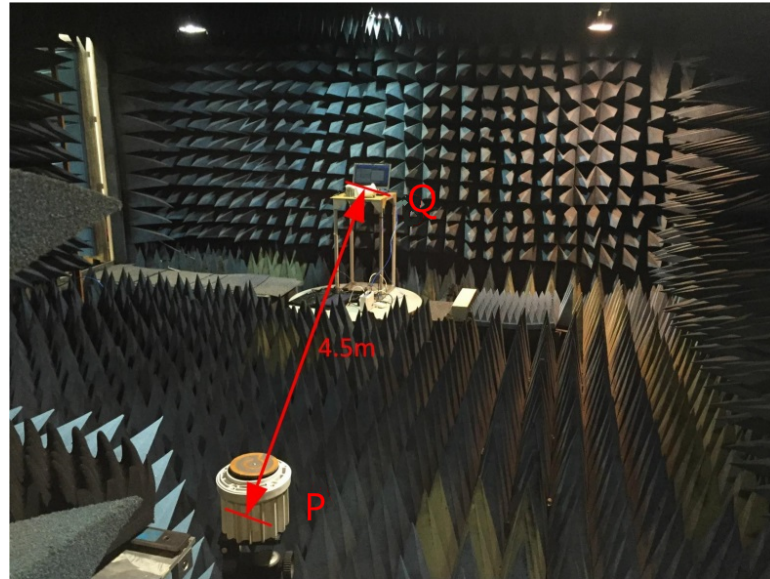


Figure 6.2: Measurement setup in an anechoic chamber.

6.2.2 Measurement Results and Discussions

After the communication between the transmitter and the receiver started, a spectrum monitoring system provided by CRFS Limited is used to monitor the radio spectrum. Fig. 6.3 gives the detected spectrum from 470 MHz to 480 MHz, from which it can be observed that the signal strength at 474MHz is about 65 dBm higher than those at other frequencies. Since the measurement is conducted in a chamber where other electromagnetic services are unavailable, the peak signal is emitted from the sensor node.

To ensure the placement orientation of the sensor node does not significantly affect performance of the IoT communication system, links are established with the transmitter sensor node having different orientations. As a reference, angle between the line connecting two opened loops on the in-house developed antenna and the diagonal line of the stand holding the transmitting node is defined as θ . During measurement, the node is adjusted to make θ equals to 45° , -45° , -135° and 135° as noted by **A**, **B**, **C** and **D** in Fig. 6.4.

Peak signal strengths detected by the spectrum monitor are recorded every two minu-

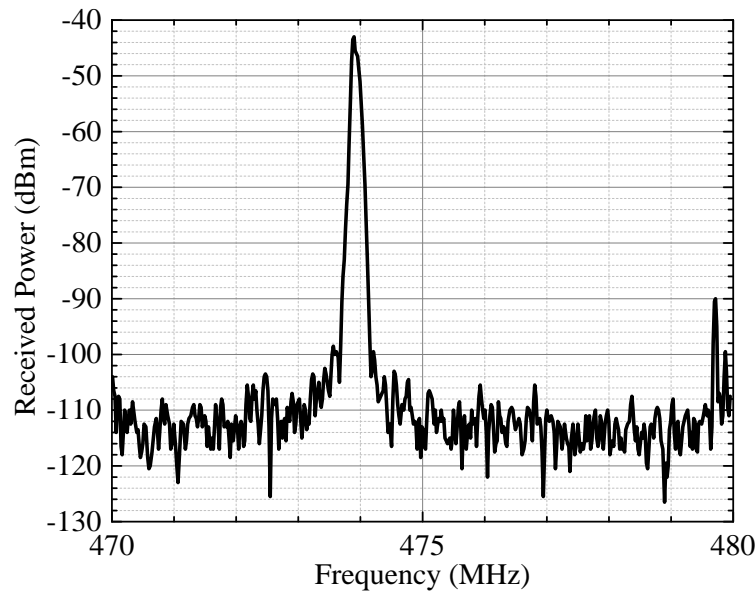


Figure 6.3: Detected signal intensity over 470-480 MHz.

tes and four data is recorded in total at each orientation angle. Normalized signal strengths are plotted in Fig. 6.4 at the corresponding angles together with illustrations of the transmitter. It is noted that data for each node orientation is separated by a small degree to be distinguished. According to Fig. 6.4, difference of signal strengths at one position is less than 2.5 dBm, which can come from inevitable scattering in the chamber. For node placed at different θ , the maximum difference is 4.5 dBm. Eliminating the environment effect which could lead to 2.5 dBm difference, the spectrum monitoring system detects signals varying within 2 dBm sent from node rotating to different orientations. Thus, the in-house developed antenna exhibits stable performance and the device orientation has little effect on its system performance.

The received signal strength indicators (RSSIs) given by the receiving sensor node are summarized in Table 6-A. Based on Table 6-A, difference between RSSIs at **A** and **D** are 4 dBm, which comes from environmental effects and gain difference introduced from the change of transmitter orientations. These received RSSIs are in coincidence with differences between the peak power and those over the rest of the spectrum given by the spectrum monitor. Further measurements demonstrate that the communication distance

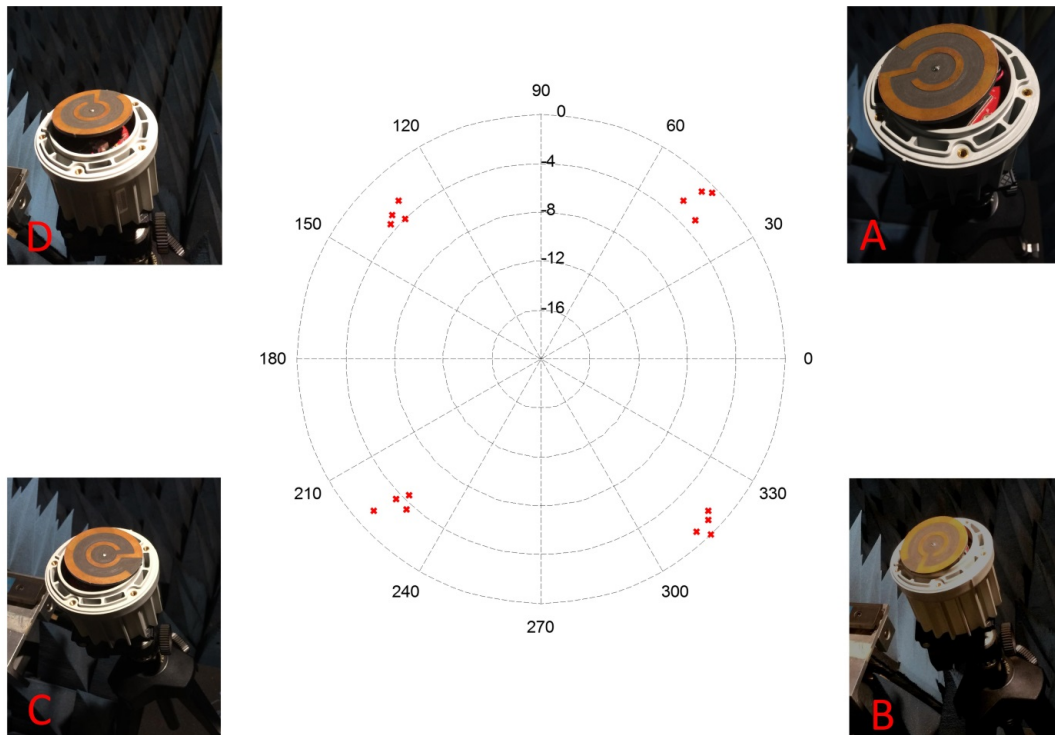


Figure 6.4: Normalized peak signal strengths detected by the spectrum monitor when the transmitter turns to different directions.

Table 6-A: Received RSSIs with the transmitter turning to different directions.

Transmitter orientation	RSSI/dBm
A	-64
B	-66
C	-67
D	-68

between the node with a spiral antenna and the node with the in-house developed circular antenna is up to 20 m outside the anechoic chamber.

6.3 UHF TV Spectrum Monitoring

6.3.1 System Description

The whole UHF TV spectrum is detected at QMUL in this section to verify the abundant spectrum resources provided by the TVWS for IoT communications. During measurement, the U-shaped printed monopole antenna proposed in Chapter 4 is connected to the RFeye system provided by CRFS Limited for intelligent spectrum monitoring [117]. The testing system consists of a RFeye node panel, a logger control box, a laptop with the RFeyeSite software installed and a USB memory stick.

The in-house developed antenna is connected to the RFeye node as shown in Fig. 6.5(a). On the RFeyeSite software, the start and the end detection frequencies are set to 470 MHz and 790 MHz, respectively, and 320 kHz (0.1% of the bandwidth of the UHF TV spectrum) is chosen for resolution bandwidth. When monitoring the spectrum, the whole system is placed at Room 353 of the Engineering Building, whose floor plans will be given in Fig. 6.11 in the following section, in QMUL.



Figure 6.5: RFeye node with (a) the in-house developed antenna and (b) a commercial antenna.

6.3.2 Measurement Results and Discussions

The measured data is exported from the USB memory stick and plotted in Fig. 6.6. Using -90 dBm signal intensity as a threshold, occupation statuses of the UHF TV channels are given in Fig. 6.7.

We can interpret from Fig. 6.6 and Fig. 6.7 that the UHF TV channels from 36 to 60 are vacant, which can result from two reasons: few signal transmission above 600 MHz and/or poor system performance of the in-house developed antenna at high frequencies. To prove the usability of the proposed antenna in systems, the spectrum is monitored again at the same location with the same settings, but the antenna connected to the RFeye node is changed to a commercial one provided by the CRFS Limited as illustrated in Fig. 6.5(b). The commercial antenna has an omnidirectional radiation pattern with a gain of 2 dBi and a VSWR of 1.7:1. Detected signals with the commercial antenna is also plotted on Fig. 6.6 for easy comparison with results acquired from using the in-house developed antenna. The two curves coincide well with each other, and small discrepancies can be caused by variances of the noise at different time as well as the gain

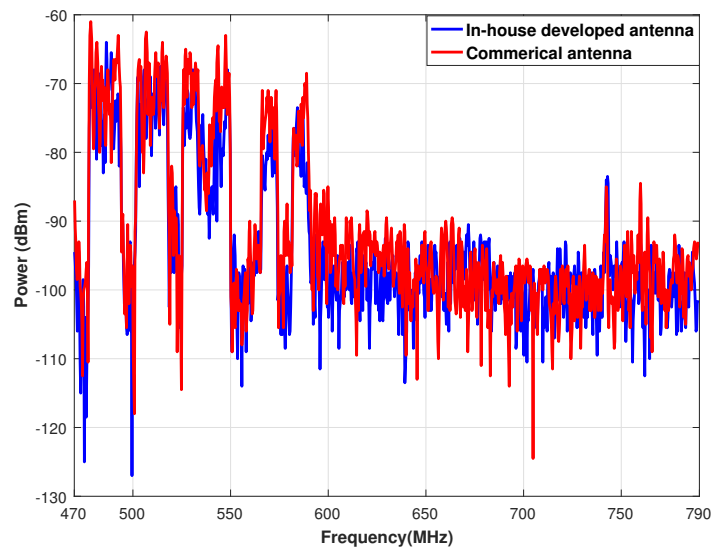


Figure 6.6: The UHF TV spectrum detected by a spectrum monitor equipped with the in-house developed antenna and a commercial antenna.

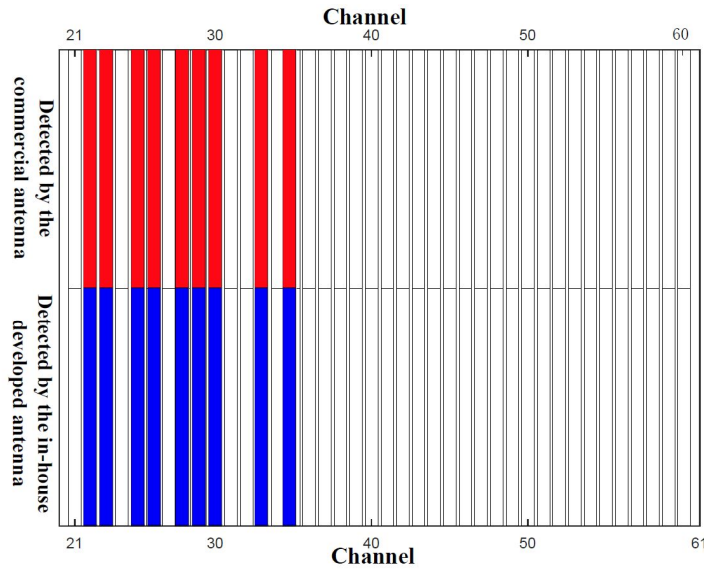


Figure 6.7: Channel occupation of the UHF TV spectrum.

and the VSWR difference of the two antennas. Hence, the in-house developed antenna shows good system usability over the entire UHF TV spectrum and there are abundant vacant channels for the TVWS.

6.4 TVWS Network Provisioning with Directional and Omnidirectional Terminal Antennas

6.4.1 System Description

After measuring TV channel occupancy at QMUL and verifying usability of the in-house developed antenna, a communication link is established over a channel where a TVWS spectrum license has been granted by Ofcom for real-time wireless transmissions. The measurement set-up is based on the RuralConnect TV White Space Radio provided by Carlson Wireless Technologies [118]. This radio follows a Carlson proprietary standard, which is close to IEEE 802.22 in characteristics, to provide wireless network access using TVWS. The set-up of both TVWS base station and clients is described as follows.

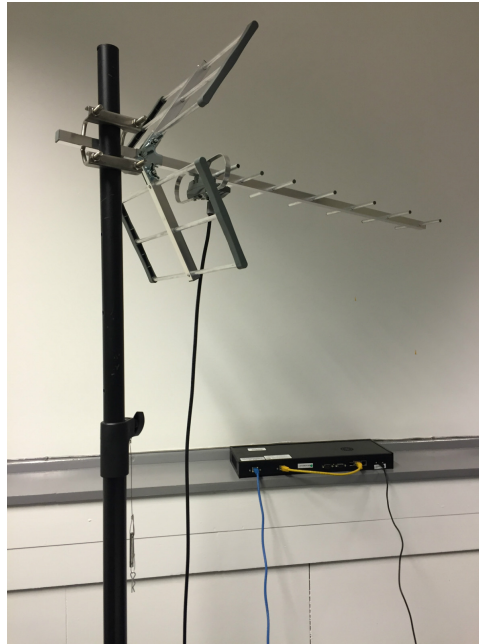


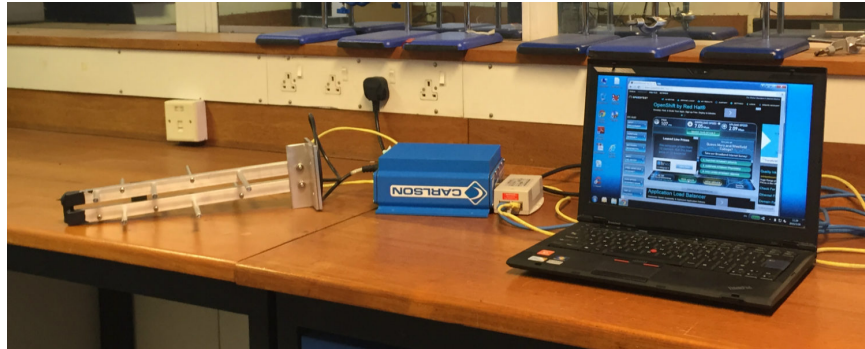
Figure 6.8: Yagi-Uda antenna connected to the base station.

1) *TVWS Base Station:*

The base station shown in Fig. 6.8 is placed at the third floor of the Electronic Engineering (EE) Building in QMUL. Connected to the Ethernet, the base station has a radio frequency transmit power of 23 dBm. Signals are transmitted from a directional Yagi-Uda antenna whose gain is 11 dBi and its feeding cable has 1 dB loss, and hence the equivalent isotropically radiated power (EIRP) is 33 dBm. Position and direction of the base station antenna are fixed, and its maximum radiation direction is set towards the northwest direction and 33.25 m above the mean sea level.

Table 6-B: Comparison between antennas connected to the TVWS client: the in-house developed printed monopole antenna and the commercial log-periodic antenna.

Antenna Index	In-house developed printed monopole antenna	Commercial log-periodic antenna
Dimension (cm ³)	23.1×3.5×0.8	38.1×35.56×10.1
Weight (Kg)	0.02	0.91
Frequency (MHz)	470-884	470-786
Beam width (3 dB down)	80° vertical Horizontal omnidirectionally	35° vertical 30° horizontal
Polarization	Linear	Linear
Gain (dBi)	1.7	9
Interface	50 Ω female SMA connector	75 Ω Female F-type Connector



(a)



(b)

Figure 6.9: (a) Commercial log-periodic antenna and (b) in-house developed printed monopole antenna connected to the client.

2) TVWS Client:

RuralConnect clients use external antennas, and the U-shaped printed monopole antenna presented in Chapter 4 is connected to the client to test its system performance. For comparison, a commercial log-periodic antenna [7] is also connected during measurement. Set-up of the client connected with the in-house developed printed monopole antenna and the commercial log-periodic antenna is shown in Fig. 6.9. Properties and sizes of the two antennas are listed in Table 6-B. According to Table 6-B, the in-house developed antenna is 211.6 times smaller and 45.5 times lighter than the commercial antenna. Owing to its large size, metallic structure and narrow beamwidth, the gain of the commercial antenna is 7.3 dBi higher than the in-house developed antenna. Radiation patterns on the elevation and the azimuth planes of the two antennas are given in Fig. 6.10, from which it can be seen that having an omnidirectional radiation pattern,

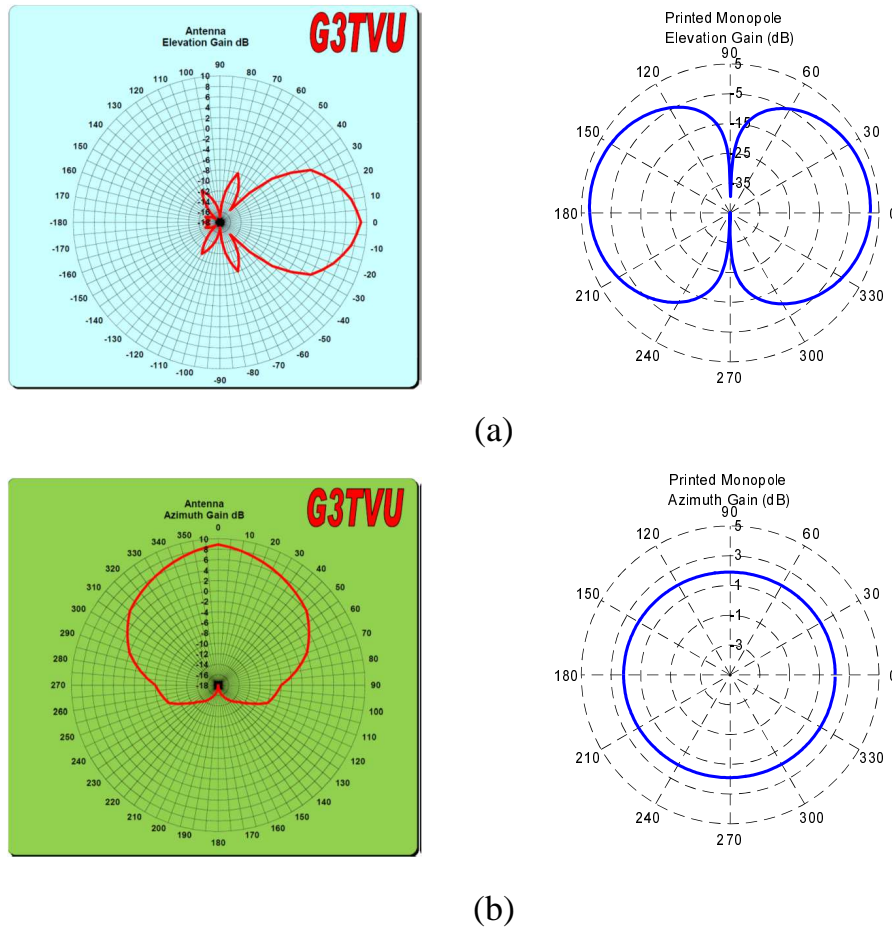


Figure 6.10: Radiation patterns of the commercial log-periodic antenna [7] and the in-house developed printed monopole antenna in (a) elevation plane and (b) azimuth plane at 630MHz.

the in-house developed antenna should see less signal strength variation when pointing at different directions. Moreover, the about 2 dBi gain realized by the in-house developed antenna is efficient for clients in TVWS radio communication systems, and this will be verified in results of a series of tests given in Section 6.4.3. Moreover, a laptop is connected to the client to monitor realized wireless network speeds as shown in Fig. 6.9.

6.4.2 Measurement Location Selection

Tests are conducted among buildings of EE, Computer Science (CS), Peoples Palace and Informatics Teaching Laboratory (ITL) at QMUL. EE building has three sections

and Section I and Section II are connected through a corridor at the second floor. The base station is fixed at Room 358 in the EE building as depicted in Fig. 6.11. Standing next to base station, the sector antenna points at northwest and is 15 m higher than the ground floor. During transmissions, signals undergo reflection, fading and multipath interference due to people, office facilities, walls, trees, etc. Therefore, moving client to different locations, seven links representing different communication scenarios are tested.

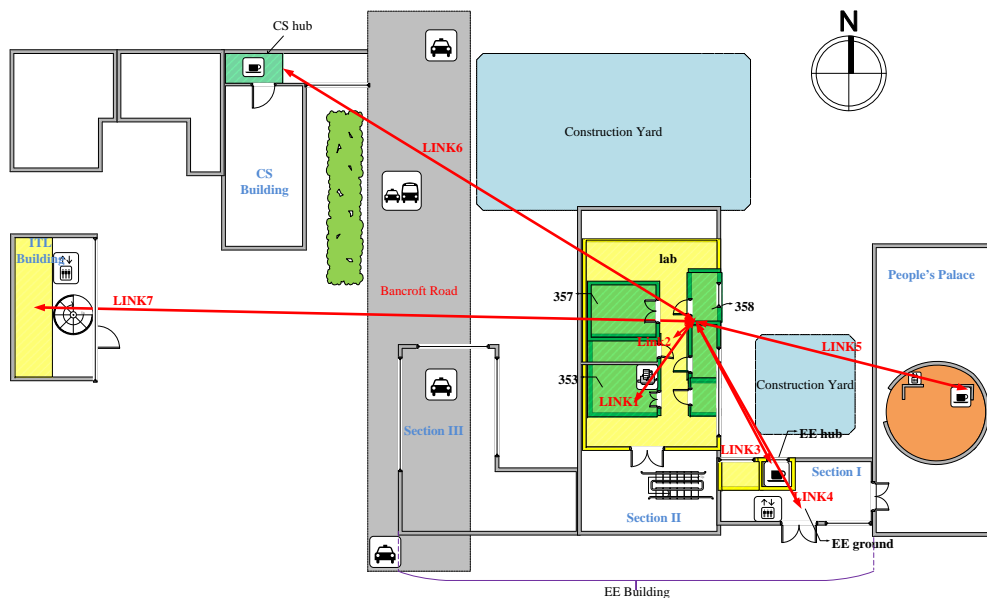


Figure 6.11: Floor plans of EE building (composed of Section I, Section II and Section III), People's Palace, CS building and ITL building. The ground floor is in white, the first floor is in orange, the second floor is in yellow, and the third floor is in green.

- Link1: The client is in Room 353 and it is 12.65 m away from the base station. In the shortest transmission path, signals go through three walls to reach the client.
- Link2: The client moves to the Electronic Lab which is just one floor below Room 358.

- Link3: The client is in EE hub on the second floor in Section I of EE building, and the distance between the client and the base station is 37.25 m. Although they are located at different sections of EE building, Room 358 can be seen from the window of EE hub.
- Link4: The client is three layers lower than the base station when being placed at the ground floor of Section I of EE building. There are several walls and distance of 47.33 m between the client and the base station. However, space between Section II of EE building and Peoples Palace is under construction, and signals from the base station have to go through much metal construction site equipment to arrive at the client.
- Link5: In the fifth link, the client is on the first floor of Peoples Palace. Distance between the client and the base station is 56.77 m. In addition to the construction yard, signal transmitted to and from the client situating in a corner can also be affected by the two walls surrounding it.
- Link6: CS hub is also on the third floor and it is 78.19 m away from Room 358. CS building is very complicated and there are many offices between the client and the base station. Besides, tall trees are outside CS building, and the Bancroft Road between EE and CS buildings is busy.
- Link7: This link is 127.5 m and goes through Room 358, Room 357, edge of Section III of EE building and a busy road. The client is one floor lower than the base station. Nevertheless, ITL building has French windows.

6.4.3 Measurement Results and Discussions

During measurement, there is an ongoing construction between the EE building and Peoples Palace and another next to Section II of EE building as illustrated in Fig. 6.11. The log-periodic antenna and the printed monopole antenna are connected with client

Table 6-C: Variances of SINRs acquired when client antennas facing at different directions.

Links	Uplink (dB) (log-periodic antenna)	Uplink (dB) (printed monopole)	Downlink (dB) (log-periodic antenna)	Downlink (dB) (printed monopole)
Link1	1.699	0.987	2.151	0.662
Link2	2.112	1.350	1.890	0.700
Link3	1.802	1.325	0.795	1.122
Link4	3.871	1.527	2.939	1.365
Link5	1.307	1.792	2.834	1.427
Link6	4.386	1.945	7.024	2.063
Link7	2.050	1.823	2.155	0.427

respectively in each link, and both of them point at southeast, southwest, northeast and northwest in turn. When each antenna points at one direction, signal-to-interference-plus-noise ratios (SINRs) and speeds of both uplink and downlink are measured four times to remove effects of environment variation during a short period of time. Measurement results with antenna orientation being taken into account are plotted in Fig. 6.12, in which blue symbols stand for SINRs acquired using the log-periodic antenna at client, while red symbols for using the printed monopole antenna. SINRs of uplink signals are noted by 'o' and those of downlink are noted by '+'.

- Link1 and Link2 are in-section transmissions. Link3 and Link4 are in-building but between-section transmissions, and Link5, Link6 and Link7 are between-building transmissions.
- When base station and client are close to each other, strong signals are distributed in the entire environment and according to Fig. 6.12 (a), (b) and (c), both uplink and downlink SINRs achieved by the printed monopole antenna and the log-periodic antenna at every direction are high and have similar values.
- Signal strengths in Link5 and Link6 degrade due to further distance between base station and client and complex transmission environment including increased number of walls, trees, constructions and people in common areas as described in Chapter 6.4.2.
- Although having the longest communication distance, signal transmission in Link7

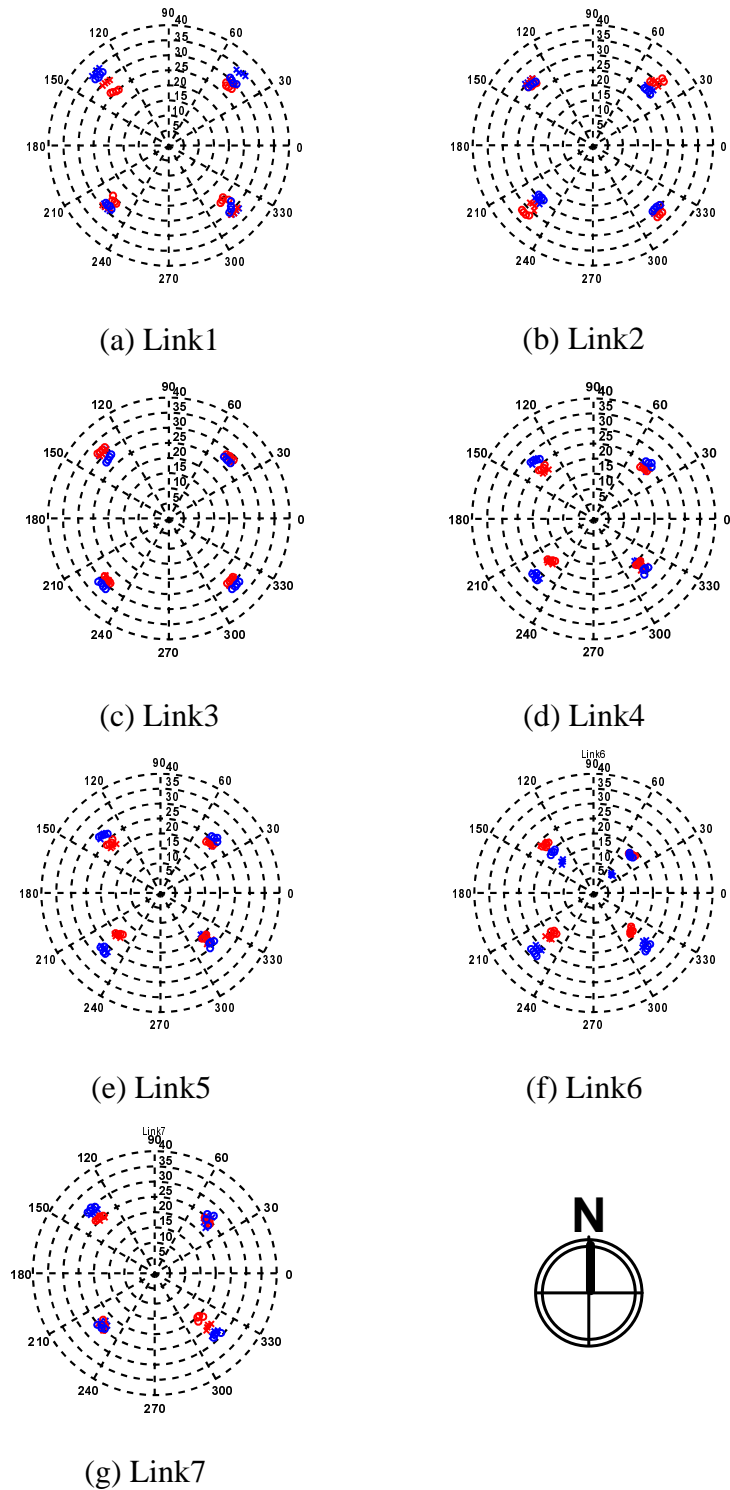


Figure 6.12: Link SINRs with client antenna turning to different directions. SINRs of uplink signals are noted by 'o' and those of downlink are noted by '+'. Blue symbols stand for SINRs acquired using the log-periodic antenna at the client and red symbols are for using the printed monopole antenna.

is more direct owing to its encountering fewer obstacles. Hence less energy is consumed due to reflection and fading.

- Variances of mean SINRs from four measurement results using two antennas pointing at each direction in every link are summarized in Table 6-C. It is clear that the printed monopole antenna sees lower SINR variations in most scenarios, which is owing to its omnidirectional radiation pattern. SINR variations acquired from using the printed monopole antenna in downlink of Link3 and uplink of Link5 are higher than those obtained from using the log-periodic antenna, which can be resulted from distinct environment change occurring during tests with the printed monopole antenna.
- Having lower gain, SINRs achieved by using the printed monopole antenna are lower than those achieved by using the log-periodic antenna in most cases according to Fig. 6.12. However, this can be compensated by systematically automatic modulation methods selection and as a result reduce bit error rate. In addition, as illustrated in Fig. 6.12 (e) and (f), when signal strengths are not strong around the entire environment where the client with log-periodic antenna is located, poor signal reception may arise due to coming signals are caught by weak gain direction of the directional antenna.
- Downlink and uplink speeds are given by an online software SPEEDTEST [119], and mean speeds with client antennas facing different directions are summarized in Table 6-D. To reduce error, the speed is tested four times when each client antenna is facing one direction. Realized speeds obtained from using the printed monopole antenna are close and sometimes even faster than those from using the log-periodic antenna.
- QMUL is covered with WiF, but when a device is at the same place where the client is located in Link7, it is easily to lose WiFi signal. However TVWS signals can still be detected according to Fig. 6.12(e), and uplink and downlink speed is

Table 6-D: Realized downlink and uplink speeds.

Links	Downlink (Mbps) (log-periodic antenna)	Uplink (Mbps) (log-periodic antenna)	Downlink (Mbps) (printed monopole)	Uplink (Mbps) (printed monopole)
Link1	6.706	1.821	7.941	2.011
Link2	7.844	2.151	9.265	2.126
Link3	10.597	2.742	10.07	3.081
Link4	6.527	3.596	7.703	3.05
Link5	4.293	1.599	3.492	1.322
Link6	3.675	1.761	4.723	1.833
Link7	7.401	3.754	9.466	3.560

1.322 Mbps and 3.492 Mbps, respectively if use the printed monopole antenna. Therefore it is verified that TVWS signals have stronger competence to bypass obstacles than WiFi signals and a wireless network built on it is more easily to be reachable at corners than a WiFi wireless network.

6.5 Summary

In this chapter, the in-house developed miniaturized narrowband antenna and the compact UWB antenna are connected to IoT devices and their system performance is evaluated under real-time communications. Based on measurement results, both the two antennas exhibit stable performance with different device orientations. And they are easily to be integrated into IoT devices thanks to the fully planar and compact properties. Moreover, the occupancy of TV channels at QMUL is measured. Finally, the competitiveness of TVWS signals is verified through measuring a testbed built on TVWS under various transmission environments.

Chapter 7

Conclusions and Future Work

7.1 Conclusions

In this thesis, three antennas, including a miniaturized narrowband antenna and two ultra-wideband (UWB) antennas, are designed with the characteristic mode analysis (CMA) for Internet-of-Things (IoT) applications over the TV white space (TVWS). Main features of these antennas are summarized in Fig. 7.1.

In Chapter 3, a miniaturized narrowband circular antenna is transformed from a vertical monopole. With relations between dimensions of the radiator and its resonant frequency being clarified via the CMA, the radiator can be generally designed at any desired frequency with a specific Rogers 5880 substrate height. Afterwards, a loop structure paralleled with the proposed radiating body is adopted to excite the significant mode through power transfer via magnetic coupling.

In Chapter 4, when designing the printed UWB monopole antenna, CMA is firstly carried out on a U-shaped plate to distinguish the modes with the UWB potential. After incorporating a substrate, a tapered microstrip feeding line, and a notched ground, the CMA on the structure is carried out again with an excitation. And it is revealed


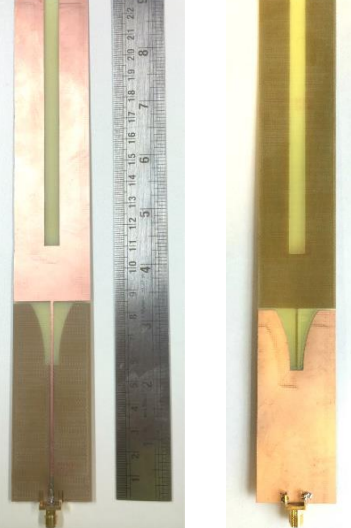

Antenna design	Main features
	<ul style="list-style-type: none"> • Circular radiating body • Ring ground plane with a cut • Magnetic feeding loop • Lateral radius: 0.052λ • Height: 0.005λ • Resonant frequency: 474 MHz • VSWR<2 bandwidth: 2.2 MHz • Omnidirectional radiation pattern • Gain: 0.02 dBi
	<ul style="list-style-type: none"> • U-shape printed monopole antenna • Tapered notch on ground • Size: $231 \times 35 \times 0.8 \text{ mm}^3$ • VSWR<2 bandwidth: 474-1212 MHz • Omnidirectional radiation pattern • Gain over the UHF TV band: 1.4-1.9 dBi • Radiation efficiency over the UHF TV band: 76.2%-92.4%
	<ul style="list-style-type: none"> • Dual Annular Ring Antenna • Slots are cut to reduce resonant frequency • The inner ring is added to create more resonating modes • Energy coupled feeding strips • Size: $200 \times 140 \times 3.2 \text{ mm}^3$ • $S_{11} < -10 \text{ dB}$ (VSWR<1.9) bandwidth: 470-987 MHz • Omnidirectional radiation pattern • Gain: 2.5-3.8 dBi

Figure 7.1: Antennas proposed in this thesis and their main features.

that multiple significant modes having wideband potential are excited to achieve the UWB behavior. The bandwidth-efficiency product of this antenna is close to that of the theoretical limit and it exceeds the products of most published designs having similar electrical sizes.

In Chapter 5, the TCM is fully utilized to create multiple modes with adjacent resonant frequencies to achieve a UWB annular ring antenna. With the CMA, this thesis firstly quantifies the relationship between dimensions of the annular ring and resonant frequencies of its basic two modes to provide a general design reference for annular ring-shaped antennas. Resonant modes on the dual annular ring are excited by energy coupled from corresponding strips operating as dipoles. Since the resonant frequency of each mode can be tuned by changing dimensions of the two rings and these modes are excited selectively, the proposed design procedure can be flexibly applied to design kinds of wideband and multi-band antennas.

Finally, in Chapter 6, the monitored UHF TV spectrum at Queen Mary University of London demonstrates the system usability of the proposed UWB printed monopole antenna over the entire TV spectrum, as well as the abundance of frequency resource for the TVWS. In addition, the miniaturized circular antenna and the UWB printed monopole antenna are integrated into IoT devices, and their omnidirectional radiation properties are verified by measuring the system performance.

7.2 Future Work

In this section, we identify the following research challenges that need to be addressed in the future work.

7.2.1 Time Domain Behavior of UWB Antennas

As introduced in Chapter 2, UWB systems employ very short pulses to deliver information, in other words, enormous bandwidth is occupied. Thence, antennas in UWB systems also act as band-pass filters. Normally, signals arrived at the receiver have distortions in shape and sometimes present a long tail termed the "ringing effect". Therefore, in the follow-up study, it is essential to study the proposed UWB antennas from a time domain perspective to avoid introducing unwanted distortions [120]. Meanwhile, when studying the time domain behavior, TVWS emission limits specified by regulators should be taken into account to avoid interference to active digital broadcasting services, which implies that an appropriate source pulse shape should be selected.

7.2.2 Variations of the UWB Annular Ring-Shaped Antenna

Although the final antenna structure in Chapter 6 is complicated, the design methodology and the functionality of each component are clear. Furthermore, the resonant frequency of each characteristic mode can be tuned by changing dimensions of the annular ring based on the close-form estimation, and the modes can be excited selectively. Therefore, this design procedure for UWB antenna using CMA could be flexibly applied to satisfy various antenna design requirements. For example, by tuning modal resonances to widely separated frequencies, multi-band antennas could be achieved. Dual-polarized antennas are realized by exciting modes having currents along the long and the short axes separately with two ports. These variations are to be realized in the future as examples to further prove the generalized antenna design methodology with CMA.

7.2.3 Radiation Pattern Synthesis and Stability

Work on this thesis mainly focuses on antenna miniaturization and bandwidth enhancement. However, since the IoT has been applied to all kinds of fields, omnidirectional

radiation patterns may not satisfy some applications having special requirements for antennas' radiation patterns. Providing far-field radiation pattern for each characteristic mode, the CMA is a useful tool for radiation pattern synthesis [71]. Future work will study how to select a number of significant modes and excite them to specific weights, and therefore obtain a designated radiation pattern. Moreover, a stable radiation pattern can be achieved across a broad frequency band by exciting characteristic modes sharing similar radiation patterns. With radiation patterns synthesized and stabilized by CMA, the follow-up work will produce more competitive antennas for IoT devices.

7.2.4 Platform-Embedded Antenna Design

CMA can obtain electromagnetic properties of an arbitrary structure, including IoT devices, without excitation. Therefore, instead of designing antennas independently, systematic antenna designs with the platform being taken into consideration are prospected in the future work. The improved design methodology can make antennas' simulated results closer to their system performance in practical measurements. In addition, this approach provides possibility to utilize devices themselves as resonators, and thence brings significant opportunities for low frequency antenna realization within compact devices.

References

- [1] Q. Zhijin, “Compressive sensing over tv white space in wideband cognitive radio,” *PhD thesis, Queen Mary University of London*, June 2016.
- [2] D. F. Sievenpiper, D. C. Dawson, M. M. Jacob, T. Kanar, S. Kim, J. Long, and R. G. Quarfoth, “Experimental validation of performance limits and design guidelines for small antennas,” *IEEE Transactions on Antennas and Propagation*, vol. 60, no. 1, pp. 8–19, 2012.
- [3] A. K. Skrivervik, J.-F. Zurcher, O. Staub, and J. Mosig, “Pcs antenna design: The challenge of miniaturization,” *IEEE Antennas and Propagation Magazine*, vol. 43, no. 4, pp. 12–27, 2001.
- [4] C. A. Balanis, “Antenna theory: analysis and design, 4th edition,” *John Wiley & Sons*, 2016.
- [5] Y.-W. Chi, K.-L. Wong, and S.-W. Su, “Broadband printed dipole antenna with a step-shaped feed gap for dtv signal reception,” *IEEE Transactions on Antennas and Propagation*, vol. 55, no. 11, pp. 3353–3356, 2007.
- [6] C. H. See, R. A. Abd-Alhameed, D. Zhou, and P. S. Excell, “A planar inverted-fl antenna (pifla) with a rectangular feeding plate for lower-band uwb applications,” *IEEE Antennas and Wireless Propagation Letters*, vol. 9, pp. 149–151, 2010.
- [7] Carlson Wireless Technologies Broadband and Voice Product, *Log Periodic Directional UHF Antenna for RuralConnect CPE*, Aug. 2014.
- [8] K. Ashton, “That internet of things thing,” *RFID journal*, vol. 22, no. 7, pp. 97–114, 2009.
- [9] Business Insider Intelligence. *BI Intelligence projects 34 billion devices will be connected by 2020*. [Online]. Available: <http://www.businessinsider.com/bi-intelligence-34-billion-connected-devices-2020-2015-11?IR=T>.
- [10] Federal Communications Commission. (2010, Sep.). *In the Matter of Unlicensed Operation in the TV Broadcast Bands, Additional Spectrum for Unlicensed Devices Below 900 MHz and in the 3 GHz Band, Second Memorandum Opinion and Order*. [Online]. Available: <http://www.adaptrum.com/docs/FCC-10-174A1.pdf>.

- [11] Federal Communications Commission. (2012, Apr.). *In the Matter of Unlicensed Operation in the TV Broadcast Bands, Additional Spectrum for Unlicensed Devices Below 900 MHz and in the 3 GHz Band, Third Memorandum Opinion and Order*. [Online]. Available: http://transition.fcc.gov/Daily_Releases/Daily_Business/2012/db0405/FCC-12-36A1.pdf.
- [12] U.K. Office of Communications. (2012, Nov.). *TV white spaces-A consultation on white space device requirements*. [Online]. Available: <http://stakeholders.ofcom.org.uk/binaries/consultations/whitespaces/summary/condoc.pdf>.
- [13] U.K. Office of Communications. (2015, Feb.). *Implementing TV White Spaces*. [Online]. Available: <http://stakeholders.ofcom.org.uk/binaries/consultations/white-space-coexistence/statement/tvws-statement.pdf>.
- [14] The European Telecommunications Standards Institute. (2014, Apr.). *White Space Devices (WSD); Wireless Access Systems operating in the 470 MHz to 790 MHz frequency band; Harmonized EN covering the essential requirements of article 3.2 of the R&TTE Directive*. [Online]. Available: http://www.etsi.org/deliver/etsi_en/301500_301599/301598/01.00.00_20/en_301598v010000a.pdf
- [15] Weightless SIG, "Weightless Specification, 1st ed"., Apr. 2013.
- [16] F. C. Commission, "First report and order in the matter of revision of part 15 of the commission's rules regarding ultra-wideband transmission systems. et-docket. 2002: 98-153," Apr. 2002.
- [17] Z. Qing, L. Wei, Y. Gao, and C. G. Parini, "Compressive spectrum sensing augmented by geo-location database," in *International Workshop on Smart Spectrum at IEEE Wireless Communications and Networking Conference (WCNC)*, New Orleans, LA, Mar. 2015, pp. 1170–1174.
- [18] N. Wang, Y. Gao, and B. Evans, "Database-augmented spectrum sensing algorithm for cognitive radio," in *IEEE International Conference on Communications (ICC)*, London, UK, Jun. 2015, pp. 7468–7473.
- [19] Z. Qing, Y. Gao, and C. G. Parini, "Data-assisted low complexity compressive spectrum sensing on real-time signals under sub-nyquist rate," *IEEE Transactions on Wireless Communications*, vol. 15, no. 2, pp. 1174–1185, Feb. 2016.

- [20] Z. Qing, Y. Gao, M. Plumbley, and C. G. Parini, "Wideband spectrum sensing on real-time signals at sub-nyquist sampling rates in single and cooperative multiple nodes," *IEEE Transactions on Signal Processing*, 2016, to be published.
- [21] R. J. Garbacz and R. H. Turpin, "A generalized expansion for radiated and scattered fields," *IEEE Transactions on Antennas and Propagation*, vol. 19, no. 3, pp. 348–358, May 1971.
- [22] R. F. Harrington and J. R. Mautz, "The theory of characteristic modes for conducting bodies," *IEEE Transactions on Antennas and Propagation*, vol. 19, no. 5, p. 622C628, May 1971.
- [23] —, "Computation of characteristic modes for conducting bodies," *IEEE Transactions on Antennas and Propagation*, vol. 19, no. 5, p. 629C639, May 1971.
- [24] Juniper Research. (2017, Mar.). *RFID to Unlock Next-Gen Retail Services*. [Online]. Available: http://www.etsi.org/deliver/etsi_en/301500_301599/301598/01.00.00_20/en_301598v010000a.pdf.
- [25] J. Stine, I. Flory, G. Karolkowski, R. Hagedorn, K. Jacobs, M. Petevinos, M. Rietra, M. Chemin, J. N. Gillot, A. Vayner, and D. Krupitzer, "Iot for the consumer goods and retail businesses: What are the benefits and where should one start?" *The Consumer Goods Forum, Capgemini and Inter*, 2017.
- [26] MooCall. (2016, Sep.). *Connecting You to Your Animals*. [Online]. Available: <http://www.vodafone.com/business/iot/case-study/moocall>.
- [27] CropX. (2016, Dec.). *Top Sensor Manufacturers Make Strategic Investment in CropX*. [Online]. Available: <https://cropx.com/press-releases/top-sensor-manufacturers-make-strategic-investment-cropx/>.
- [28] IBM. (2017, Jun.). *IBM integrates with BMW CarData to Enable New and Innovative Services for Drivers*. [Online]. Available: <https://www-03.ibm.com/press/us/en/pressrelease/52595.wss>.
- [29] D. Boswarthick, O. Elloumi, and O. Hersent, "M2m communications: a systems approach," *John Wiley & Sons*, March 2012.
- [30] —, *M2M communications: a systems approach*. John Wiley & Sons, 2012.
- [31] Weightless. (2016, Feb.). *The Argument for LPWAN in the Inter-*

- net of Things*. [Online]. Available: <http://www.weightless.org/about/the-argument-for-lpwan-in-the-internet-of-things>.
- [32] S. Srikanteswara and D. Choudhury, "A review of tv whitespace portable devices," in *Radio and Wireless Symposium (RWS), 2010 IEEE*. IEEE, 2010, pp. 480–483.
- [33] D. T. Otermat, C. E. Otero, and I. Kostanic, "Analysis of the fm radio spectrum for internet of things opportunistic access via cognitive radio," in *Internet of Things (WF-IoT), 2015 IEEE 2nd World Forum on*. IEEE, 2015, pp. 166–171.
- [34] P. Rawat, K. D. Singh, and J. M. Bonnin, "Cognitive radio for m2m and internet of things: A survey," *Computer Communications*, vol. 94, pp. 1–29, 2016.
- [35] ITU, "Digital dividend insights for spectrum decisions," August 2013.
- [36] A. D. Yaghjian and S. R. Best, "Impedance, bandwidth, and q of antennas," *IEEE Transactions on Antennas and Propagation*, vol. 53, no. 4, pp. 1298–1324, 2005.
- [37] L. J. Chu, "Physical limitations of omni-directional antennas," *Journal of applied physics*, vol. 19, no. 12, pp. 1163–1175, 1948.
- [38] R. C. Hansen, "Fundamental limitations in antennas," *Proceedings of the IEEE*, vol. 69, no. 2, pp. 170–182, 1981.
- [39] J. S. McLean, "A re-examination of the fundamental limits on the radiation q of electrically small antennas," *IEEE Transactions on antennas and propagation*, vol. 44, no. 5, p. 672, 1996.
- [40] R. Collin and S. Rothschild, "Evaluation of antenna q," *IEEE Transactions on Antennas and Propagation*, vol. 12, no. 1, pp. 23–27, 1964.
- [41] H. A. Wheeler, "Fundamental limitations of small antennas," *Proceedings of the IRE*, vol. 35, no. 12, pp. 1479–1484, 1947.
- [42] P.-L. Chi, K. M. Leong, R. Waterhouse, and T. Itoh, "A miniaturized cpw-fed capacitor-loaded slot-loop antenna," in *Signals, Systems and Electronics, 2007. ISSSE'07. International Symposium on*. IEEE, 2007, pp. 595–598.
- [43] G. Breed, "Basic principles of electrically small antennas," *High Frequency Electronics*, vol. 6, no. 2, pp. 50–53, 2007.
- [44] Y. Hwang, Y. Zhang, G. Zheng, and T. K. Lo, "Planar inverted f antenna loaded with high permittivity material," *Electronics Letters*, vol. 31, no. 20, pp. 1710–

- 1712, 1995.
- [45] J. S. Colburn and Y. Rahmat-Samii, "Patch antennas on externally perforated high dielectric constant substrates," *IEEE Transactions on Antennas and Propagation*, vol. 47, no. 12, pp. 1785–1794, 1999.
- [46] A. Kiourti and K. S. Nikita, "Miniature scalp-implantable antennas for telemetry in the mics and ism bands: design, safety considerations and link budget analysis," *IEEE Transactions on Antennas and Propagation*, vol. 60, no. 8, pp. 3568–3575, 2012.
- [47] J. Lluís, M.-v. Marta, and S. C. Raquel, "Handbook on small antennas," *ESoA Course on Compact Antennas*, 2011.
- [48] P. M. Ikonen, K. N. Rozanov, A. V. Osipov, P. Alitalo, and S. A. Tretyakov, "Magnetodielectric substrates in antenna miniaturization: Potential and limitations," *IEEE Transactions on Antennas and Propagation*, vol. 54, no. 11, pp. 3391–3399, 2006.
- [49] R. Hansen and M. Burke, "Antennas with magneto-dielectrics," *Microwave and optical technology letters*, vol. 26, no. 2, pp. 75–78, 2000.
- [50] J. K. Ji, W. K. Ahn, J. S. Kum, S. H. Park, G. H. Kim, and W. M. Seong, "Miniaturized t-dmb antenna with a low-loss ni-mn-co ferrite for mobile handset applications," *IEEE Magnetics Letters*, vol. 1, pp. 5 000 104–5 000 104, 2010.
- [51] J. Oh and K. Sarabandi, "Low profile, miniaturized, inductively coupled capacitively loaded monopole antenna," *IEEE Transactions on Antennas and Propagation*, vol. 60, no. 3, pp. 1206–1213, 2012.
- [52] H. Wang, Z. Zhang, Y. Li, and Z. Feng, "A dual-resonant shorted patch antenna for wearable application in 430 mhz band," *IEEE Transactions on Antennas and Propagation*, vol. 61, no. 12, pp. 6195–6200, 2013.
- [53] S. K. Podilchak, M. Caillet, D. Lee, Y. M. Antar, L. C. Chu, J. Cain, M. Hammar, D. Caldwell, and E. Barron, "A compact circularly polarized antenna using an array of folded-shortened patches," *IEEE Transactions on Antennas and Propagation*, vol. 61, no. 9, pp. 4861–4867, 2013.
- [54] J. Rashed and C.-T. Tai, "A new class of resonant antennas," *IEEE Transactions*

- on Antennas and Propagation*, vol. 39, no. 9, pp. 1428–1430, 1991.
- [55] D. K. Chew and S. R. Saunders, “Meander line technique for size reduction of quadrifilar helix antenna,” *IEEE Antennas and wireless propagation letters*, vol. 1, no. 1, pp. 109–111, 2002.
- [56] J. P. Gianvittorio and Y. Rahmat-Samii, “Fractal antennas: A novel antenna miniaturization technique, and applications,” *IEEE Antennas and Propagation magazine*, vol. 44, no. 1, pp. 20–36, 2002.
- [57] Y.-L. Ban, Y.-F. Qiang, Z. Chen, K. Kang, and J.-H. Guo, “A dual-loop antenna design for hepta-band wwan/lte metal-rimmed smartphone applications,” *IEEE Transactions on Antennas and Propagation*, vol. 63, no. 1, pp. 48–58, 2015.
- [58] S. Ahn, S. Park, Y. Noh, D. Park, and H. Choo, “Design of an on-glass vehicle antenna using a multiloop structure,” *Microwave and Optical Technology Letters*, vol. 52, no. 1, pp. 107–110, 2010.
- [59] J. H. Schaffner, H. J. Song, A. Bekaryan, H.-P. Hsu, M. Wisnewski, and J. Graham, “The impact of vehicle structural components on radiation patterns of a window glass embedded fm antenna,” *IEEE Transactions on Antennas and Propagation*, vol. 59, no. 10, pp. 3536–3543, 2011.
- [60] M. Z. Win, D. Dardari, A. F. Molisch, W. Wiesbeck, and J. Zhang, “History and applications of uwb,” *Proc. IEEE*, vol. 97, no. 2, pp. 198–204, 2009.
- [61] G. F. Ross, “The transient analysis of multiple beam feed networks for array systems,” *Ph.D dissertation, Polytechnic Institute of Brooklyn*, 1963.
- [62] M. Z. Win and R. A. Scholtz, “Impulse radio: How it works,” *IEEE Commun. Lett.*, vol. 2, pp. 36–38, 1998.
- [63] ———, “Ultra-wide bandwidth time-hopping spread-spectrum impulse radio for wireless multiple-access communications,” *IEEE Trans. Commun.*, vol. 48, pp. 679–691, 2000.
- [64] J. Reed, *Introduction to ultra wideband communication systems*. Prentice Hall Press, 2005.
- [65] T. Kaiser, A. F. Molisch, and I. Oppermann, “Uwb communications systems: A comprehensive overview,” *Hindawi Publishing Corporation*, 2006.

- [66] H. Nikookar and R. Prasad, "Introduction to ultra wideband for wireless communications," *Springer Science & Business Media*, 2008.
- [67] R. Kraemer and M. Katz, "Short-range wireless communications-emerging technologies and applications," *John Wiley & Sons, Ltd*, 2009.
- [68] W. Wiesbeck, G. Adamiuk, and C. Sturm, "Basic properties and design principles of uwb antennas," *Proceedings of the IEEE*, vol. 97, no. 2, pp. 372–385, 2009.
- [69] M. Cabedo Fabres, "Systematic design of antennas using the theory of characteristic modes," Ph.D. dissertation, 2007.
- [70] H. Li, Z. T. Miers, and B. K. Lau, "Design of orthogonal mimo handset antennas based on characteristic mode manipulation at frequency bands below 1 ghz," *IEEE Transactions on Antennas and Propagation*, vol. 62, no. 5, pp. 2756–2766, 2014.
- [71] Y. Chen and C.-F. Wang, "Hf band shipboard antenna design using characteristic modes," *IEEE Transactions on Antennas and Propagation*, vol. 63, no. 3, pp. 1004–1013, 2015.
- [72] D. Ludick, E. Lezar, and U. Jakobus, "Characteristic mode analysis of arbitrary electromagnetic structures using feko," in *Electromagnetics in Advanced Applications (ICEAA), 2012 International Conference on*. IEEE, 2012, pp. 208–211.
- [73] M. Vogel, G. Gampala, D. Ludick, U. Jakobus, and C. Reddy, "Characteristic mode analysis: Putting physics back into simulation," *IEEE Antennas and Propagation Magazine*, vol. 57, no. 2, pp. 307–317, 2015.
- [74] E. Antonino-Daviu, M. Cabedo-Fabres, M. Gallo, M. Ferrando-Bataller, and M. Bozzetti, "Design of a multimode mimo antenna using characteristic modes," in *Antennas and Propagation, 2009. EuCAP 2009. 3rd European Conference on*. IEEE, 2009, pp. 1840–1844.
- [75] A. Araghi and G. Dadashzadeh, "Oriented design of an antenna for mimo applications using theory of characteristic modes," *IEEE Antennas and Wireless Propagation Letters*, vol. 11, pp. 1040–1043, 2012.
- [76] D. Manteuffel and R. Martens, "Compact multimode multielement antenna for indoor uwb massive mimo," *IEEE Transactions on Antennas and Propagation*, vol. 64, no. 7, pp. 2689–2697, 2016.

- [77] E. Antonino-Daviu, M. Cabedo-Fabres, M. Ferrando-Bataller, and A. Valero-Nogueira, "Wideband double-fed planar monopole antennas," *Electronics Letters*, vol. 39, no. 23, p. 1635, 2003.
- [78] N. L. Bohannon and J. T. Bernhard, "Design guidelines using characteristic mode theory for improving the bandwidth of pifas," *IEEE Transactions on Antennas and Propagation*, vol. 63, no. 2, pp. 459–465, 2015.
- [79] J. J. Adams and J. T. Bernhard, "A modal approach to tuning and bandwidth enhancement of an electrically small antenna," *IEEE Transactions on Antennas and Propagation*, vol. 59, no. 4, pp. 1085–1092, 2011.
- [80] W. Wu and Y. Zhang, "Analysis of ultra-wideband printed planar quasi-monopole antennas using the theory of characteristic modes," *IEEE Antennas and Propagation Magazine*, vol. 52, no. 6, pp. 67–77, 2010.
- [81] E. Antonino-Daviu, M. Fabres, M. Ferrando-Bataller, and V. M. R. Peñarrocha, "Modal analysis and design of band-notched uwb planar monopole antennas," *IEEE Transactions on Antennas and Propagation*, vol. 58, no. 5, pp. 1457–1467, 2010.
- [82] W. Hong and K. Sarabandi, "Low-profile, multi-element, miniaturized monopole antenna," *IEEE Transactions on Antennas and Propagation*, vol. 57, no. 1, pp. 72–80, 2009.
- [83] J. Oh and K. Sarabandi, "Low profile, miniaturized, inductively coupled capacitively loaded monopole antenna," *IEEE Transactions on Antennas and Propagation*, vol. 60, no. 3, pp. 1206–1213, 2012.
- [84] G. Monti, L. Catarinucci, and L. Tarricone, "Compact microstrip antenna for rfid applications," *Progress In Electromagnetics Research*, vol. 8, pp. 191–199, 2009.
- [85] R. Ma, Y. Gao, Y. Wang, and C. Parini, "Circular co-planar inverted-f antenna for uhf machine-to-machine communications," in *Antennas and Propagation & USNC/URSI National Radio Science Meeting, 2015 IEEE International Symposium on*. IEEE, 2015, pp. 1418–1419.
- [86] Y. Chen and C.-F. Wang, "Electrically small uav antenna design using characteristic modes," *IEEE Transactions on Antennas and Propagation*, vol. 62, no. 2,

- pp. 535–545, 2014.
- [87] Federal Communications Commission. (2016, Aug.) *Digital Television, Major Initiatives of Federal Communications Commission*. [Online]. Available: <http://www.fcc.gov/dtv/>
- [88] R. Caso, A. D’Alessandro, A. A. Serra, P. Nepa, and G. Manara, “A compact dual-band pifa for dvb-t and wlan applications,” *IEEE Transactions on Antennas and Propagation*, vol. 60, no. 4, pp. 2084–2087, 2012.
- [89] M. Hanqing and Q.-X. Chu, “Compact broadband planar antenna for dvb-h applications,” *Microwave and Optical Technology Letters*, vol. 51, no. 1, pp. 239–242, 2009.
- [90] H.-D. Chen, “Compact broadband microstrip-line-fed sleeve monopole antenna for dtv application and ground plane effect,” *IEEE Antennas and Wireless Propagation Letters*, vol. 7, pp. 497–500, 2008.
- [91] M. Karoui, H. Ghariani, M. Samet, M. Ramadi, and R. Pedriau, “Bandwidth enhancement of the square rectangular patch antenna for biotelemetry applications,” *International journal of information systems and telecommunication engineering*, vol. 1, no. 1, pp. 12–18, 2010.
- [92] D. T. Nguyen, D. H. Lee, and H. C. Park, “Very compact printed triple band-notched uwb antenna with quarter-wavelength slots,” *IEEE Antennas and wireless propagation letters*, vol. 11, pp. 411–414, 2012.
- [93] J. Jung, W. Choi, J. Choi *et al.*, “A small wideband microstrip-fed monopole antenna,” *IEEE Microwave and Wireless Components Letters*, vol. 15, no. 10, pp. 703–705, 2005.
- [94] C.-Y. Huang, B.-M. Jeng, and J.-S. Kuo, “Grating monopole antenna for dvb-t applications,” *IEEE Transactions on Antennas and Propagation*, vol. 56, no. 6, pp. 1775–1776, 2008.
- [95] B.-M. Jeng, C.-M. Lee, and C.-H. Luo, “Multiple-ring monopole antenna with sleeve-shaped ground for dvb-t applications,” *Progress In Electromagnetics Research*, vol. 14, pp. 155–161, 2010.
- [96] C. A. Balanis, *Antenna theory: analysis and design*. John Wiley & Sons, 2016.

-
- [97] *IEEE Standard Test Procedures for Antennas*, IEEE Std 149TM-1979 (R2008), Dec. 2008.
- [98] E. Newman, P. Bohley, and C. Walter, "Two methods for the measurement of antenna efficiency," *IEEE Transactions on antennas and propagation*, vol. 23, no. 4, pp. 457–461, 1975.
- [99] D. M. Pozar and B. Kaufman, "Comparison of three methods for the measurement of printed antenna efficiency," *IEEE Transactions on Antennas and Propagation*, vol. 36, no. 1, pp. 136–139, 1988.
- [100] C. L. Holloway, H. A. Shah, R. J. Pirkl, W. F. Young, D. A. Hill, and J. Ladbury, "Reverberation chamber techniques for determining the radiation and total efficiency of antennas," *IEEE Transactions on Antennas and Propagation*, vol. 60, no. 4, pp. 1758–1770, 2012.
- [101] X. Qian and H. Yi, *Anechoic and Reverberation Chambers: Theory, Design and Measurements*. Wiley-IEEE Press, 2018.
- [102] C. L. Holloway, H. A. Shah, R. J. Pirkl, W. F. Young, D. A. Hill, and J. Ladbury, "Reverberation chamber techniques for determining the radiation and total efficiency of antennas," *IEEE Transactions on Antennas and Propagation*, vol. 60, no. 4, pp. 1758–1770, 2012.
- [103] Q. Xu, Y. Huang, X. Zhu, L. Xing, Z. Tian, and C. Song, "A modified two-antenna method to measure the radiation efficiency of antennas in a reverberation chamber," *IEEE Antennas and Wireless Propagation Letters*, pp. 336–339, Jun. 2015.
- [104] C. L. Holloway, D. A. Hill, J. M. Ladbury, P. F. Wilson, G. Koepke, and J. Coder, "On the use of reverberation chambers to simulate a rician radio environment for the testing of wireless devices," *IEEE Transactions on Antennas and Propagation*, vol. 54, no. 11, pp. 3167–3177, 2006.
- [105] T.-Y. Shih and N. Behdad, "Design of vehicle-mounted, compact vhf antennas using characteristic mode theory," in *Antennas and Propagation (EUCAP), 2017 11th European Conference on*. IEEE, 2017, pp. 1765–1768.
- [106] R. Martens, E. Safin, and D. Manteuffel, "Inductive and capacitive excitation of the

- characteristic modes of small terminals,” in *Antennas and Propagation Conference (LAPC), 2011 Loughborough*. IEEE, 2011, pp. 1–4.
- [107] M. C. Fabr s, “Systematic design of antennas using the theory of characteristic modes,” Ph.D. dissertation, 2008.
- [108] Q. Zhang, X. Zhang, O. Holland, M. Dohler, J. M. Chareau, Y. Gao, and P. Chawdhry, “Tv white space network provisioning with directional and omni-directional terminal antennas,” in *2016 IEEE 84th Vehicular Technology Conference (VTC-Fall)*, pp. 1–5.
- [109] K. L. Wong and M. T. Chen, “Small-size lte/wwan printed loop antenna with an inductively coupled branch strip for bandwidth enhancement in the tablet computer,” *IEEE Transactions on Antennas and Propagation*, vol. 61, no. 12, pp. 6144–6151, 2013.
- [110] B.-Y. Wu, X.-Q. Sheng, R. Fabregas, and Y. Hao, “Full-wave modeling of broadband near field scanning microwave microscopy,” *Scientific reports*, vol. 7, no. 1, p. 16064, 2017.
- [111] D. Alonso, Q. Zhang, Y. Gao, and D. Valderas, “Uhf passive rfid-based sensorless system to detect humidity for irrigation monitoring,” *Microwave and Optical Technology Letters*, vol. 59, no. 7, pp. 1709–1715, 2017.
- [112] L. Bedogni, A. Trotta, M. Di Felice, Y. Gao, X. Zhang, Q. Zhang, F. Malabocchia, and L. Bononi, “Dynamic adaptive video streaming on heterogeneous tvws and wi-fi networks,” *IEEE/ACM Transactions on Networking*, vol. 25, no. 6, pp. 3253–3266, 2017.
- [113] Y. Gao, Z. Qin, Z. Feng, Q. Zhang, O. Holland, and M. Dohler, “Scalable and reliable iot enabled by dynamic spectrum management for m2m in lte-a,” *IEEE Internet of Things Journal*, vol. 3, no. 6, pp. 1135–1145, 2016.
- [114] A. Kliks, P. Kryszkiewicz, A. Umbert, J. P rez-Romero, and F. Casadevall, “Tvws indoor measurements for hetnets,” in *Wireless Communications and Networking Conference Workshops (WCNCW), 2014 IEEE*. IEEE, 2014, pp. 76–81.
- [115] M. H. Islam, C. L. Koh, S. W. Oh, X. Qing, Y. Y. Lai, C. Wang, Y.-C. Liang, B. E. Toh, F. Chin, G. L. Tan *et al.*, “Spectrum survey in singapore: Occupancy measu-

- rements and analyses,” in *Cognitive Radio Oriented Wireless Networks and Communications, 2008. CrownCom 2008. 3rd International Conference on*. IEEE, 2008, pp. 1–7.
- [116] M. López-Benítez, A. Umbert, and F. Casadevall, “Evaluation of spectrum occupancy in spain for cognitive radio applications,” in *Vehicular technology conference, 2009. VTC Spring 2009. IEEE 69th*. IEEE, 2009, pp. 1–5.
- [117] CRFS, *RFeye Nodes*. [Online]. Available: [Avaliable:https://us.crf.com/en/hardware/nodes/](https://us.crf.com/en/hardware/nodes/).
- [118] Carlson wireless ruralconnect. [Online]. Available: <http://www.carlsonwireless.com/ruralconnect/>
- [119] Speedtest. [Online]. Available: <http://www.speedtest.net/>.
- [120] L. Guo, “Study and miniaturisation of antennas for ultra wideband communication systems,” Ph.D. dissertation, 2009.